Forcings and chaos in interannual to decadal climate change

J. Hansen,[1] M. Sato,[1] R. Ruedy,[1] A. Lacis,[1] K. Asamoah,[2] K. Beckford,[3] S. Borenstein,[3] E. Brown,[4] B. Cairns,[5] B. Carlson,[1] B. Curran,[6] S. de Castro,[3] L. Druyan,[17] P. Etwarrow,[8] T. Ferede,[6] M. Fox,[6] D. Gaffen,[9] J. Glascoe,[1] H. Gordon,[10] S. Hollandsworth,[11] X. Jiang,[15] C. Johnson,[8] N. Lawrence,[8] J. Lean,[12] J. Lerner,[1] K. Lo,[1] J. Logan,[13] A. Luckett,[6] M.P. McCormick,[14] R. McPeters,[11] R. Miller,[15] P. Minnis,[15] I. Ramberran,[2] G. Russell,[1] P. Russell,[16] P. Stone,[17] I. Tegen,[15] S. Thomas,[8] L. Thomason,[15] A. Thompson,[11] J. Wilder,[18] R. Willson,[7] and J. Zawodny [15]

Abstract. We investigate the roles of climate forcings and chaos (unforced variability) in climate change via ensembles of climate simulations in which we add forcings one by one. The experiments suggest that most interannual climate variability in the period 1979-1996 at middle and high latitudes is chaotic. But observed SST anomalies, which themselves are partly forced and partly chaotic, account for much of the climate variability at low latitudes and a small portion of the variability at high latitudes. Both a natural radiative forcing (volcanic aerosols) and an anthropogenic forcing (ozone depletion) leave clear signatures in the simulated climate change that are identified in observations. Pinatubo aerosols warm the stratosphere and cool the surface globally, causing a tendency for regional surface cooling. Ozone depletion cools the lower stratosphere, troposphere and surface, steepening the temperature lapse rate in the troposphere. Solar irradiance effects are small, but our model is inadequate to fully explore this forcing. Well-mixed anthropogenic greenhouse gases cause a large surface warming that, over the 17 years, approximately offsets cooling by the other three mechanisms. Thus the net calculated effect of all measured radiative forcings is approximately zero surface temperature trend and zero heat storage in the ocean for the period 1979-1996. Finally, in addition to the four measured radiative forcings, we add an initial (1979) disequilibrium forcing of +0.65 W/m². This forcing yields a global surface warming of about 0.2°C over 1979-1996, close to observations, and measurable heat storage in the ocean. We argue that the results represent evidence of a planetary radiative imbalance of at least 0.5 W/m²; this disequilibrium presumably represents unrealized warming due to changes of atmospheric composition prior to 1979. One implication of the disequilibrium forcing is an expectation of new record global temperatures in the next few years. The best opportunity for observational confirmation of the disequilibrium is measurement of ocean temperatures adequate to define heat storage.

[1]NASA Goddard Institute for Space Studies, New York.
[2]MAST High School, Cambria Heights, Queens, New York.
[3]Department of Natural Science, York College, Jamaica, New York.
[4]Marine Sciences, University of Miami, Coral Gables, Florida.
[5]Department of Applied Physics, Columbia University, New York.
[6]Bronx High School of Science, Bronx, New York.
[7]Center for Climate Systems Research, Columbia University, New York.
[8]Far Rockaway High School, Brooklyn, New York.
[9]NOAA Air Resources Laboratory, Silver Spring, Maryland.
[10]Department of Physics, University of Miami, Coral Gables, Florida.
[11]NASA Goddard Space Flight Center, Greenbelt, Maryland.
[12]E.O. Hulbert Center for Space Research, Naval Research Laboratory, Washington, D. C.
[13]Department of Earth and Planetary Sciences, Harvard University, Cambridge, Massachusetts.
[14]Department of Physics, Hampton University, Hampton, Virginia.
[15]NASA Langley Research Center, Hampton, Virginia.
[16]NASA Ames Research Center, Moffett Field, California.
[17]Center for Meteorology, Massachusetts Institute of Technology, Cambridge, Massachusetts.
[18]Engineering Division, Polytechnic University, Brooklyn, New York.

1. Introduction

Scientists and laypersons have a predilection for deterministic explanations of climate variations. However, climate can vary chaotically, i.e., in the absence of any forcing. Indeed, the climate system exemplifies "complexity," a combination of deterministic behavior and unpredictable variations ("noise" or "chaos"). Interactions connect all parts of the system, giving rise to complex dynamical patterns that never precisely repeat. The slightest alteration of initial or boundary conditions changes the developing patterns, and thus next year's weather is inherently unpredictable. This behavior results from the nonlinear fundamental equations governing the dynamics of such a system [*Lorenz*, 1963]. Yet the same laws limit the behavior and can be used to determine a probability function for the response to any imposed climate forcing.

Climate change of recent decades offers a superb opportunity to compare the roles of climate forcings and chaos. Global observations provide definition of several climate forcings as well as measurements of the climate response. Global climate models can generate a reasonable facsimile of the climate system, and even modest computer resources are now sufficient to make ensembles of climate simulations on decadal timescales.

Such studies have practical relevance. Public attention has been focused on climate change by recent large regional climate anomalies and by the realization that humankind itself has the potential to alter global climate. Prudent public policy requires improved knowledge of the roles of natural and anthropogenic factors in climate change.

Our objective is to study forced and unforced climate variability on interannual to decadal timescales. We first outline our strategy of investigation and then document the climate model and climate forcings. Results are organized as follows: (1) global mean climate response for all models and forcings, (2) regional interannual climate variability and predictability implied by the simulations, (3) a detailed look at the response to forcings as a function of geography, season and height.

2. Strategy of Investigation

Our strategy is influenced by the belief that scientists should try to communicate incomplete understanding of climate change to the public even as they try to improve it. This implies a need to pay attention to space and timescales most noticeable to the layperson. A second consideration is that climate models, especially the ocean component, provide only a crude representation of reality, so we seek a perspective on model capabilities that helps focus future model development. A third factor is the need to compare multiple climate forcing mechanisms on a uniform basis.

2.1. Freeze Atmospheric Model

Our simulations all employ the identical atmospheric model SI95, fixed during the 1995 Goddard Institute for Space Studies (GISS) Summer Institute on Climate and Planets. A frozen model allows precise comparison of simulations with different forcings and different ways of treating the ocean. It also helps characterize model merits and deficiencies, aiding interpretation of experiments and development of an improved model.

2.2. Employ Range of Ocean Treatments

The ocean's role in climate change is uncertain and current ocean models are primitive, so we use several distinct oceans to investigate the role of the ocean in interannual to decadal climate change. First, we specify observed time-varying SSTs, thus providing a "perfect" but noninteractive ocean boundary condition for driving the atmosphere. Second, we calculate ocean temperature with a simple "Q flux" ocean [*Hansen et al.*, 1984], which has specified horizontal transport of heat and diffusive mixing of heat perturbations into the deep ocean. Finally, we use ocean models with interactive dynamics, employing two separate models: the classical ocean model developed at the Geophysical Fluid Dynamics Laboratory (GFDL) [*Bryan*, 1969; *Cox*, 1984] as implemented at GISS [*Miller and Jiang*, 1996], and a model developed independently at GISS [*Russell et al.*, 1995].

2.3. Add Forcings One by One

We add radiative climate forcings to the model one at a time, so their individual influences can be studied. The first (control) runs have no time varying radiative forcings. We then successively add stratospheric aerosols, well-mixed greenhouse gases, ozone, and solar irradiance changes, all of which have been measured since 1979, and finally a constant 0.65 W/m^2 forcing representing a plausible initial (1979) planetary radiative disequilibrium. We do not explicitly include other suspected climate forcings, such as

tropospheric aerosols and land use changes, because accurate data are not presently available, but all pre-1979 forcings implicitly affect the initial radiative disequilibrium.

Table 1 indicates the array of experiments pertaining to the choices of ocean model and radiative forcing. We designate members of this array as runs Mmn, where M is A, B, C, or D for the four specifications of the ocean: m is a, b, c, d, e, or f for the six choices of forcing, and n is an integer specifying the member of the ensemble, as discussed below.

2.4. Make Ensembles of Runs

We generate ensembles of five or ten runs for most model/forcing combinations (Table 1) by slightly altering initial atmospheric temperatures. The ensembles provide a measure of the unforced variability in the climate simulations, allowing us to investigate inherent limitations on predictability due to the chaotic nature of the climate system. The ensembles also yield a measure of the numerical significance of computed climate changes for the specific models employed.

2.5. Study Climate Change and Seasonal Predictability

We study together global climate change and seasonal prediction of regional climate. These different time and space scales are affected by the same processes, albeit to varying degrees. Chaotic fluctuations that may dominate regional interannual climate change also influence the ability to detect decadal global change; and global radiative forcings have an influence on regional climate variations which we want to quantify, even if it is small on a 17-year timescale.

Quantitative comparison of the roles of global climate forcings and unforced variability on different time and space scales should be useful for communication with the layperson as well as between meteorological subdisciplines. For example, it may help answer persistent questions about whether regional climate fluctuations are related to global climate change.

2.6. Involve Students and Educators in Model Analysis

We involve students and educators from local high schools, colleges, and universities in our model testing, experiments, and analyses. Students and educators work full time at GISS in the summer, attend research team meetings during the academic year, and have electronic access to our data from their schools. The educators are incorporating elements of the research program into their science curricula.

Our aim is to improve our research product as well as teaching of science in the classroom. A long-range goal is to contribute to public understanding of climate variability and the nature of science research.

2.7. Repeat Experiments With Improved Model and Data

As models will always be imperfect, an important test of conclusions is their consistency as model realism increases. We plan to repeat key experiments with future models, which we intend to freeze at intervals of 1-2 years. The accuracy of climate forcing data also should improve with time, and data may become available for forcings not included in our present simulations. It will be important to document changes in the results caused by new forcing data, as opposed to changes caused by model improvements.

2.8. Extend Period of Simulation

We chose 1979-1996 for our initial climate simulations because several climate forcings were measured accurately in that period.

Table 1. Run Identification, Number of Runs, and Years Covered by Simulations in our Array of Experiments With a Fixed Atmospheric Model

Radiative Forcing	Ocean Representation			
	A (Observed SST)	B (Q Flux Model)	C (GISS Model)	D (GFDL Model)
a No radiative forcing	run Aa 5 runs (1979-1996)	run Ba 100-year run 5 21-year runs	run Ca 100-year run 5 21-year runs	run Da 100-year run 5 21-year runs
a' $a + 0.65$ W/m^2	X	run Ba' 5 21-year runs	run Ca' 5 21-year runs	run Da' 5 21-year runs
b Stratospheric aerosols	run Ab 10 runs (1979-1996)	run Bb 5 runs (1979-1996)	X	X
c $b +$ ozone change	run Ac 5 runs (1979-1996)	run Bc 5 runs (1979-1996)	X	X
d $c +$ greenhouse gas change	run Ad 5 runs (1979-1996)	run Bd 5 runs (1979-1996)	X	X
e $d +$ Solar change	run Ae 10 runs (1979-1996)	run Be 5 runs (1979-1996)	run Ce 5 runs (1979-1996)	run De 5 runs (1979-1996)
f $e + 0.65$ W/m^2	X	run Bf 5 runs (1979-2000)	run Cf 5 runs (1979-2000)	run Df 5 runs (1979-2000)

The upper case letter in the run identification specifies the ocean model and the lower case letter specifies the radiative forcing.

Also certain climate diagnostics, such as MSU (Microwave Sounding Unit) temperatures, are available for that period. The brevity of this period allows a large number of simulations with our limited (workstation) computing resources.

However, the length of our present simulations is too short to draw many inferences about decadal climate change. We do not extend the present runs, because we have identified improvements that should be included in the next model. However, our future experiments will include longer periods.

3. Atmospheric Model

The SI95 model uses the same "B grid" distribution of variables and vertical layering as GISS model II [*Hansen et al.*, 1983a] but with finer horizontal resolution, higher precision numerical integrations, and improved representations of key physical processes. Major changes are documented in the literature, and additional minor changes are specified here. The present model has recognized shortcomings, key weak points being summarized below. Our aim is to spur and shape model development as well as define caveats needed for interpretation of climate experiments.

The equilibrium global climate sensitivity of the SI95 model is about 3.5°C for doubled CO_2 using the Q flux ocean (Appendix A). Extensive diagnostics of the equilibrium response to doubled CO_2

are available on the internet via the GISS home page (www.giss.nasa.gov).

The following summary of changes between the model II and the SI95 model employs technical jargon for the sake of brevity. Readers uninterested in model detail can skip to section 3.11.

3.1. Moist Convection and Prognostic Cloud Calculations

The moist convection parameterization [*Del Genio and Yao*, 1993] specifies a vertical mass flux proportional to the moist static instability, using two plumes one of which is entraining, incorporating a downdraft flux equal to one-third that of the updraft, including vertical mixing of horizontal momentum, and representing effects of mesoscale cirrus anvils. Cumulus mass fluxes are constrained so as to relax the atmosphere to a neutrally stable state at the cloud base. The convective scale downdrafts are intended to prevent excessive drying of the boundary layer by compensating subsidence. An objective of the cirrus anvil parameterization is to realistically include anvil moistening of the upper troposphere and anvil radiative effects.

The chief objective of prognostic clouds is to permit analysis of climate feedbacks. Evidence that the new prognostic cloud calculation [*Del Genio et al.*, 1996] has the correct sense for at least one component of the large-scale cloud feedback on global temperature is provided by the fact that the variation of cloud optical

depth with temperature in the model is in good agreement with International Satellite Cloud Climatology Project (ISCCP) observations for low clouds [Del Genio et al., 1996]. Another point in favor of the new prognostic clouds is that they provide a more realistic albedo than model II in some regions, apparently because of unrealistic cirrus cloud optical depths in model II. However, the realism of prognostic clouds is subject to the realism of other model characteristics, such as the distribution of atmospheric water vapor. We discuss in section 3.11 evidence for unrealistic aspects of the planetary radiation balance in the SI95 model, which are probably associated with cloud optical properties and which in turn may be a consequence of other model deficiencies.

The prognostic cloud water parameterization [Del Genio et al., 1996] yields an effective cloud particle radius, which is used along with the cloud water content to infer cloud optical depth. Radiation calculations assume 10 μm effective particle size in defining the scattering "phase function" and single scatter albedo, but the principal effect of particle size is included implicitly via its impact on cloud optical depth. Clouds are approximated as plane parallel for radiation calculations.

Cloud calculations are carried out once per hour. Full radiation calculations are carried out every fifth hour, using the clouds calculated that hour. Radiative fluxes change each hour in accord with the incident solar flux, as in model II. On climatological timescales, say seasonal means, the inconsistency between the cloud and the radiation time steps should have only small effects; this was confirmed via simulations with a 1-hour radiation time step with model II [Hansen et al., 1983a] and reconfirmed with our present model.

3.2. Planetary Boundary Layer

The planetary boundary layer (PBL) treatment in the SI95 climate model is the method described by Hartke and Rind [1997], which parameterizes drag and mixing coefficients based on similarity theory. Separate transfer coefficients are determined for heat, momentum and moisture. The surface layer model, defined to be a constant flux layer, computes surface fluxes using a wind profile model to extrapolate the wind downward from the first model layer.

This boundary layer parameterization and the new moist convection parameterization lead to substantial improvements in atmospheric circulation [Druyan et al., 1995], compared to the older model II [Hansen et al., 1983a]. The geographical distribution of low-latitude precipitation is more realistic with these new parameterizations [Druyan et al., 1995], as is the vertical profile of heating [Del Genio and Yao, 1993]. Interhemispheric transport of tracers is faster and closer to observations [Rind and Lerner, 1996].

However, our present PBL model is still far from a realistic treatment of turbulent processes [Garratt, 1993; Ayotte et al., 1996]. We suspect that some of the greatest improvements to the climate model can be obtained via a more realistic PBL, and thus one of the foci of our current model development is the PBL representation.

3.3. Ground Hydrology and Evapotranspiration

The land surface parameterization in the SI95 model is described by Rosenzweig and Abramopoulos [1997]; their description includes a change in the snow calculation which was not included in SI95, as mentioned below. The land cover parameterization incorporates explicit modeling of the vegetation canopy and modeling of soil water flow through six soil layers, including underground runoff. Transpiration by plants and evaporation of intercepted precipitation and dew are included, as well as

evaporation from bare soil, as each grid box is divided into fractions of bare soil and vegetation cover. Objectives of the parameterization are not only to improve the accuracy of latent and sensible heat fluxes from the land surface but also to obtain more realistic physical and biological climate feedbacks.

Druyan et al. [1995] evaluated the effect of this land surface parameterization on the model's climatology, finding only marginal impacts, including a tendency for continental interiors to be too warm in the summer. Such a deterioration in model performance is not surprising. Hahmann et al. [1995] found that the Biosphere Atmosphere Transfer Scheme (BATS) surface parameterization caused similar but more severe problems in the National Center for Atmospheric Research general circulation model (NCAR GCM), because it exposed and magnified problems in the model's cloud cover and surface insolation.

Problems with the SI95 model, which are probably traceable to the land surface parameterization, include excessive snow buildup in about 10 grid boxes in mountainous central Asia and a general deficiency of runoff after heavy moist convection. The snow buildup was corrected subsequent to freezing the SI95 model by subdividing absorbed radiative fluxes into canopy and snow and by correcting an error in the snowmelt calculation [Rosenzweig and Abramopoulos, 1997], changes which will be included in the SI97 model. Improving the realism of the runoff, on the other hand, seems to be a fundamental difficulty requiring further model development.

3.4. Numerical Methods and Resolution

The horizontal resolution in the SI95 model is 4° by 5° (latitude by longitude). Vertical resolution is identical to model II, with nine layers in sigma coordinates and a rigid lid at the 10 mbar level [Hansen et al., 1983a]. Variables are defined on the "B grid," as in model II. Fourth-order numerical differencing is used for the momentum and mass equations [Abramopoulos, 1991]. A quadratic upstream scheme, equivalent to that of Prather [1986], is used for heat and moisture. A weak Shapiro filter is applied to the horizontal winds to remove high wave number noise.

The fourth-order calculations move waves faster [Rind and Lerner, 1996; Kalnay et al., 1977], and the quadratic upstream calculations reduce numerical noise and realistically maintain strong atmospheric gradients of tracers [Rind and Lerner, 1996]. These higher-precision calculations are included in SI95, but they are expensive in computing time. The fourth-order calculations increase the model computing time about 30%, and the quadratic upstream scheme increases it another 30%. Thus the merits of these numerical methods will be reassessed for SI97.

Preliminary tests with higher horizontal resolution (2° by 2.5°) do not yield much improvement in the model's climatology. However, the coarse vertical resolution may be seriously detrimental to our intended model applications. The SI95 model has only 1-2 layers in the stratosphere, which combined with the rigid model top and an arbitrary drag included in the top layer makes the simulation of the lower stratosphere unrealistic and calls into question experiments dependent upon stratosphere-troposphere interactions, as discussed below. Furthermore, the thick layers in the middle troposphere (ΔP about 160 mbar) and in the planetary boundary layer (two layers making up the lowest 130 mbar) also may constrain model capabilities. Thus higher vertical resolutions are being tested for the SI97 model.

3.5. Land Cover and Land Albedo

The SI95 model represents a large number of vegetation types as appropriate fractions of a small suite of vegetation types

[*Matthews*, 1984], as in GISS model II. However, changes are made in SI95 to incorporate cultivated land and to improve the realism of the surface albedo. The impact of agriculture is included via a data set for cultivation intensity [*Matthews*, 1983], which defines the cultivated fraction of cells at 1° resolution. Cultivated land is thus a separate category in the present model, with its characteristics defined presently as being the same as those of grassland.

The single albedo value for dry desert in model II (0.35) is replaced by surface albedo measurements from the International Satellite Cloud Climatology Project [*Rossow and Zhang*, 1995]. This generally increases the albedo in Saharan and Arabian regions and decreases it in arid regions of Australia, Asia, North America, and southern Africa.

The spectrally integrated albedo of deep fresh snow was 0.85 in model II, decreasing exponentially to 0.5 with a 5-day time constant as snow aged. With the small rate of snowfall in Antarctica this led to unrealistically low albedos and excessive warming. In the current model, snow ages only on those days in which the temperature of the top layer of the ground exceeds 0°C. The main impact of this change is in Antarctica, where it tends to keep the spectrally integrated albedo in the range 0.8-0.85, similar to observations [*Grenfell et al.*, 1994]. A sensitivity test shows that the new parameterization increases the mean surface albedo in Antarctica about 0.12, which cools the surface air about 10°C in summer and 5°C in the annual mean, resulting in a surface temperature close to observations.

3.6. Ocean Albedo

The SI95 model modifies ocean albedo to account for subsurface scattering and foam at high wind speed, based on a parameterization developed by one of us (H.G.). The contribution of subsurface scattering is included as a spectrally dependent reflectance [*Gordon and Clark*, 1981; *Gordon et al.*, 1988], for example, a maximum of 0.04 at 440 nm, 0.02 at 500 nm, 0.01 at 520 nm, 0.005 at 550 nm, and 0.001 at 600 nm. Incremental surface reflectance due to foam at high wind speeds is included via a term proportional to wind speed to the power 3.52 [*Koepke*, 1984; *Gordon and Wang*, 1994]. The net effect of these two terms added to the ocean reflectance is to increase the globally and spectrally integrated ocean albedo by 0.009 to 0.075, from the value 0.066 in model II, which included only Fresnel reflection from a wind-modified distribution of surface slopes [*Hansen et al.*, 1983a, equation (12)].

3.7. Sea Ice Albedo

Sea ice albedo is important because the large contrast between the albedo of ice and open ocean leads to a positive feedback during climate change. This feedback is enhanced, at least with model II physics, by a positive interaction between sea ice and cloud changes [*Hansen et al.*, 1997b]. These feedbacks tend to make the area of sea ice rather unstable. For example, we found that with the sea ice albedo of model II (0.55 in the visible, 0.3 in the near infrared, 0.45 spectrally integrated) the area of sea ice increased unrealistically, stabilizing with about 40% more sea ice than observed, when SST was computed in our Q flux ocean model.

A reduced sea ice albedo during the warm season, when it is most important because of large insolation, may be justified because of the effect of puddling or moistening of the ice. In the SI95 model we employ an extreme puddling parameterization by reducing the sea ice albedo when its temperature reaches the melting point to

$$A \text{ (sea ice)} = \begin{cases} 0.25 \ (\lambda < 0.7 \ \mu m) \\ \\ 0.10 \ (\lambda > 0.7 \ \mu m) \end{cases} \quad \text{if } T_{ice} > -0.1°C \quad (1)$$

which approximates measured albedos of wet sea ice in the Arctic [*Grenfell and Perovich*, 1984]. This leads to stable sea ice in our control run with the Q flux ocean but causes excessive absorption of solar radiation as judged by Earth Radiation Budget Experiment (ERBE) top-of-the-atmosphere observations [*Barkstrom et al.*, 1989; *Hansen et al.*, 1996a].

Recently, we have tested a more moderate puddling parameterization, which allows the albedo reduction to come into play gradually between 0°C and 10°C

$$A \text{ (sea ice)} = \begin{cases} 0.55 - 0.03 \ T_s \ (\lambda < 0.7 \ \mu m) \\ \\ 0.30 - 0.02 \ T_s \ (\lambda > 0.7 \ \mu m) \end{cases} \quad \text{if } 0 < T_s < 10°C \quad (2a)$$

$$A \text{ (sea ice)} = \begin{cases} 0.25 \ (\lambda < 0.7 \ \mu m) \\ \\ 0.10 \ (\lambda > 0.7 \ \mu m) \end{cases} \quad \text{if } T_s \geq 10°C. \quad (2b)$$

This moderate sea ice puddling parameterization yields better agreement with ERBE fluxes than the extreme puddling (Figure 1). Although elimination of puddling would perhaps achieve still slightly better agreement with ERBE, sea ice albedo observations
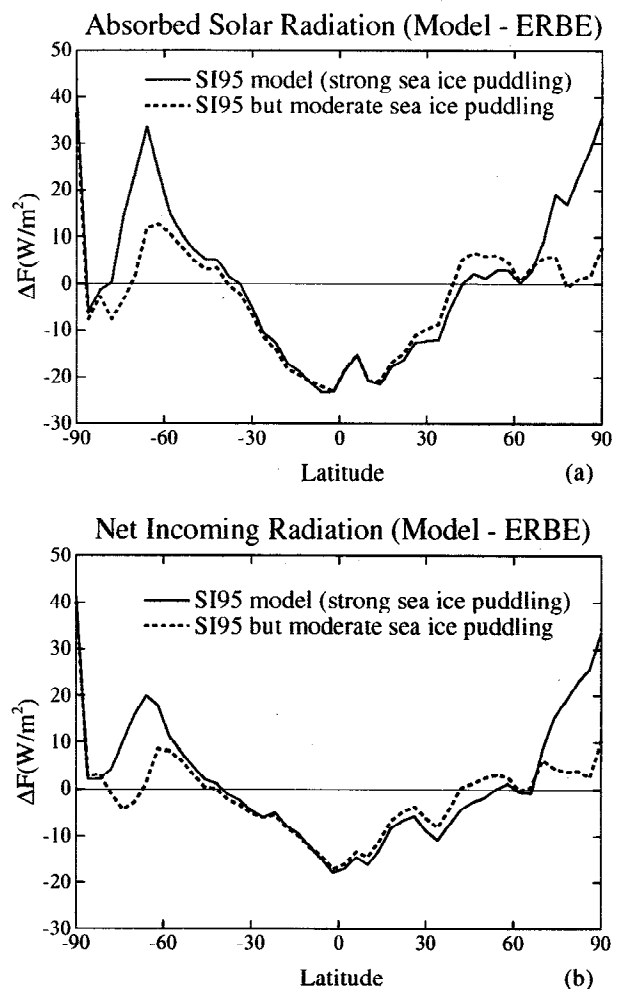

Figure 1. Difference between annual-mean radiation at the top of the atmosphere in Goddard Institute for Space Studies global climate model (GISS GCM) and in Earth Radiation Budget Experiment (ERBE) 1985-1989 observed climatology [*Barkstrom et al.*, 1989]. (a) Absorbed solar flux and (b) Net incoming radiation.

[*Barry*, 1996] argue for inclusion of a gradual puddling effect. The excess absorption of solar radiation at high latitudes that remains with the moderate sea ice puddling parameterization presumably is a result of deficient cloud albedo in the model, which in turn may be linked with the fact that the high-latitude troposphere is too dry in SI95.

We use the extreme puddling parameterization (1) in SI95 because the first runs were completed before the excess absorption was discovered; this parameterization also has the advantage of yielding a realistic sea ice cover in the control run of the Q flux ocean model. However, if the cloud cover in our model were larger at high latitudes, as suggested by some observations, the cloud shielding might reduce the impact of the ice/water albedo contrast, thus allowing stable sea ice cover with a moderate puddling parameterization. These issues are being investigated with the expectation of having more realistic clouds in the SI97 model and employing less extreme sea ice puddling.

3.8. Tropospheric Aerosols

The tropospheric aerosols in model II are the climatology of *Toon and Pollack* [1976], which was designed only as a global average representation. The Toon and Pollack aerosols have a global mean optical depth at 550 nm (τ_v) of 0.125, about 0.17 over land and 0.1 over ocean, with the spatial variation over land or ocean depending only on latitude. Global climate models will need to include realistic geographical distributions of several aerosol constituents to allow interactions with other climate variables. As an interim change, for SI95 we made the following changes to model II: (1) we replaced the Toon and Pollack sulfates with the global natural ($\tau_v = 0.025$) and anthropogenic ($\tau_v = 0.035$) sulfate distributions of *Langner and Rodhe* [1991] using Toon and Pollack's size distribution for both sulfate components; (2) we reduced the Toon and Pollack basalt optical depth by 50% and added in the global natural ($\tau_v = 0.017$) and anthropogenic ($\tau_v = 0.017$) desert dust distribution of *Tegen et al.* [1996].

3.9. Atmospheric Radiation

In model II, computing time is saved by calculating radiation only at every second grid box, with results at alternate grid boxes taken as the average of the neighbors. This introduces errors and complications in interpreting regional experiments, so radiation is calculated at every grid box in model SI95.

In model II, partial cloud cover is handled in the radiation calculations by assigning full cloud cover a fraction of the time. The procedure is to compare a random number between 0 and 1 to the calculated cloud cover, assigning full cloud cover for radiation if the random number is less than the cloud cover. In model II a single random number is used for all layers, thus yielding maximum cloud overlap and minimum total cloud cover. In SI95, when there are noncontiguous cloud layers, i.e., cloud layers separated by a cloud-free layer, a new random number is generated for each group of contiguous clouds. This semirandom cloud overlap procedure increases global cloud cover 0.9%, from 55.5 to 56.4%, with the largest increase (1.5%) at high northern latitudes.

The SI95 model control run has atmospheric composition appropriate for 1979. The temporal changes of CO_2, CH_4, N_2O, and the CFCs are specified in section 5.3. Ozone is longitudinally invariant but changes with height, latitude, and season according to the data of *McPeters* [1993], which is graphically displayed by *Hansen et al.* [1997b].

3.10. Solar Irradiance

In a trial run for SI95, using mean observed SSTs and sea ice for the 6-year period 1982-1987 (section 4) and solar irradiance

1367 W/m^2, the net radiation at the top of the atmosphere was out of balance by 0.4%. This imbalance is the net result of many approximations, uncertainties, and model errors. It is useful to remove this imbalance so that the model is in energy balance, thus tending to reduce drift in the simulations with calculated SST. Therefore we reduced the solar irradiance to 1362 W/m^2 for all of the model runs in Table 1.

3.11. Key Atmospheric Model Limitations

The present atmospheric model is extensively documented. Although the documented versions differ slightly, they all include the major changes in the boundary layer, moist convection, clouds, ground hydrology, and some of the more minor changes discussed above. The more minor changes are mainly radiative and do not substantially alter the general circulation. Surface, tropospheric, and stratospheric temperatures, including examples of interannual variability, surface winds, precipitation and the planetary radiation balance are compared with observations for both June-July-August and December-January-February by *Hansen et al.* [1996a]. *Rind and Lerner* [1996] illustrate the ability of the model to simulate the transport of atmospheric tracers. *Druyan et al.* [1995] test the model capabilities for simulating interannual atmospheric climate variations associated with El Niños, using observed SSTs. Additional tests of the atmospheric GCM are included in model development papers referenced above and in model intercomparison projects listed in the summary section below.

The model surface temperatures are too warm in some summer continental regions by about 5°C [*Hansen et al.*, 1996a, Figure 4], a problem related to the resistance of vegetation to excess evapotranspiration, perhaps caused by deficient clouds and excess solar heating of the surface [*Hahmann et al.*, 1995]. Surface temperatures in winter are too warm in northeastern Canada by as much as 10°C while being too cool in Greenland [*Hansen et al.*, 1996a, Figure 4], suggesting an inaccurate representation of atmospheric long waves. The extratropical upper troposphere is generally too cool by several degrees [*Hansen et al.*, 1996a, Figure 5; *Shah and Rind*, 1995]; water vapor is deficient at middle and high latitudes aloft, and thus large-scale cloud cover is deficient there. Interhemispheric transport of atmospheric tracers is marginally too slow, although close to the range of observations [*Rind and Lerner*, 1996, Table 3]. The following model limitations are perhaps the most crucial ones for the climate change studies in this paper.

3.11.1. Lower stratosphere. Many climate change mechanisms, such as changes of stratospheric aerosols, ozone amount, and ultraviolet solar irradiance, initiate in the lower stratosphere. The coarse vertical resolution in our model does not prevent delivery of reasonably accurate radiative forcings to the troposphere, but some climate change mechanisms depend upon stratosphere-troposphere dynamical interactions. For example, *Kodera and Yamazaki* [1994] present empirical evidence for tropospheric winter warming associated with large volcanic eruptions, attributed to changes in stratospheric temperature gradients and their influence on tropospheric long waves. *Robock and Mao* [1992] and *Graf et al.* [1994] present other empirical and modeling evidence tending to support this interpretation. Changes of ozone and solar ultraviolet irradiance could also alter stratospheric temperature gradients and thus affect the troposphere in a similar way. In general, stratosphere-troposphere interactions are sufficient to dictate great caution in drawing conclusions from a climate model which does not realistically represent the lower stratosphere.

The SI95 model cannot represent the lower stratosphere well, as this model has a rigid lid at 10 mbar, only 1-2 layers within the stratosphere, and a drag imposed in the top layer so as to damp wave

reflection from the model top and prevent excessive zonal winds [*Hansen et al.*, 1983a]. These constraints are alleviated in a 23-layer version of the GISS model [*Rind et al.*, 1988] but at the penalty of a large increase in computing time and with a degree of emphasis on the middle atmosphere that is inappropriate for our present tropospheric applications. Thus we are testing 12-17 layer versions of the current model for SI97, with several layers added in the stratosphere and tropopause regions, as well as possible small improvements in resolution of the boundary layer and middle troposphere. The effect on simulated climate change caused by the crude representation of the stratosphere in our present model can only be determined by repeating key experiments with a more realistic model. In the meantime, we interpret with caution climate change results dependent upon interactions with the stratosphere.

3.11.2. Surface fluxes.

Much of the uncertainty in predicting climate arises from our poor understanding and crude representation of the ocean's role in climate change. Indeed, this is why we employ several ocean models. However, the ocean simulations depend vitally on the realism of the fluxes of heat, moisture, and momentum delivered to the ocean surface by the atmospheric model. The SI95 model has deficiencies in its ability to provide accurate fluxes, which limits the conclusions that can be drawn from our experiments.

A telling inference of model inadequacies is provided by the global oceanic energy transports implied by the surface energy fluxes in the models. *Gleckler et al.* [1995, Figure 3a], compare several estimates of real world ocean transports, the mean of the estimates having northward transport in the northern hemisphere with maximum value about 2 PW at 24°N, the transport switching to southward at about 5°S. A recent comprehensive hydrographic analysis by *Macdonald and Wunsch* [1996] yields northward ocean transports 1.5 ± 0.3 PW at 24°N, 0.6 ± 0.3 PW at 47°N, and -0.9 ± 0.3 PW at 30°S.

The implied ocean transport in model SI95 is shown in Figure 2a. Although our model compares favorably with the 15 GCMs examined by *Gleckler et al.* [1995], southward transport in the southern hemisphere is less than observational estimates. This is not surprising, given the model's discrepancy with observed net radiative forcing at the top of the atmosphere (Figure 1). We expect that the factors required to improve the radiation balance will also improve the accuracy of energy fluxes into the ocean. Support for that expectation is provided by the test run with the improved sea ice puddling parameterization, equation (2), as shown in Figures 1 and 2a. Indeed, this change alone makes the implied ocean transports consistent with the observational estimates. However, this agreement may be fortuitous, as Figure 1 of this paper and the map of *Hansen et al.* [1996a, Figure 8] show that the model's short wave albedo is larger than observed over low-latitude oceans, and *Stone and Risbey* [1990] conclude that the poleward transport of energy by the atmosphere is too large in the GISS model. Our current model development includes a focus on those factors influencing cloud radiative forcing. Perhaps if the error in cloud radiative forcing is reduced, atmospheric and oceanic transports will become more realistic.

Consequences of the surface energy flux inaccuracy are dramatic in our dynamical ocean models: when sea ice cover is calculated, after several years most of the sea ice melts during the summer with either ocean model C (GISS) or D (GFDL) coupled to the SI95 atmospheric model. The *Q* flux ocean model is able to maintain stable sea ice, because its horizontal ocean heat transports are specified so as to yield observed ocean temperatures with the model-calculated surface fluxes. Indeed, a key objective of the *Q* flux approach is to try to minimize the damage caused by imprecise surface fluxes, but we cannot be certain that the model's sensitivity
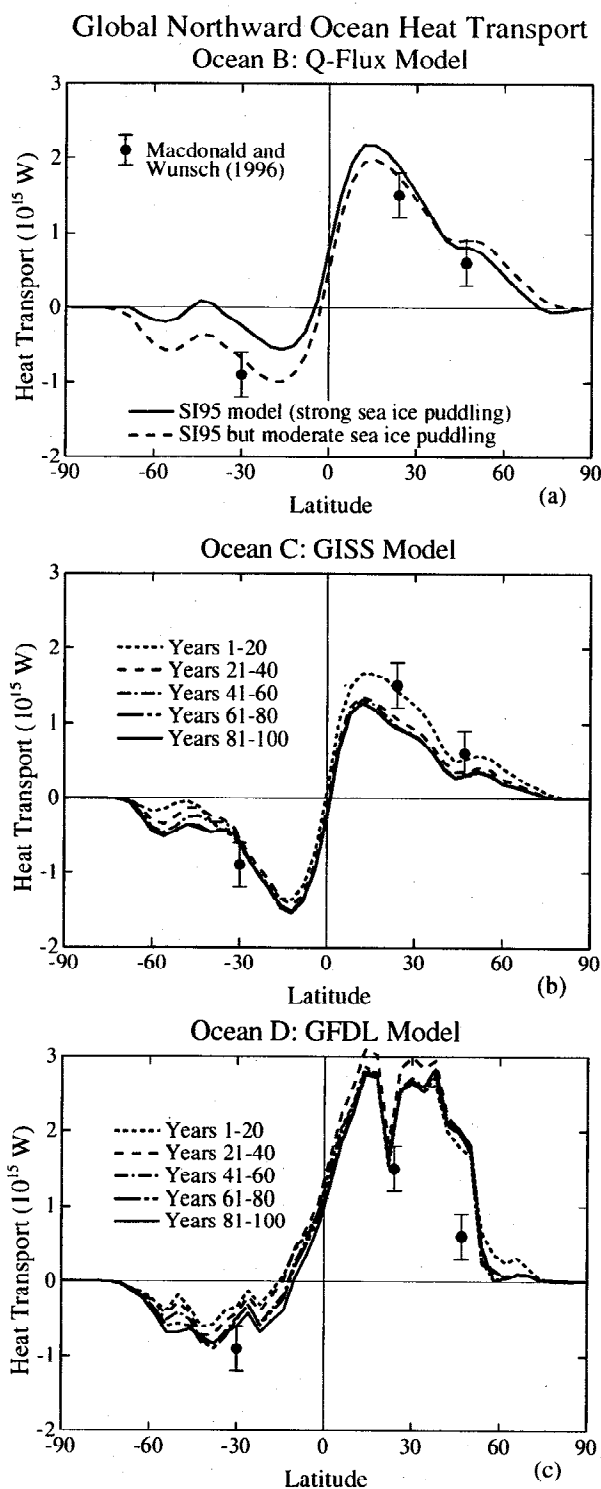

Figure 2. (a) Ocean heat transport used in ocean B, calculated as the implied transport using observed sea surface temperatures (SSTs); the solid curve is the transport used here, while the dashed curve is the transport obtained using equation (2) sea ice puddling parameterization. Figures 2b and 2c show the heat transport in 20-year intervals of the control runs of the dynamically interactive oceans C and D.

is not altered by this procedure of sweeping surface flux errors into horizontal transports, and of course the *Q* flux model is incapable of yielding information on ocean dynamical feedbacks.

The ocean models also depend vitally on the momentum and freshwater fluxes provided by the atmospheric model. The SI95

model delivers qualitatively realistic surface wind stress fields, judged by comparison with the analyses of *Hellerman and Rosenstein* [1983], although tropical easterlies are weaker than observations by about one third, while the middle-latitude surface wind stress is about twice the observed strength in the southern hemisphere but within 20% in the northern hemisphere. The distribution of model freshwater fluxes is in qualitative agreement with the analyses of *Oberhuber* [1988], with freshening at high latitudes and under the Intertropical Convergence Zone (ITCZ) balanced by net evaporation in the rest of the tropics. There is an indication that subtropical evaporation may be too large by one third and that freshening in the ITCZ is underestimated by one quarter in the Pacific, although observed rainfall estimates are uncertain. Errors also occur in the freshwater input from rivers to the ocean, with the greatest error in the GISS model being for the Amazon, which delivers only about half of the volume indicated by observations [*Miller et al.*, 1994].

    3.11.3. Summary. Despite the model limitations it seems worthwhile to carry out the set of planned experiments. At the least, this process will help define improved procedures for future experiments. It also provides a baseline which will help in testing the endurance of inferences about climate change as models improve, one of the elements in our strategy of investigation (section 2.8).

    Furthermore, model intercomparisons suggest that our current model is representative of the state of the art. In GCM radiation comparisons with line-by-line calculations [*Cess et al.*, 1993] the GISS model was found to be one of the most accurate. The same conclusion follows from the intercomparison of cloudiness and its variability in a large number of GCMs [*Weare et al.*, 1995], as well as intercomparison of seasonal changes in cloud radiative forcing in GCMs [*Cess et al.*, 1996]. We already noted above that the implied ocean transport (Figure 2a) is more realistic in the GISS GCM than in most of the 15 models presented by *Gleckler et al.* [1995]. A comparison of the hydrologic processes in 29 GCMs with observations ranks the GISS model in the upper quartile of the models [*Lau et al.*, 1996]. Comparison among 30 GCMs of the amplitude and seasonality of precipitation over the United States showed the GISS model to be one of the most realistic, with a fidelity similar to that of the 19-layer T42 model of the Max Planck Institute [*Boyle*, 1996]. The atmospheric humidity in the GISS model is lower than observed [*Gaffen et al.*, 1997], although such a deficiency is common to many of the AMIP GCMs.

    Thus the model flaws are more a commentary on the state of the art than a condemnation of the SI95 model. We stress our model limitations as a warning against indiscriminate use of the climate simulations. However, it is inappropriate to use the existence of model deficiencies as a reason to denigrate all model results as untrustworthy. Recognized model limitations need not prohibit effective use of the models for climate analyses.

4. Ocean Representations

4.1. Ocean A: Observed SST and Fixed Sea Ice

    Prior to defining the SI95 model, we carried out simulations for 1979-1993 with the predecessor model, SI94 [*Hansen et al.*, 1996a], employing the SST and sea ice boundary conditions of the Atmospheric Model Intercomparison Project (AMIP) [*Gates*, 1992]. These boundary conditions produced a global surface air warming of 0.24°C/decade, much greater than observed warming of about 0.1°C/decade [*Hansen et al.*, 1996b]. The large warming rate was traced to sea ice changes in the AMIP boundary conditions,

which were formed by concatenation of three sea ice data sets, with discontinuities at the end of 1981 and the end of 1987.

    Satellite microwave data [*Gloerson et al.*, 1992] provide reasonably homogeneous data for sea ice cover. These data indicate that observed interannual variability of sea ice cover is an order of magnitude smaller than the discontinuities in the AMIP data. In order to avoid a large spurious climate forcing, we use the mean seasonal cycle of sea ice of the AMIP data. Thus sea ice is not a forcing in our ocean A experiments.

    We use AMIP SSTs for 1979-1988 and the recent OI (optimum interpolation) SST analysis of *Reynolds and Smith* [1994] for 1989-1996. Thus the SST in sea ice regions has some inconsistency with the sea ice distribution. This inconsistency should have little effect on global average climate, but the simulated interannual climate variations in and around the sea ice regions may be affected, so our results are examined with that possibility in mind.

    In future modeling studies, it would be useful to include interannual variability of sea ice based on a homogeneous analysis of satellite microwave data. Sea ice changes may contribute to interannual climate variability, and also there is evidence of recent decadal trends of sea ice cover, especially in the Arctic [*Johannessen et al.*, 1995; *Maslanik et al.*, 1996]. It is desirable that the sea ice used in the derivation of SSTs [*Reynolds and Smith*, 1994] be the same as that used in the modeling studies. Care is required to avoid a discontinuity in sea ice at the transition from ship data to satellite plus ship data.

4.2. Ocean B: Q flux Model

    In our Q flux ocean model the horizontal transport of heat in the ocean is fixed. As in the model of *Hansen et al.* [1988], the ocean heat transport is calculated from the divergence of energy at each grid box in a control run. The control run specified 1982-1987 mean seasonally-varying SSTs and climatological seasonally varying ocean mixed layer depths, with the global-mean annual-maximum depth being 109 m. The method of calculating the implied ocean heat transport is described in detail by *Russell et al.* [1985]. The resulting zonal-mean ocean heat transport is shown in Figure 2a and discussed in section 3.11.

    In our transient experiments with the Q flux ocean, heat anomalies in the mixed layer are diffused into the deeper ocean with a geographically varying diffusion coefficient. The value of the diffusion coefficient k is based on an empirical relation between the observed penetration of passive tracers and the climatological stability at the base of the mixed layer, as described by *Hansen et al.* [1984]. The value of k varies from about 0.2 cm^2/s at low latitudes to about 10 cm^2/s in the North Atlantic Ocean and around Antarctica, as shown by [*Hansen et al.*, 1984, Figure 15a]. The global ocean mean of k is about 2.5 cm^2/s, but the value of k required in a one-dimensional model to yield an equivalent vertical heat transport is about 1 cm^2/s [*Hansen et al.*, 1984].

    The Q flux ocean model does not allow dynamical feedbacks between climate change and ocean dynamics. Thus this "surprise-free" ocean excludes the possibility of shifts in ocean circulation or in the rate of deep water formation. We have speculated that it may underestimate the rate of heat exchange with the deep ocean after a large cooling perturbation, such as the Pinatubo volcanic eruption [*Hansen et al.*, 1996a]. Nevertheless, given problems that beset the current generation of dynamically interactive ocean models, as described below, it is possible that this model still provides the best current estimate of decadal transient global climate change. At any rate it provides a useful comparison for other ocean models.

We run the Q flux model with both calculated sea ice and specified (AMIP mean 1982-1987) sea ice. Specified sea ice provides precise comparison with oceans A, C, and D, which all use fixed sea ice, while calculated sea ice allows investigation of the sea ice climate feedback. Although the simple thermodynamic sea ice calculations of model II are known to yield a significant positive climate feedback at equilibrium [*Hansen et al.*, 1984; *Rind et al.*, 1995], we show below that the impact of calculated sea ice is small in our present 17-year transient simulations.

4.3. Ocean C: GISS Model

The "GISS ocean model" is as described by *Russell et al.* [1995], except here it is coupled to the SI95 atmospheric model. The ocean model has 4°×5° resolution, defines variables on the C grid, and moves potential enthalpy and salt with a linear upstream scheme which incorporates subgrid scale linear gradients in three dimensions [*Russell and Lerner*, 1981], thus effectively increasing the resolution. The model has up to 13 layers in the vertical, with each successively deeper layer increasing in thickness by 50%, with the top layers being 12, 18, 27, 40.5, and 61 m. Thus the ocean mixed-layer typically has three to five layers.

The model is run without flux adjustment; but because of the excessive solar heating at high latitudes generated by the atmospheric model (section 3.7), which would tend to melt most of the sea ice, we employ the same fixed climatological sea ice as in ocean model A. The ocean physics includes convection, vertical diffusion, and bottom friction. The resulting effective annual-mean horizontal-mean vertical diffusion varies from about 5 cm^2/s at the top of the mixed layer to 0.25 cm^2/s at the bottom of the mixed layer, and is about 0.15 cm^2/s throughout most of the ocean.

The ocean model conserves water mass, allowing for divergent flow, with a free upper surface. River flow is added to the ocean at appropriate places, altering the ocean height. The atmosphere and ocean models are truly synchronously coupled, with joint physical processes occurring every hour. A disadvantage of the model, compared with the classical model described below, is that it is slower and cannot practically be run for thousands of simulated years. The current version of this ocean model requires about 35% as much computing time as the atmospheric model. This is not an undue burden for a synchronously coupled model, and furthermore, programming efficiencies have been identified which can reduce this to about 25%. Thus we anticipate that it may be practical to use higher horizontal resolution within the ocean when it is coupled to the SI97 atmospheric model.

The poleward heat transport in the first 20 years of the control run of the ocean C model coupled to the SI95 atmospheric model (Figure 2b) is in close agreement with the observational analysis of *Macdonald and Wunsch* [1996]. The ocean transport weakens in later decades, consistent with the fact that SI95 delivers too little solar heating to the ocean at low latitudes and too much at high latitudes (Figure 1).

4.4. Ocean D: GFDL Model

The "GFDL ocean model" is the classical model of *Bryan* [1969] and *Bryan and Cox* [1972], based on the computer code of *Cox* [1984]. However, because of minor alterations in its implementation, the model performance characteristics we find are not representative of model capabilities in applications carried out at GFDL. In particular, we chose to distribute surface heat fluxes throughout the mixed layer, discovering later that this made the interannual variability of SSTs less realistic (section 7.1).

The present implementation of this model [*Miller and Jiang*, 1996] has 4°×5° resolution with 16 layers concentrated toward the

surface, the top layer being 30 m thick. The ocean mixed layer typically has 2 to 3 layers.

The model is run without flux adjustment. We employ the same fixed climatological sea ice as in ocean models A and C, thus avoiding unrealistic retreat of sea ice which the SI95 atmospheric model would tend to generate. Diffusion of heat is that described by *Bryan and Lewis* [1979], vertical diffusion increasing from 0.3 cm^2/s at the surface to 1.3 cm^2/s in the deep ocean and horizontal diffusion decreasing from 10^7 at the surface to 0.5×10^7 in the deep ocean. The momentum diffusion coefficients were tuned, to 20 cm^2/s in the vertical and 4×10^9 in the horizontal, to optimize heat and mass transports when used with an earlier version of the GISS atmospheric model [*Miller and Jiang*, 1996], but the effect of these changes was small.

The poleward heat transports in the ocean model when it is coupled to the SI95 atmospheric model are shown in Figure 2b. The simulated transports are apparently too large in the northern hemisphere, despite the deposition of too little solar energy into the low-latitude oceans. The double hump in the transport, with a minimum near 20°N, is associated with meridional overturning cells in the simulated Pacific Ocean.

Our present implementation of the GFDL ocean model requires only about 11% as much computing time as the atmospheric model. Thus we anticipate use of higher horizontal resolution with this ocean model when it is coupled to the SI97 model.

5. Control Runs

5.1. Variability

The unforced interannual variability of global-mean annual-mean surface air temperature in the four control runs is shown in Plate 1a. The 17-year standard deviations are indicated for all four oceans. As may be hoped, the largest variability ($\sigma = 0.09$°C) is for ocean A (observed SSTs), since only in this case is there any influence of the real-world time-dependent climate forcings. Also as expected, ocean B (Q flux), with dynamical transports identical each year, is the least variable ($\sigma = 0.04$°C). The relatively high variability ($\sigma = 0.07$°C) of ocean C (GISS model) may arise in part from its C grid differencing scheme for momentum, which tends to generate alternating patterns in the large-scale vertical mass flux [*Russell* et al., 1995], as well as from the absence of explicit horizontal diffusion. The smaller variability ($\sigma = 0.06$°C) in ocean D (GFDL model) may result in part from the fact that (in the ocean D implementation here) surface fluxes are deposited uniformly through the mixed layer rather than only in the top layer, as well as from the relatively large vertical and horizontal diffusion. Different vertical convection schemes in oceans C and D may also contribute to their variabilities.

5.2. Drift

The 100-year standard deviations are indicated in Plate 1a for the three long runs (oceans B, C, D). In order to eliminate the effect of long-term drift of the mean surface temperature, we also calculate the standard deviation about the linear trend of the global temperature, represented by σ^*; σ^*_{100} is similar in value to σ_{17}.

Drift of the global mean temperature occurs with all the ocean models, as it was impractical to have long spin-up runs with atmosphere and full oceans synchronously coupled. Ocean B calculates only temperature anomalies; its initial ocean condition was zero temperature anomaly everywhere. Ocean C had no spin-up; its initial ocean condition was the climatology of *Levitus et al.* [1994]. Ocean D was spun up for 5000 years using the wind
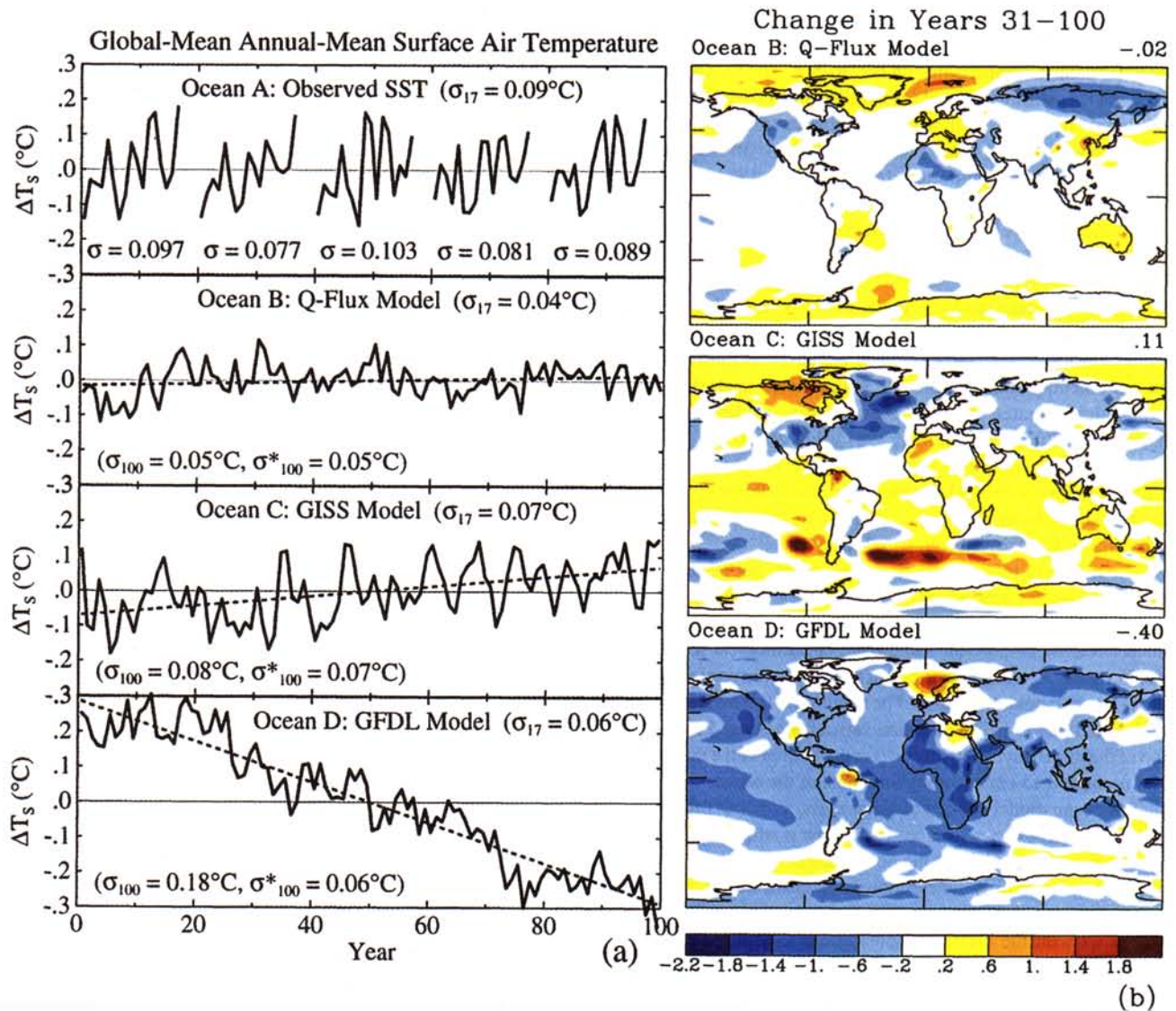
Plate 1. (a) Global-mean annual-mean surface air temperature in control runs using four ocean models. Ocean A (observed SST) is limited to 17 years of observed ocean data (1979-1995) but has five independent runs; σ_n is the standard deviation of the surface air temperature about the n year mean, and σ^* is the standard deviation about the linear trend. For the 100-year runs, σ_{17} is the mean of 84 17-year standard deviations, each calculated relative to their 17-year mean. (b) Surface air temperature change (drift) in years 31-100 of control runs of three ocean models.

stress from the GISS atmospheric model (section 3 above) but relaxing the sea surface salinity and SST to the climatology of *Levitus* [1982].

Ocean drift can hinder the search for impacts of small radiative forcings. We begin all experiments near the end of the control runs, at year 80, to allow ocean heat transport to stabilize and to reduce drift. We initiate at year 80 two sets of five control runs: set a has no radiative forcings and set a' has only a constant 0.65 W/m² forcing. The experiment runs b, c, d, and e include the 0.65 W/m² forcing. Thus by using run a (a') as the control, we obtain the estimated climate effect with (without) the 0.65 W/m² forcing.

The constant 0.65 W/m² forcing was introduced by the replacement of an efficient but less precise radiation routine with one capable of accurate calculation of the time-variable radiative forcings. The model's time-dependent and equilibrium responses to this forcing are summarized in Appendix A. Although the 0.65 W/m² forcing was introduced inadvertently, it was fortuitously

similar in magnitude to suspected initial disequilibrium forcing in 1979, as discussed in the next section, and it yields a quantitative estimate of the climate effect of an initial disequilibrium.

6. Climate Forcings

6.1. Stratospheric Aerosols

Climate forcing by stratospheric aerosols, if defined as the change of net radiation at the tropopause, depends principally upon the spectrally dependent aerosol optical depth [*Lacis et al.*, 1992; *Hansen et al.*, 1997b]. This aerosol climate forcing, which causes surface and tropospheric cooling, should be accurately represented in our present experiments, as it is insensitive to minor uncertainties in the aerosol size distribution. A secondary climate influence of the aerosols comes via their warming effect in the stratosphere, which could alter atmospheric dynamics and thus also affect the surface
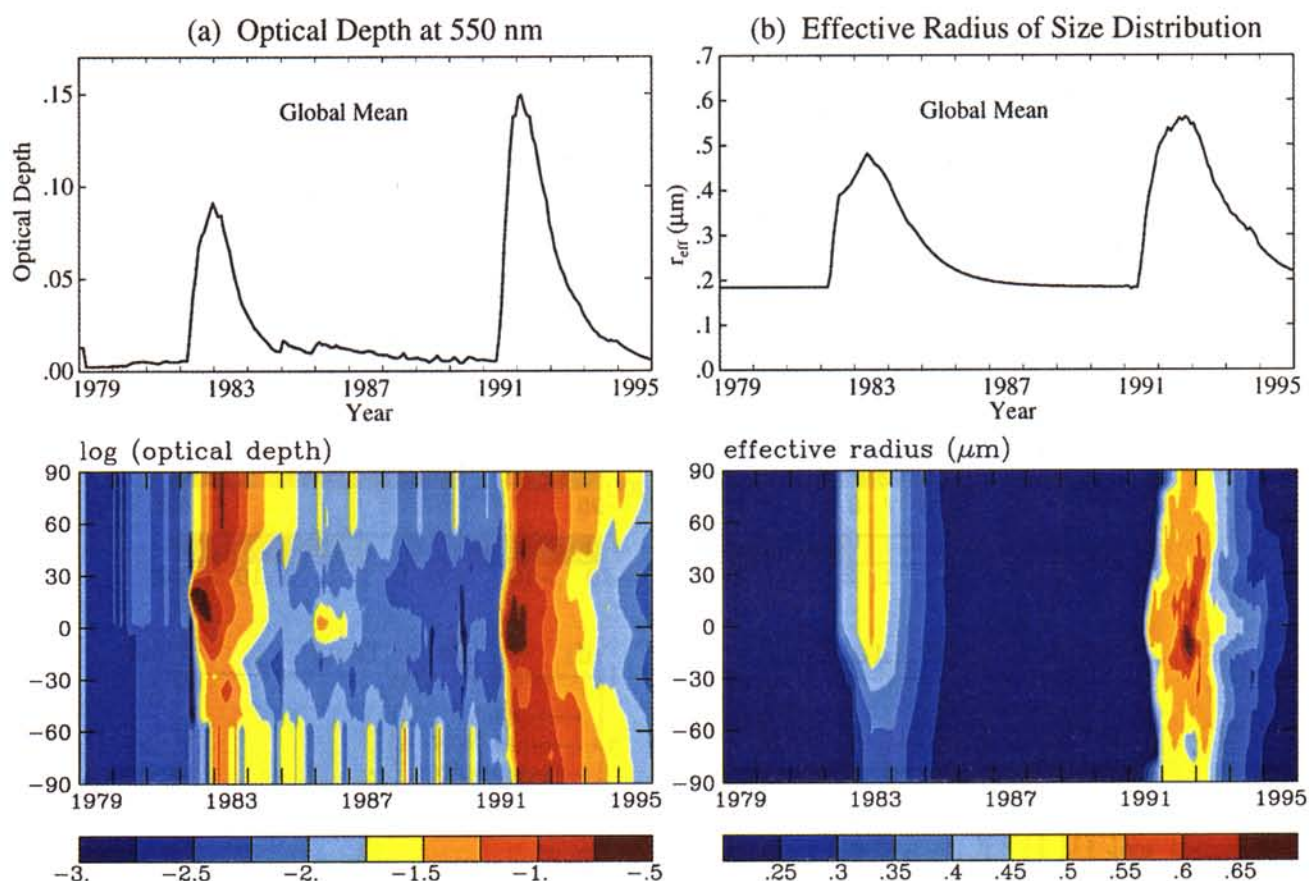
Plate 2. (a) Global mean stratospheric aerosol optical depth at wavelength 550 nm and (b) effective radius of aerosol size distribution employed in simulations with SI95 model. The bottom panel shows the variation of these parameters with latitude.

and troposphere. This secondary forcing depends upon the large particle tail of the aerosol size distribution and upon the possible presence of absorbing aerosols; these characteristics may be inaccurately represented in our present experiments. Moreover, the SI95 model's upper boundary conditions and coarse vertical resolution make the present model poorly suited for simulating stratospheric dynamical effects (section 3.11).

The stratospheric aerosol properties we employ for the period after the Pinatubo eruption are the same as those we used with the SI94 model [*Hansen et al.*, 1996a]. They were derived by one of us (AAL), as discussed by *Hansen et al.* [1996a], from solar occultation measurements of optical depth made by the Stratospheric Aerosol and Gas Experiment (SAGE II) at four wavelengths, assuming a monomodal gamma size distribution independent of height with the (assumed time independent) width of the distribution constrained by satellite measurements at 12.1 μm [*Lambert et al.*, 1993]. The resulting global mean aerosol optical depth at 0.55 μm (Plate 2a) peaked at about 0.15 about 6 months after the Pinatubo eruption, and the effective radius was 0.5-0.6 μm during the time of large aerosol amount (Plate 2b). The Pinatubo aerosol properties obtained in this way are in good agreement with analyses of multiple data sources by *Russell et al.* [1996].

SAGE occultation measurements are available for much of the earlier period, 1979-1990, but not immediately after the 1982 El Chichon eruption. We use optical depths of *Sato et al.* [1993] for the period prior to Pinatubo, but in the 4 years after El Chichon, we increase the optical depth of *Sato et al.* [1993] by 10% based on an analysis of multiple data sources provided by J. Pollack and P.

Russell at Ames Research Center (private communication, 1995). The effective aerosol radius after El Chichon, Plate 2b, was deduced from several measurement sources by Pollack and coworkers. We take the aerosols as being a 75% solution of sulfuric acid. Silicate ash may have been significant during the first few months after the eruptions, especially after El Chichon [*Snetsinger et al.*, 1987], but it is in effect replaced by sulfuric acid in our present simulations. The resulting climate forcing is illustrated below and compared with other forcings. The stratospheric aerosol optical depth time series, including latitudinal dependence, is available via www.giss. nasa.gov/Data/STRATAER.

6.2. Ozone

The climate forcing due to ozone change depends mainly on the change of the ozone vertical profile [*Lacis et al.*, 1990; *Hansen et al.*, 1997b], which has not been measured accurately. We patch together a profile of ozone change using data from several sources. Because there are uncertainties in the data, we emphasize that the resulting SI95 ozone change experiments should be viewed as sensitivity studies, hopefully stimulating the construction of a more precise ozone change data set.

We use the ozone climatology of *McPeters* [1993], based on 1979-1980 measurements, in our control runs. Our ozone change is based on a combination of solar backscatter ultraviolet (SBUV) [*Hollandsworth et al.*, 1995a], SAGE II [*McCormick et al.*, 1992], and ozonesonde [*Logan*, 1994] data. We use SBUV to specify time dependence of total ozone (i.e., column amount) and the profile of change at altitudes above the 32 mbar level, SAGE II to specify the
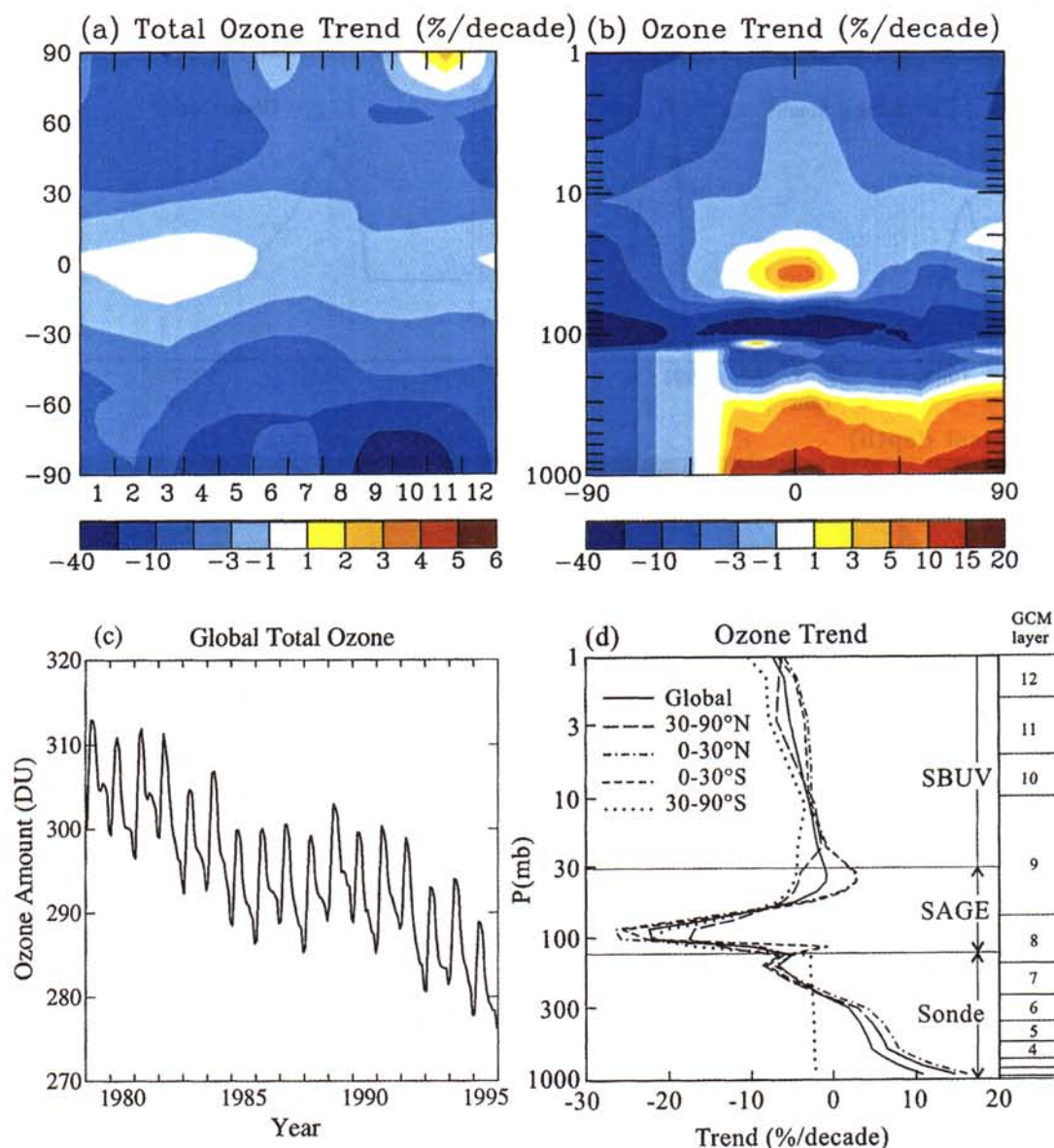
Plate 3. Ozone changes used in ozone forcing experiments with SI95 model: (a) trend of column-integrated ozone versus month and latitude, (b) trend of annual-mean ozone versus height and latitude, (c) global-mean total ozone versus time, (d) global ozone trend versus height.

profile of ozone change between 32 and 125 mbar, and the mean of the sonde profiles to specify a trend for tropospheric change at latitudes 90°N to 30°S, with a first guess of no tropospheric change at latitudes 30°S to 90°S. After the three sources of profile data are combined, a small correction (proportional to the climatological profile) is added to the ozone amounts at altitudes below 32 mbar to make the column ozone amount agree exactly with the SBUV total ozone. We do not use SBUV data per se but rather the "model" of *Hollandsworth et al.* [1995a, b], including solar and quasi-biennial oscillation (QBO) variations, which is fit to the SBUV data. Our ozone amount is not identical to Hollandsworth's model, because we added a small offset to make her 1979-1980 ozone amounts agree exactly with those of *McPeters* [1993], because his climatology for 1979-1980 was used in our control runs.

The resulting ozone change for our SI95 experiments is shown in Plate 3. It is uncertain whether the actual ozone change is as sharp near the tropopause as indicated by SAGE II [*World Meteorological*

Organization (WMO), 1994]. However, the coarse vertical resolution of our model smears out the ozone change into thick layers indicated in the right-hand side of Plate 3d. The climate forcing associated with this ozone change is presented and discussed below and also discussed by *Hansen et al.* [1997b].

6.3. Homogeneously Mixed Greenhouse Gases

The assumed changes of CO_2, CH_4, N_2O, CFC-11 and CFC-12, specified in Table 2, are similar to those in the *Intergovernmental Panel on Climate Change (IPCC)* [1995]. For the years 1996-1999 the annual increments are fixed at 1.4 ppm for CO_2, 8 ppb for CH_4, 0.6 ppb for N_2O; CFC-11 and CFC-12 changes are assumed to be negligible in that period. The CO_2 change is uniform with height. The other changes are uniform to altitude 16 km, falling off at higher altitudes with a 10 km scale height.

In addition to these five gases that we model explicitly, we include a forcing of 0.01 W/m^2 per year as an approximation for all

Table 2. Tropospheric Annual-Mean Amounts Assumed for Well-Mixed Greenhouse Gases in SI95 Model

Year	CO_2, ppm	CH_4, ppb	N_2O, ppb	CFC11, ppt	CFC12, ppt
1979	335.6	1561	301.0	152	286
1980	337.7	1574	301.2	162	305
1981	339.2	1587	302.4	171	320
1982	340.3	1600	303.4	179	339
1983	342.3	1613	304.0	188	355
1984	343.6	1626	304.8	194	372
1985	345.0	1639	305.0	202	389
1986	346.5	1652	306.0	213	406
1987	348.0	1665	305.8	224	425
1988	350.2	1675	306.4	238	448
1989	351.7	1685	308.3	245	465
1990	352.8	1693	308.8	253	479
1991	354.0	1705	309.6	257	492
1992	354.8	1713	310.9	263	503
1993	355.8	1715	311.0	264	513
1994	357.1	1723	311.5	263	517
1995	358.6	1733	312.2	263	517

other increasing trace gases. The net effect of minor halocarbons provided a forcing of about half that rate in the 1980s [*Hansen et al.*, 1989]. Stratospheric H_2O may be increasing [*Oltmans and Hofmann*, 1995], indeed an increase is expected from oxidation of increasing CH_4 [*Lelieveld et al.*, 1993], but its climate forcing is estimated to be small by *IPCC* [1995]. Some other gases known to be changing, such as CO, also have small forcings. If the effect of these and other unmeasured trace gases is negligible, then the allowance we have included (0.17 W/m^2 over 17 years) may be 50% too large. In that event our forcing for well-mixed greenhouse gases is too large by 10-15%.

6.4. Solar Irradiance

We include solar irradiance changes (Figure 3) based on an analysis of satellite measurements by one of us (JLL). Total solar irradiance has been measured over almost the full period of our simulation. The spectral distribution of variability in the ultraviolet region has been measured over a sufficient portion of the solar cycle to allow reasonable inference of the spectral distribution of variability in the past solar cycle [*Lean et al.*, 1997]. We divide the spectrum into three intervals: less than 0.295 μm, between 0.295 and 0.31 μm, and greater than 0.31 μm. The range of solar variability over the solar cycle within these three spectral intervals is about 1, 0.3, and 0.07%, respectively. As these intervals contain about 0.95, 0.65, and 98.4% of the solar irradiance, the proportions of the solar variability associated with these three intervals are about 12, 2, and 86%, with the intervals in the order of increasing wavelength. For a typical solar zenith angle, solar radiation in these three intervals is absorbed above layer 9 (i.e., above the 10 mbar level), within layer 9 (between 10 and 70 mbar), and beneath layer 9.

Thus most of the energy associated with solar variability is deposited below the tropopause, but it is conceivable that the small forcing in the stratosphere can alter significantly stratospheric temperatures and winds. In addition, there is an indirect solar climate forcing via changes of ozone over the solar cycle. This latter forcing is included in our specified ozone changes, as discussed above. We show elsewhere [*Hansen et al.*, 1997b] that the radiative

forcing associated with the solar cycle ozone change is about a factor of 3 smaller than the direct solar cycle radiative forcing. Despite the small magnitude of these direct and indirect solar cycle forcings, *Haigh* [1996] finds that these forcings reproduce some aspects of observed climate variations, albeit with a smaller magnitude than observed, in a perpetual January climate simulation.

The SI95 climate model may not be able to realistically simulate the climate response to either of the stratospheric forcings associated with the solar cycle, because of its crude representation of the stratosphere, as discussed above. The model should be well suited for simulating the effect of the 86% of the irradiance variability affecting the troposphere.

6.5. Forcings not Explicitly Included

Several other radiative forcings, especially tropospheric aerosols and land use changes, may be important on decadal timescales. These forcings may be unimportant on global average for the period 1979-1996 but they are probably significant on regional scales and should be included in quantitative analyses. However, they are excluded in our present GCM simulations, because of a lack of defining data.

Anthropogenic aerosols, especially sulfates, organic aerosols, and soil dusts, may be an important climate forcing on the century timescale [*IPCC*, 1995]. We estimate that the global direct radiative forcing due to all anthropogenic aerosols is at most a (negative) few tenths of 1 W/m^2 over the past century [*Hansen et al.*, 1997a]. This corresponds to a magnitude no more than 0.1 W/m^2 globally for 1979-1996, but probably less because aerosol amounts decreased in some regions. Even more uncertain is the indirect radiative forcing by aerosols, i.e., their influence on cloud properties, which we argue is probably larger than their direct effect [*Hansen et al.*, 1997a]. GCM simulations on the century timescale have been made including both direct and indirect aerosol forcings [*Hansen et al.*, 1993; *Taylor and Penner*, 1994; *Mitchell et al.*, 1995], but these are probably best regarded as sensitivity studies. There is empirical evidence of a thermal response with a spatial pattern corresponding to the expected distribution of sulfate aerosols [*Karl et al.*, 1995; *Hansen et al.*, 1997a], but such a local response pattern would occur nearly independently of the aerosol single-scatter albedo, which however is crucial for determining the global aerosol effect [*Hansen et al.*, 1997b]. We conclude that any presumed aerosol forcing in
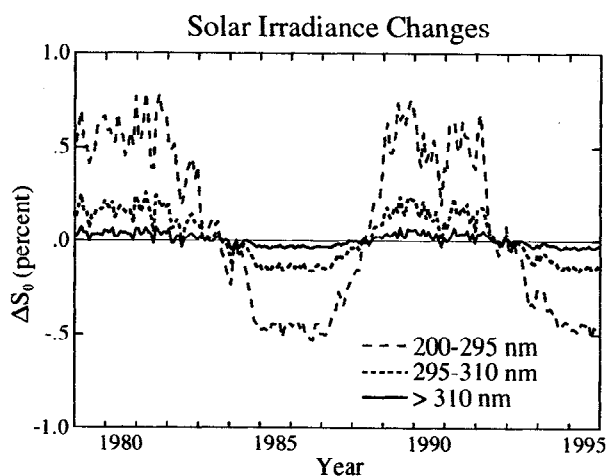

Figure 3. Solar irradiance changes (relative to 1985-1994 mean) used in solar irradiance climate forcing experiments with SI95 model. Solar irradiance in SI95 experiments for dates from January 1995 onward is a (10 years) cyclic repetition of 1985-1994 data.

our present experiments would be arbitrary, but it is important to obtain measurements that define aerosol forcing for future simulations.

Land use change is another potentially significant forcing, especially on regional scales. As a sensitivity study, we replaced the "natural" vegetation distribution [*Matthews*, 1984] in our GCM with a data set incorporating modern land use, i.e., cultivation [*Matthews*, 1983]. This was a crude test, as areas under cultivation were simply defined to have "grassland" characteristics [*Hansen et al.*, 1983a]. The model was run first with fixed SSTs, revealing that the global mean radiative forcing due to anthropogenic land use is -0.4 W/m^2, a significant forcing. However, *Hansen et al.* [1997b] show that all forcings are not equivalent, and specifically, midlatitude land use forcing should be only about half as effective as a greenhouse gas forcing of the same magnitude. We confirmed this by making a 50-year run with the land use change, obtaining an equilibrium global cooling of -0.2°C. Further, no more than half of the land use change, corresponding to -0.1°C, is believed to have occurred this century. We conclude that it is desirable to include land use forcings, whose effect is most likely to be noticed on a regional scale; but the global effect is probably small for 1979-1996 and is not included in our present simulations.

6.6. Initial Disequilibrium Forcing

A key issue with climate simulations initiated during a time of changing forcings, especially simulations as brief as 17 years, is whether the planet was in radiation balance at the beginning of the experiment. Indeed, there is reason to expect that the planet had a positive radiation balance (net incoming radiation) in 1979 [*Hansen et al.*, 1984], because greenhouse gases increased rapidly in prior years. The long response time of the ocean [*Hansen et al.*, 1985] (see also Appendix A below) implies that ocean temperature would not keep pace, i.e., stay in thermal equilibrium, with atmospheric composition. This issue, discussed by *Hansen et al.* [1988] and *Hasselmann et al.* [1993], is sometimes called the "cold start" problem.

The cold start problem can be ameliorated simply by adding a constant radiative forcing equal to the estimated disequilibrium at the start of the run. This is not a perfect solution, as the true transient situation would have some profile of temperature anomalies within the ocean, but it should provide a first-order correction for the energy imbalance. The magnitude of the initial disequilibrium depends upon climate sensitivity and upon the history of all forcings prior to 1979, thus, for example, upon aerosol changes as well as greenhouse gases. *Hansen et al.* [1993] made a large number of simulations for the period 1850-1995, with different climate sensitivities and different forcings, concluding, from the models which fit observed century timescale and post-Pinatubo temperatures best, that the recent energy imbalance is probably about 0.5 W/m^2.

The actual disequilibrium (or energy imbalance) of the Earth varies from year to year because of chaotic fluctuations of global temperature. We could most easily obtain an estimate of the disequilibrium if we initiated our simulations at a time when the global temperature was typical of the previous few years, rather than at an extreme. Our simulations began in 1979, right after a rather sudden jump of global temperature by about 0.2°C. A temperature change of 0.2°C corresponds to a forcing of about 0.25 W/m^2, if climate sensitivity is about 3.5°C for doubled CO_2 (a forcing of about 4.2 W/m^2). However, this is an overestimate of the uncertainty in the disequilibrium introduced by chaotic fluctuations, because the quantity of greatest relevance is the heat content of the upper ocean, not the mean surface temperature of the globe, and the ocean heat content is not so noisy as the surface temperature.

Thus it is meaningful to search for and attempt to quantify a disequilibrium if it is larger than a few tenths of 1 W/m^2. We make such a search by comparing cases e and f (Table 1). Cases e and f both include all four measured radiative forcings, with case f adding the effect of an initial disequilibrium +0.65 W/m^2. As discussed at the end of section 5, cases e and f use the same experiment runs, but they use, respectively, controls a' and a to subtract model drift.

6.7. Comparison of Radiative Forcings

Figure 4 compares the adjusted forcings due to stratospheric aerosol, ozone, greenhouse gas, and solar irradiance changes. The adjusted forcing is the net radiative flux change at the tropopause
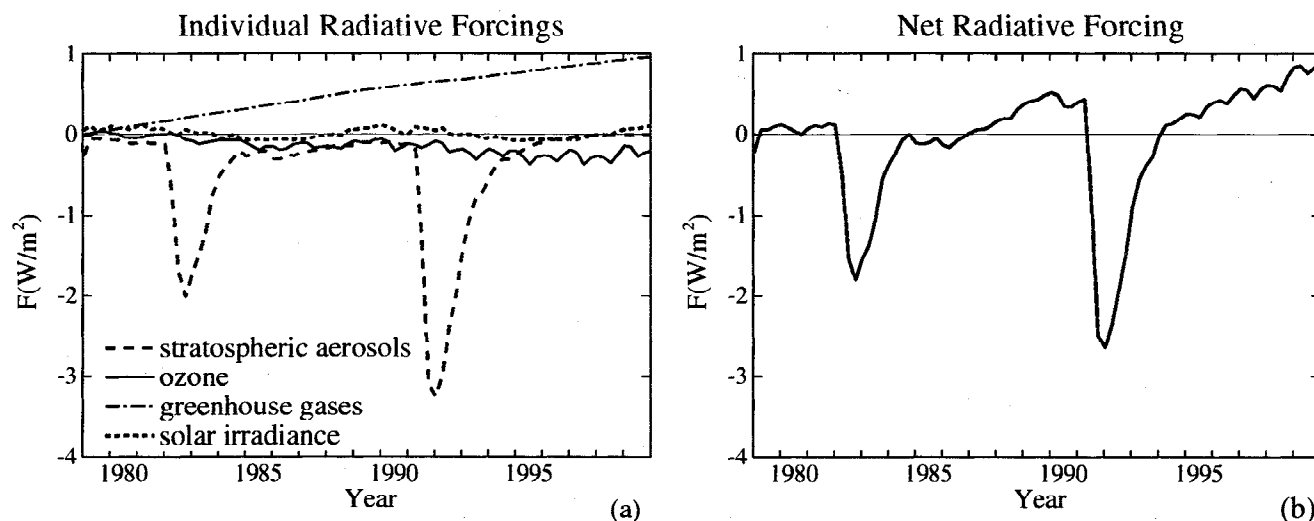

Figure 4. (a) Global-mean seasonal-mean adjusted radiative forcings due to the assumed changes of stratospheric aerosols, ozone, well-mixed greenhouse gases, and solar irradiance; and (b) net forcing due to these four mechanisms. This estimate of adjusted forcing is obtained by calculating the instantaneous forcing for each constituent for the full period and multiplying by the ratio of adjusted forcing to instantaneous forcing calculated for single years (1992 for stratospheric aerosols, 1994 for ozone and the well-mixed greenhouse gases, and the difference between 1981 and 1985 for solar irradiance).

after the stratospheric temperature has equilibrated with the changed radiation field. In most cases the adjusted forcing is a better measure of the expected climate response than is the instantaneous forcing [*Hansen et al.*, 1997b]; but because the instantaneous forcing is easier to calculate, we obtained the adjusted forcings for the time-varying forcings by calculating the instantaneous forcing for every season from 1979 to 1999 and multiplying it by the ratio of adjusted and instantaneous forcings calculated for specific changes of the different constituents. This ratio was found to be 0.94, 2.8, 0.88, 1.06, and 1.02 for stratospheric aerosol, ozone, carbon dioxide, other well-mixed greenhouse gases, and solar irradiance changes, respectively. These values and their bases are discussed by *Hansen et al.* [1997b]. Note that any error due to computing adjusted forcings at only one time has no effect on the climate simulations in this paper, as the GCM transient simulations employ directly the time-dependent changes of the radiative constituents, not the estimated forcing in Figure 4.

Stratospheric aerosols cause the largest short-term climate forcing. The well-mixed greenhouse gases are the dominant long-term factor. However, ozone depletion causes a significant negative forcing since 1979. Solar forcing is small, its full annual-mean solar-cycle amplitude being about 0.15 W/m^2. This small value occurs because the smoothed amplitude of total solar irradiance variability is only about 0.08% [*Willson and Hudson*, 1991; *Lean*, 1991] and because the variability is largest at ultraviolet wavelengths where the radiation does not reach the troposphere; these effects are discussed quantitatively by *Hansen et al.* [1997b]. The solar cycle irradiance variation also affects ozone amount, causing an indirect forcing of about 0.05 W/m^2 which is in phase with the direct solar forcing, yielding a net solar forcing of about 0.2 W/m^2 [*Hansen et al.*, 1997b]. The convention in this paper is to include the solar-induced ozone change in the ozone climate forcing, not in the solar forcing.

The net climate forcing, due to the four measured radiative constituents, approaches 0.5 W/m^2 in the mid-1990s, relative to 1979. This is considerably less than the forcing by the well-mixed greenhouse gases alone, mainly because of the negative forcing due to ozone change. The negative forcing due to ozone depletion in the lower stratosphere easily outweighs the positive forcing due to tropospheric ozone increase in the period 1979-1995 [*Hansen et al.*, 1997b], unlike the situation during the preceding century [*Hauglustaine et al.*, 1994; *IPCC*, 1995; *Hansen et al.*, 1997a].

The forcing due to the measured radiative changes should be contrasted with the 1%/y CO_2 growth rate that is sometimes used in idealized scenarios as a case with presumed relevance to anthropogenic greenhouse gas changes. The 1%/y scenario, beginning with 1.4 ppm/y CO_2 growth rate in 1979, yields a forcing at the end of 17 years of 1.3 W/m^2, more than twice the net forcing due to the four measured radiative mechanisms. Indeed, because of the two large volcanos in the period 1979-1996, it appears that the four measured forcings should produce very little net global temperature change as a result of their changes within that period. This is confirmed by calculations in section 7.

7. Global Mean Climate Response

Global mean quantities provide a good opportunity to detect a response to small radiative forcings because unforced variability or "noise" is least on the largest spatial scales. Here we compare the global thermal response in the climate model with satellite measurements of stratospheric (MSU4) and tropospheric (MSU2) temperature [*Spencer et al.*, 1991], and with combined land-ocean surface temperature data of *Hansen et al.* [1996b].

7.1. Ocean A: Observed SSTs

Calculated global-mean annual-mean atmospheric temperatures for ocean case A, i.e., specified observed transient SSTs for 1979-1995, are shown in Figure 5a. The five rows correspond to the different forcings of Table 1, ranging from no radiative forcing in the top row to all four forcings (stratospheric aerosols, ozone, well-mixed greenhouse gases, and solar irradiance) in the bottom row. For each forcing there is an ensemble of five runs, which differ only in their slightly altered initial atmospheric conditions.

Temperature anomalies are defined as the deviation from the 1979 to 1990 mean, except for MSU channel 4 where we follow the convention of Christy [J. R. Christy, Analysis of the merging procedure for the MSU daily temperature time series, submitted to *Journal of Climate*, 1997], defining anomalies relative to the 1984-1990 mean. The period between volcanos is used as a base to prevent biasing of the mean seasonal cycle by the El Chichon and Pinatubo volcanic perturbations, which have a large effect on stratospheric temperature.

7.1.1. MSU channel 4.
Observed time-varying SSTs alone affect the MSU channel 4 level by only about 0.1°C (Figure 5a, top left corner). Even these small variations are in part SST influence on the troposphere, as 5.5% of the channel 4 signal arises [*Hansen et al.*, 1996a, Table 1] from GCM layers 1-7 (beneath 150 mbar level) and 36% from GCM layer 8 (70-150 mbar) which straddles the tropopause at low latitudes. Furthermore, as discussed above, the present model is not expected to be a reliable tool for studying dynamical interactions of the troposphere and stratosphere, so we do not pursue the significance of these small modeled temperature variations in channel 4.

The present model represents well radiative forcings by aerosols and gases and thus should simulate their direct thermal response. Although dynamical feedbacks that alter the spatial distribution of temperature change may not be simulated accurately, such effects are probably smallest for the global mean. Figures 5b, 5c, and 5d suggest that the long-term global-mean cooling trend in the stratosphere is accounted for reasonably well by the combination of ozone depletion, and to a lesser extent increasing CO_2, while volcanic aerosols must be the cause of the stratospheric warmings of 1982-1983 (following El Chichon) and 1992-1993 (following Pinatubo).

Observed stratospheric cooling between 1979 and 1996 is about 0.9°C. The calculated cooling due to ozone change is about 0.6°C, and CO_2 change increases the calculated cooling to about 0.7°C. The remaining discrepancy with observations perhaps is not meaningful in view of uncertainties in the ozone change and the coarse vertical resolution of our model; but longitudinal variation of ozone change, which we do not include in our ozone forcing, is substantial [*Hood and Zaff*, 1995]; associated changes in stratospheric dynamical patterns could alter zonal mean and perhaps even global mean temperatures. In addition, if stratospheric water vapor is increasing, as limited measurements suggest [*Oltmans and Hofmann*, 1995], that would increase stratospheric cooling.

The calculated stratospheric warming after the volcanos is less than that observed, especially after El Chichon. The simulated warming would be greater if the aerosol size distribution had more large particles than the gamma function size distribution that we employed [*Hansen et al.*, 1996a]. Our Pinatubo aerosol size distribution is derived from SAGE measurements at four wavelengths in the range 0.4-1 μm, assuming a fixed shape (gamma function) for the size distribution with a time-independent effective variance of 0.35 μm. Our El Chichon aerosol size distribution is based on in situ measurements analyzed by J. Pollack and colleagues
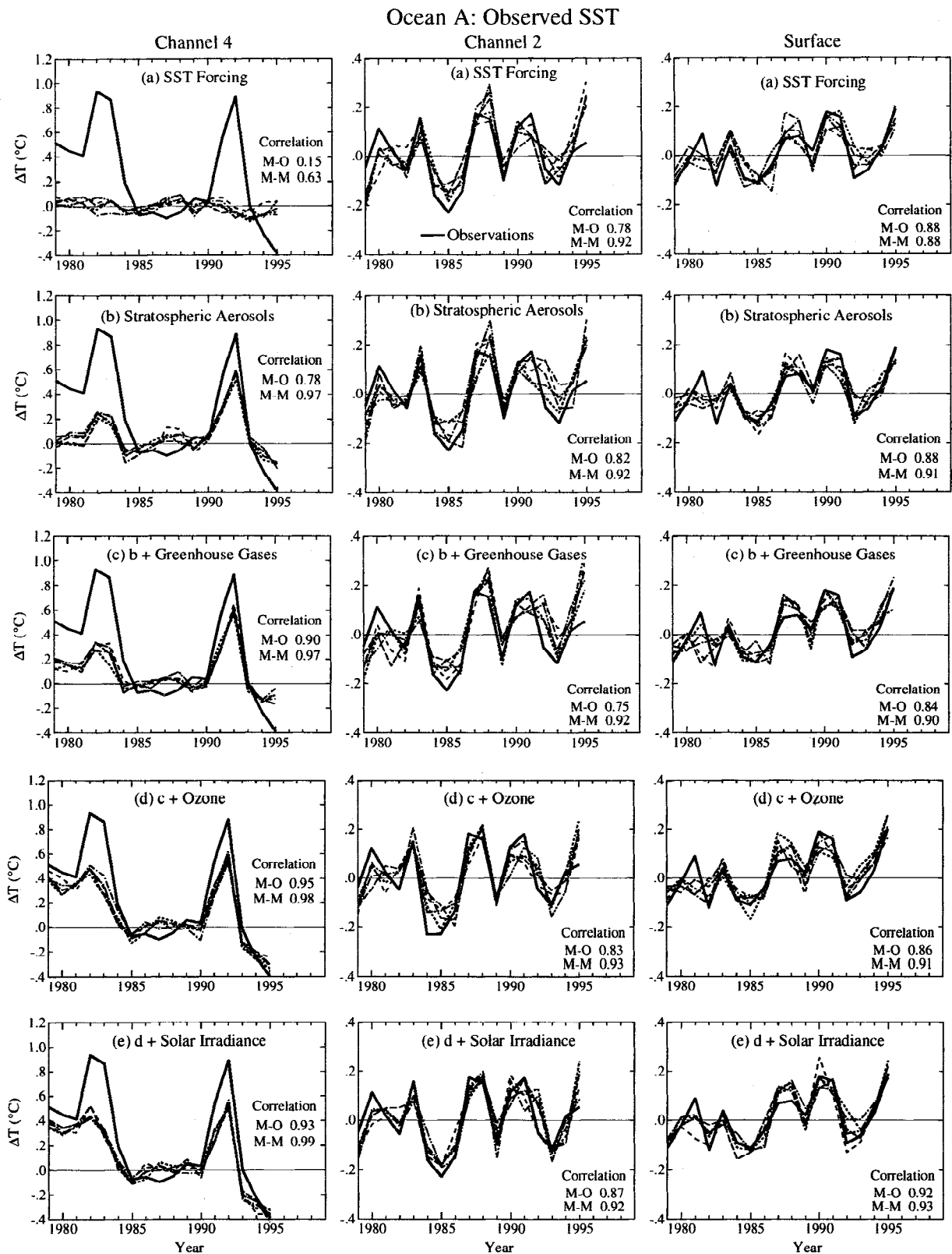
Figure 5a. Comparison of observed global stratospheric, tropospheric, and surface annual-mean temperatures (solid lines) with model calculations (five runs) in which the SST is specified from observations. The base period is 1984-1990 for Microwave Sounding Unit (MSU) channel 4 and 1979-1990 for MSU channel 2 and surface temperature. The model-observation (M-O) correlation coefficient is between the observations and the mean of the model curves. The model-model (M-M) correlation coefficient is the mean of the correlations of the individual model curves with the mean of the other model curves. MSU observations are from *Christy et al.* [1997] and surface data are from *Hansen et al.* [1996b].

at Ames Research Center. For both volcanos there are satellite measurements at thermal infrared wavelengths available, from the solar mesosphere explorer for El Chichon [*Eparvier et al.*, 1994] and from the Upper Atmospheric Research Satellite [*Lambert et al.*, 1993] for Pinatubo. These thermal infrared data, in combination with the other aerosol data we have used, should allow derivation of a more detailed and reliable aerosol size distribution for use in future climate simulations.

Underestimate of short-term volcanic-induced stratospheric warming may be due in part to the assumption of a pure sulfuric acid aerosol composition, as volcanic ash or impurities could increase absorption of solar radiation. However, this is probably not the major reason, because ash particles tend to be large and fall out more rapidly, while the observed excess warming is still present in the second year after the eruption. Another possibility is that the simulations in our present nine-layer model are unable to accurately portray the aerosols' thermal effect because of the model's poor vertical resolution. *Young et al.* [1994] found greater heating by the Pinatubo aerosols in their 26-layer stratospheric model, but it is not clear whether the greater heating resulted from the higher vertical resolution, their assumed crude aerosol size distribution (mean radius 0.6 μm), or dynamical effects.

Finally, we note that the uncertainty about volcanic-induced stratospheric warming has only little effect on the stratospheric aerosol radiative forcing of the troposphere, which is a function primarily of the aerosol optical depth for solar radiation [*Lacis et al.*, 1992; *Hansen et al.*, 1996a, 1997b]. We estimate the uncertainty of the volcanic aerosol forcing of the troposphere as at most 20% for both El Chichon and Pinatubo.

7.1.2. MSU channel 2 and surface air. Observed and simulated interannual temperature variations are larger in the troposphere than at the surface (Figure 5a, columns 2 and 3). Enhanced sensitivity in the middle troposphere occurs in global warming calculations [e.g., *Manabe and Wetherald*, 1980; *Hansen et al.*, 1984] as a result of increased surface evaporation and subsequent latent heat release in the troposphere. Enhanced tropospheric variations are also observed in radiosonde temperature profiles, especially in relation to the tropical El Niño cycle [*Angell and Korshover*, 1977].

The year-to-year global mean temperature variations driven by specified SSTs (Figure 5a) are in good agreement with observations, a result previously obtained with other climate models by *Graham* [1995] and *Kumar et al.* [1994] in simulations with observed SSTs but no explicit radiative forcings. Of course, the specified SSTs implicitly contain much of the influence of any radiative forcings, and use of observed SSTs should yield a high correlation with observations, at least over the oceans.

We provide in Figure 5a the model-observation correlation between the observed global temperature curve and the mean of the five simulations. In addition, we include a model-model correlation, specifically the mean of the correlations calculated for each of the individual runs against the mean curve for the other four runs.

The correlation of model and observations must be less than unity. Even if the model and observations were both perfect, the observed temperature curve would not fall entirely within the envelope specified by only five model runs. Because the real world runs through this experiment period only once, at best the model-observation correlation will only approximate the model-model correlation.

The model-observation correlations are about 0.9 for both the troposphere and the surface when all forcings are included. The model-observation correlations have a significance above 99% in all cases except channel 4 (stratosphere) with only SST forcing. Remarkably, the model-observation correlation is almost as high as

the model-model correlation. The fact that the model is driven by observed SSTs limits the practical significance of the high correlation, but it suggests that the model may be useful for analysis of observed climate change.

One question of interest is whether the direct effect of radiative forcings, other than the effect transmitted via changed SST, improves the agreement between observations and simulations. With ocean A the small radiative forcings, of the order of magnitude 1 W/m^2, are not allowed to affect SST and should have very little influence on surface air temperature over the ocean, but they may have some impact on continental and upper air temperature. There is a suggestion of an influence, as the model-observation correlations for tropospheric and surface air temperatures increase somewhat when all four radiative forcings are included. Whether the apparent changes are of physical significance can be addressed better by examining the spatial distribution of the changes (section 9).

7.2. Ocean B: Q flux Ocean

Figure 5b shows calculated global-mean atmospheric temperatures for ocean B, i.e., the Q flux ocean. The calculated stratospheric temperatures are essentially the same for ocean B as for ocean A. This is because of the dominance of local radiative changes in determining stratospheric temperature change.

The calculated tropospheric and surface temperatures have little net temperature change over 17 years when the model is driven by the four measured radiative forcings (case e). When the constant 0.65 W/m^2 forcing is added, a global warming trend slightly larger than observed is obtained. We defer discussion of whether we can meaningfully estimate an initial radiative disequilibrium until sections 7.4 and 10.1, when we can compare results for all ocean models.

The modeled temperature changes of the troposphere and surface for ocean B correlate less well with observations than in the case of specified SSTs, as expected. The mean model-observation correlation coefficient is much higher for surface air temperature (0.6-0.7 for all forcings) than it is for tropospheric temperature (0.1-0.2). Visual inspection indicates that the principal reason for the smaller correlation with MSU2 data is the observed global warming in 1983 and the cooling in 1989, these being global climate features associated with El Niño and La Niña, respectively. Of course, the climate model, even if it had a dynamically predicted ocean, could not predict the timing of El Niños and La Niñas based on initial conditions from several years earlier. Lack of El Niño/La Niña predictability affects the MSU2 level more than the surface air because El Niño/La Niña thermal anomalies are stronger in the middle troposphere than at the surface [*Angell and Korshover*, 1977]. This is because the surface El Niño southern oscillation (ENSO) signal occurs mainly in the equatorial east and central Pacific, while warming at the MSU2 level is spread throughout the tropics [*Yulaeva and Wallace*, 1994].

With all radiative forcings included, the correlations are significant at the 99% level for surface air but insignificant for MSU channel 2. The Pinatubo cooling is slightly (about 0.1°C) greater in the model than in the data. The model has a significant warming trend at the surface over the 17-year period but little trend in the troposphere. We make a quantitative comparison of surface-troposphere temperature differences in section 9.

7.3. Oceans C and D

The variability among experiment runs is larger for the dynamical ocean models (Figures 5c and 5d) than for the Q flux ocean (Figure 5b). This is consistent with the variabilities in the
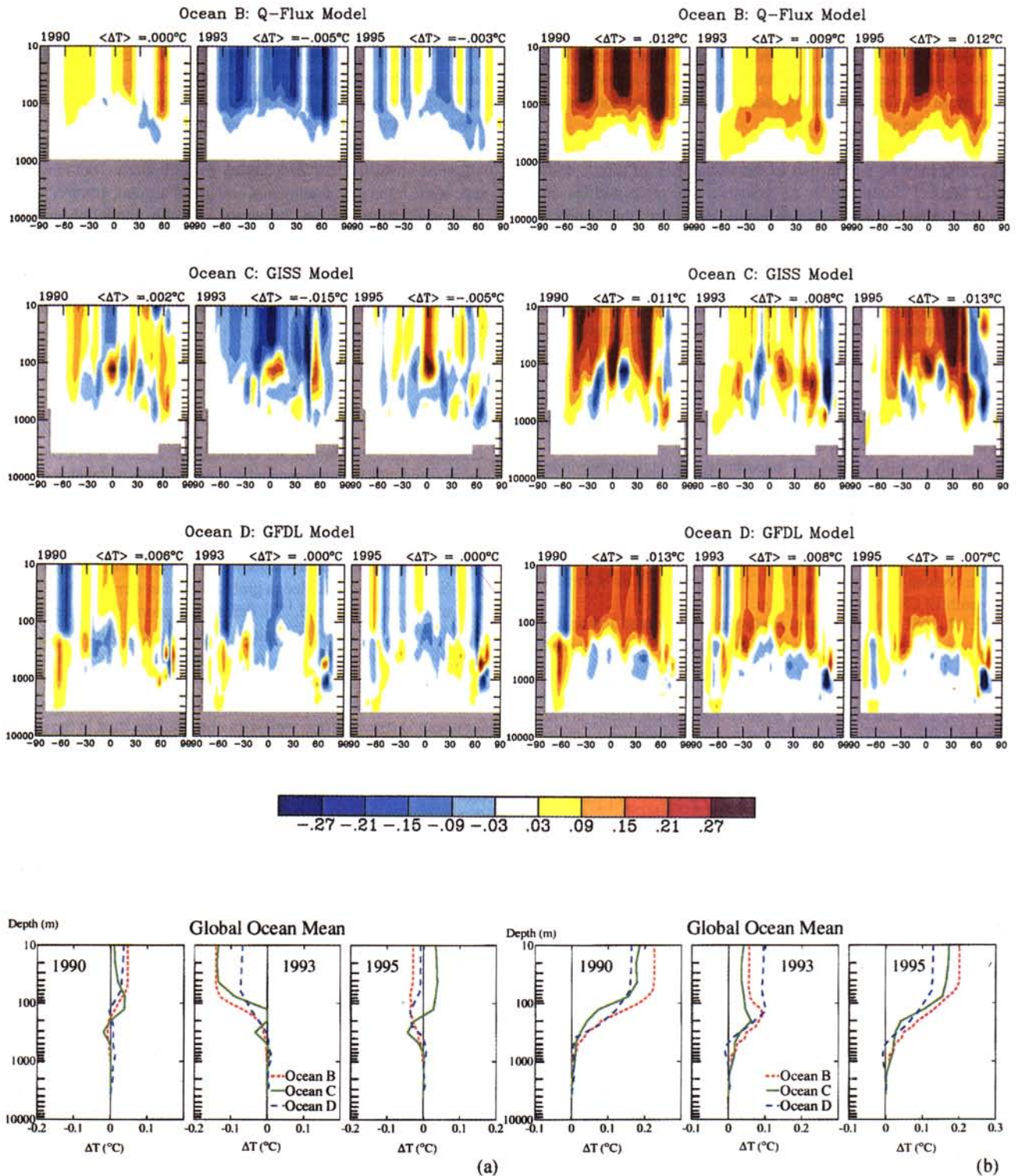
Plate 4. Temperature anomalies in oceans B, C, and D in 1990, 1993, and 1995. The anomalies are the difference between the mean of five model runs and five control runs from the same starting point. Temperature changes in the top right-hand corners are the mean over the actual (~4 km) ocean depth, with ocean B by assumption having zero change below 1000 m depth. (a) Results for the four measured radiative forcings and (b) Results including initial [1979] radiative disequilibrium of 0.65 W/m^2.
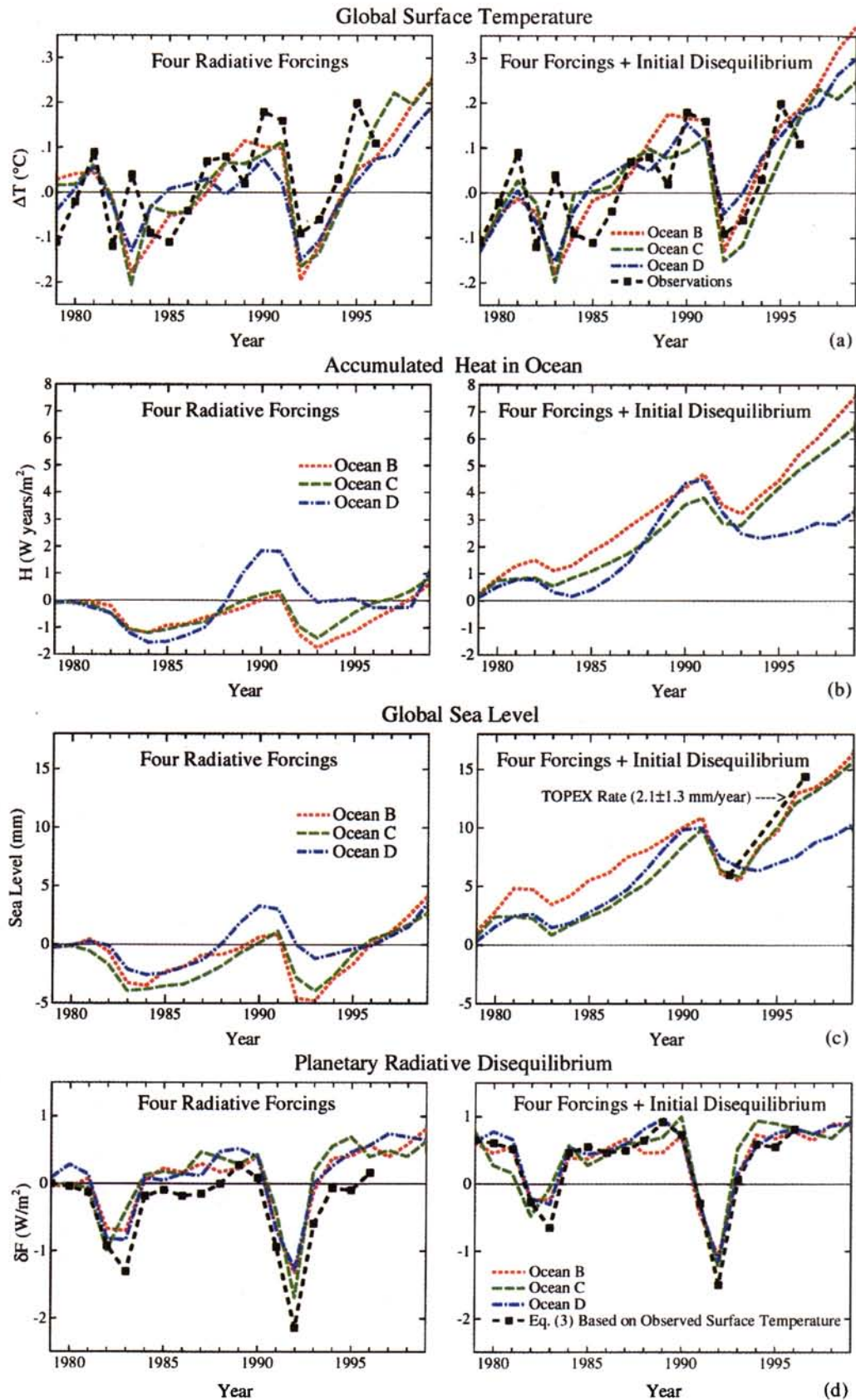
Plate 5. (a) Global surface temperature change for annual mean of five model runs with the four radiative forcings and the same four forcings plus an initial [1979] radiative disequilibrium of 0.65 W/m². Observations are from *Hansen et al.* [1996b]. Temperature zero point is 1979-1990 mean. (b) Ocean heat content relative to initial conditions in units of W yr/m² averaged over the full globe. (c) Mean sea level change due to thermal expansion of ocean water in the different models. (d) Planetary radiative disequilibrium at the top of the atmosphere (positive is heat gained by the planet).
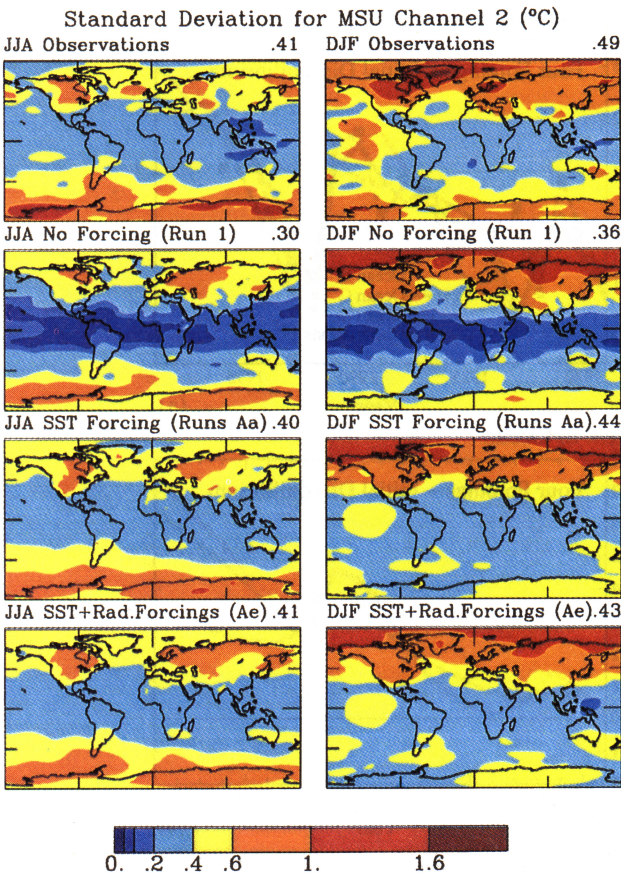
Standard Deviation for MSU Channel 2 (°C)

JJA Observations   .41   DJF Observations   .49

JJA No Forcing (Run 1)   .30   DJF No Forcing (Run 1)   .36

JJA SST Forcing (Runs Aa) .40   DJF SST Forcing (Runs Aa).44

JJA SST+Rad.Forcings (Ae) .41   DJF SST+Rad.Forcings (Ae).43

0. .2 .4 .6 1. 1.6

Plate 6. Standard deviation (σ) of seasonal-mean tropospheric temperature in observations (MSU2) and SI95 model. Run 1 has no forcing (climatological SST), run Aa observed time-varying SST, and run Ae observed SST plus four radiative forcings (table 1). Observed σ is based on 17 seasons, 1979-1996; σ of run 1 is based on a single run. σ of runs Aa or Ae is the mean for five 1979-1996 runs. The area-weighted global-mean σ is given in top right-hand corners.

control runs (Plate 1a). Also, the variability is larger for ocean C (GISS model) than for ocean D (GFDL model).

The response to the large volcanic aerosol forcings is also more variable with the dynamical ocean models, especially ocean C. Although the models do a good job of simulating the observed response to Pinatubo, their tight forcing-response determinism, especially that of the Q flux model, is not generally representative of the real world response to volcanos [Robock, 1991; Hansen et al., 1993, 1996a]. A case in point is the discrepancy between observed and simulated global temperatures after El Chichon, when a strong El Niño in 1983 more than compensated for volcanic cooling. Although the greater variability of the dynamical ocean models is per se more realistic than the Q flux model, it should not be assumed that the nature of this variability is the same as in the real world or that the present models provide reliable predictive capability for real world variability. For example, our simulation of the lower stratosphere is too poor to represent well the dynamical effects of aerosol heating proposed by Kodera and Yamazaki [1994], as discussed in section 3.11; also, our simulation of El Niño variations is too unrealistic for us to expect to represent volcano-El Niño interactions [Handler, 1986], should these exist in the real world.

The global mean temperatures simulated by our present models with dynamically interactive oceans do not represent the real world

more accurately than the Q flux model, judging only from the model-observation correlations in Figures 5b, 5c, and 5d. That is not a surprise, given the primitive state of the current ocean models and the fact that much of the global variability over a 17-year period may not be deterministic.

Finally, we note that the results with ocean models C and D, as well as A and B, present evidence for a cooling of the troposphere (as sampled by MSU channel 2) relative to the surface. This is qualitatively different than the result that would be expected for change of only CO_2 or other well-mixed greenhouse gases [Manabe and Wetherald, 1980; Hansen et al., 1984]. This topic, as well as the geographical distribution of the temperature change, is addressed quantitatively in section 9.

7.4. Intercomparison of Ocean Models

Global surface temperature has nearly zero trend for the 17-year period in oceans B, C, and D when the models are driven by the four measured forcings. With the addition of the initial radiative disequilibrium oceans B and D warm by 0.20°C over the 17-year period, while ocean C warms 0.09°C. These compare with the calculated warming of 0.17°C in model A (which uses observed SST) and observed warming of 0.16°C. The geographical patterns of the temperature changes in all four models and observations are presented in section 9.
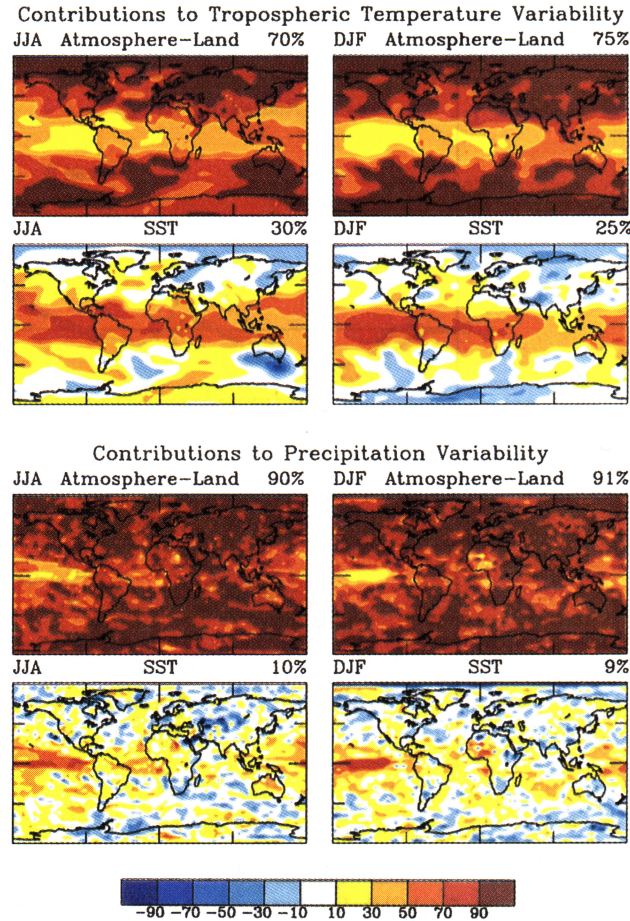
Contributions to Tropospheric Temperature Variability

JJA Atmosphere-Land   70%   DJF Atmosphere-Land   75%

JJA   SST   30%   DJF   SST   25%

Contributions to Precipitation Variability

JJA Atmosphere-Land   90%   DJF Atmosphere-Land   91%

JJA   SST   10%   DJF   SST   9%

-90 -70 -50 -30 -10 10 30 50 70 90

Plate 7. Portions of climate model variability attributable to unforced atmosphere-land variability and SST variability, for tropospheric temperature (top two rows) and precipitation (bottom two rows). For both parameters the top row is σ(run 1)/σ(run Aa), while the second row is [σ(run Aa)-σ(run 1)]/σ(run Aa).
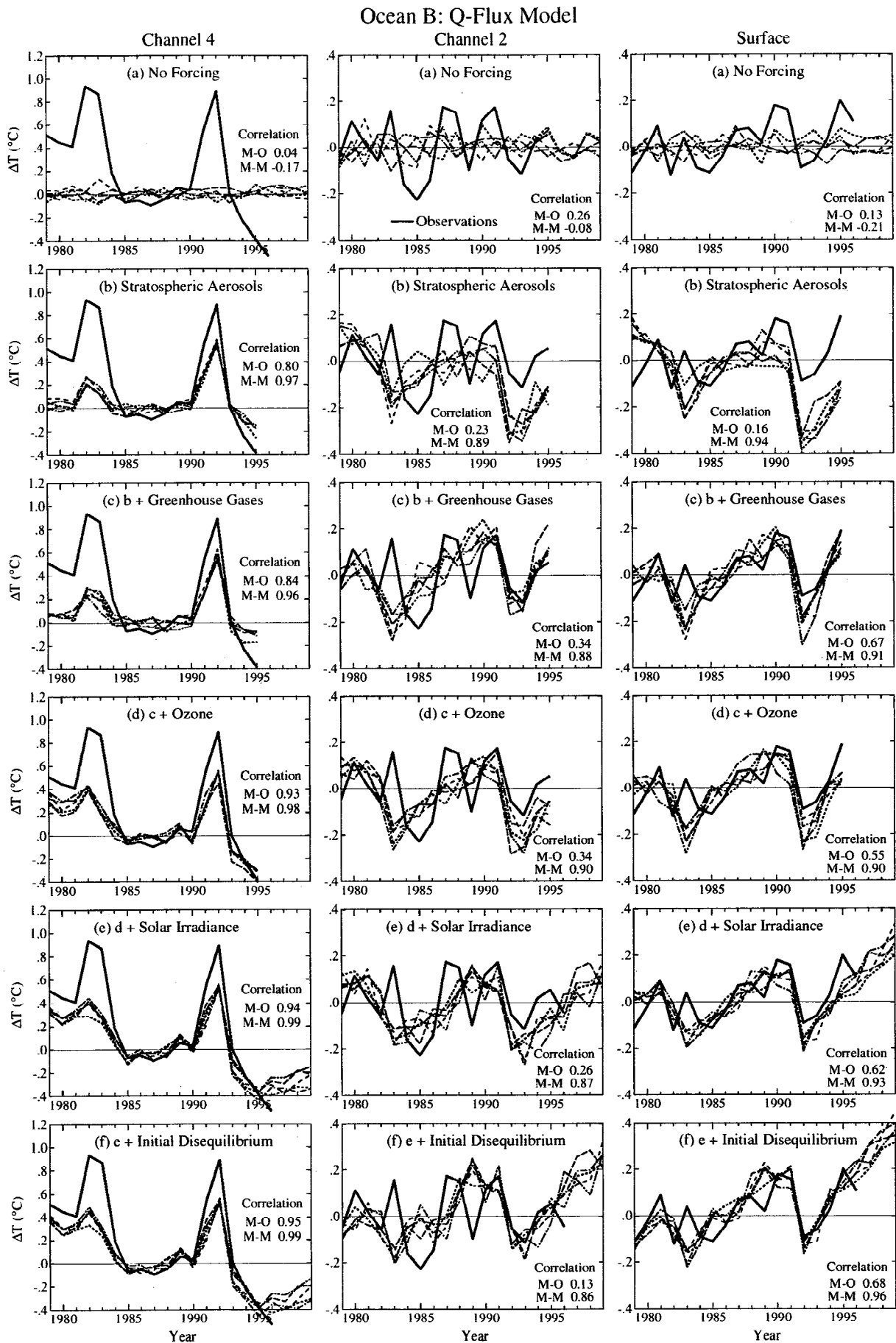
Ocean B: Q-Flux Model

Figure 5b. Comparison of observed global stratospheric, tropospheric, and surface temperatures (solid lines) with model calculations using the Q flux ocean. Definitions as in Figure 5a.
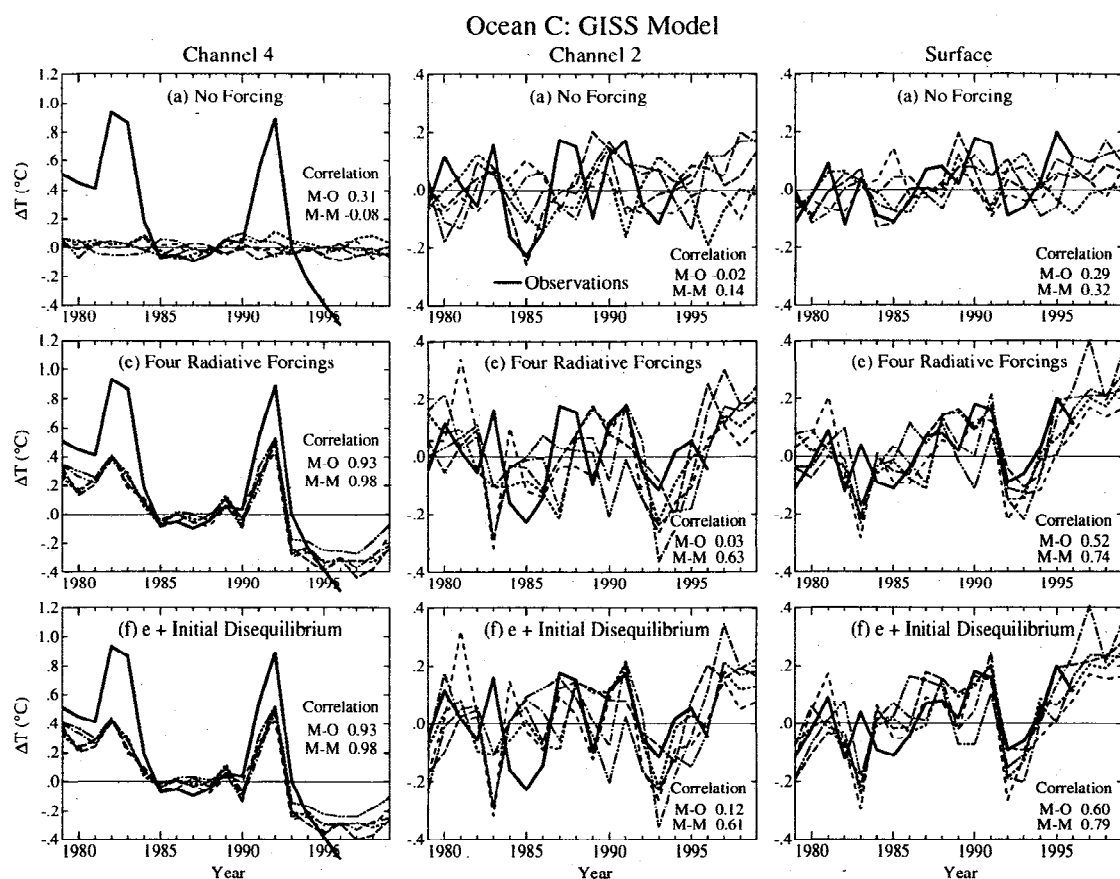
Ocean C: GISS Model

Figure 5c. Comparison of observed global stratospheric, tropospheric, and surface temperatures (solid lines) with model calculations using ocean C. Definitions as in Figure 5a.
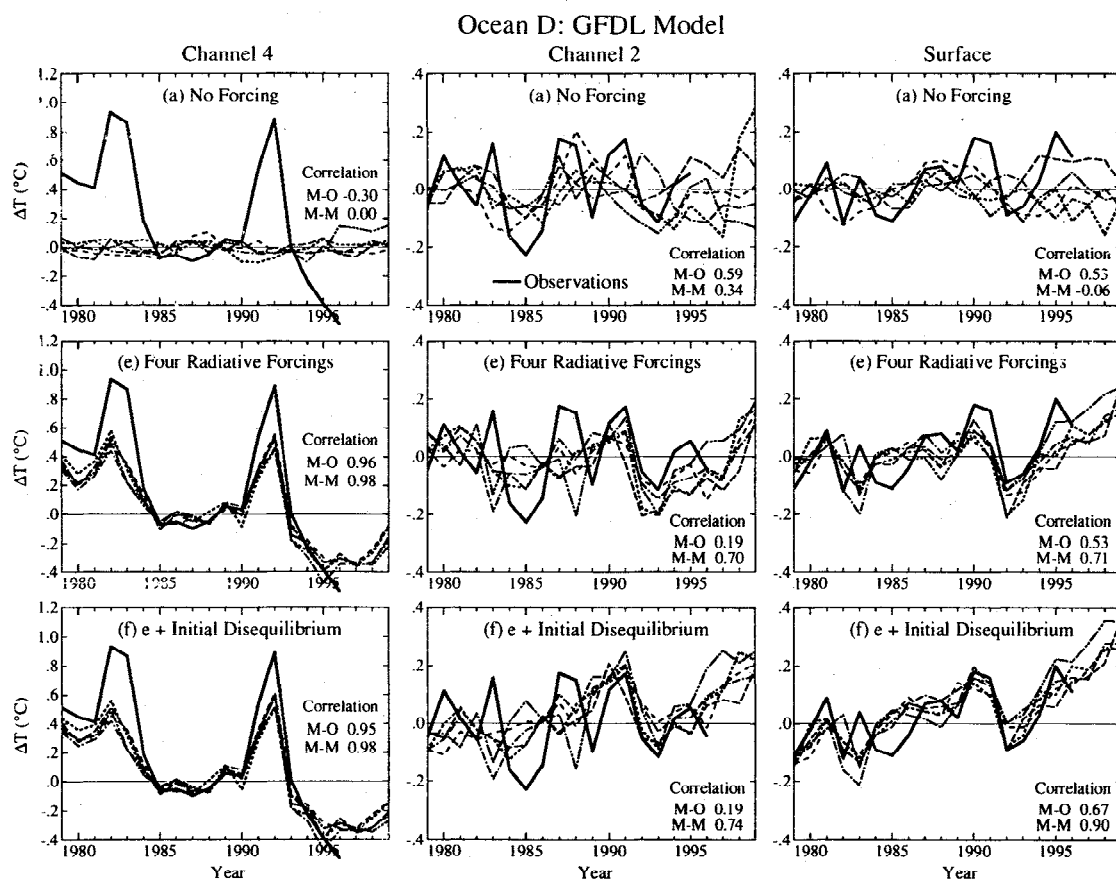
Ocean D: GFDL Model

Figure 5d. Same as Figure 5c but for ocean D.

Calculated heat anomalies in the ocean are shown in Plate 4a for 1990 (last year before Pinatubo), 1993 (just after maximum Pinatubo impact), and 1995 (when observed surface temperature seems to have recovered from Pinatubo cooling) for the case with the models driven by the four measured radiative forcings. Results with the initial radiative disequilibrium included are shown in Plate 4b. Although there are differences among the three ocean models, the initial radiative disequilibrium overwhelms these differences, causing a substantial ocean heat storage in all cases. As shown below, the heat storage amounts to several W yr/m^2 averaged over the world.

Detailed study of the ocean temperature anomaly patterns is probably unwarranted, because the versions of oceans C and D that we employed were primitive. We note that the great depth of penetration of temperature anomalies at high southern latitudes in ocean D was previously found by *Manabe et al.* [1990].

The global mean surface temperature change, averaged over the five runs of each model, is compared with observations in Plate 5a, and the cumulative heat storage in the ocean is shown in Plate 5b. The cumulative heat storage is only 3-4 W yr/m^2 by 1995, despite the initial radiative disequilibrium of 0.65 W/m^2 and continued growth of greenhouse gases. This is mainly because of the cooling effect of the two large volcanos.

The sea level change caused by thermal expansion or contraction of ocean water in the different models is shown in Plate 5c and compared with the rate of sea level change inferred from satellite (TOPEX/POSEIDEN) surface topography measurements in the last 4 years [*Nerem et al.*, 1997]. Interpretation of observed sea level change is hindered by the absence of measurements of ice sheet volume changes, but it appears that thermal expansion could account for much of the observed sea level change in the past several years.

The planetary radiative disequilibrium (imbalance) at the top of the atmosphere, $\delta F(t)$, is shown in Plate 5d for the mean of 5 runs for each of oceans B, C, and D. For comparison, we show the disequilibrium estimated from

$$\delta F(t) = c \, [T_{eq}(t) - T(t)], \tag{3}$$

where the proportionality constant to convert a forcing to an equilibrium temperature change is taken to be $c = 4.2$ W/m^2/3.6°C, based on our doubled CO_2 experiment, $T(t)$ is the observed global temperature of *Hansen et al.* [1996b], and $T_{eq}(t)$ is the equilibrium surface temperature for the forcings known to exist at time t, i.e., c $T_{eq}(t)$ is the forcing due to the four measured radiative forcings shown in Figure 4.

The left side of Plate 5d shows that a wide disparity (about 0.5 W/m^2 by 1995) develops between the disequilibrium based on models with free ocean temperatures and the result based on observed temperatures, if the constant disequilibrium forcing is not included. This is a consequence of the unrealistic temperature changes in all the models if no initial disequilibrium is included. Removal of this disparity requires an initial disequilibrium of at least 0.5 W/m^2.

The calculated disequilibrium in the late 1990s is in the range 0.7-1 W/m^2 for the different ocean models. This result is based on the assumption of no large volcanic eruption in the remainder of the decade.

8. Regional Climate Variability and Predictability

Our experiment ensembles provide a tool for comparing unforced climate fluctuations (chaos) with forced (deterministic)

climate changes. Indeed, the brevity of the period studied, 1979-1996, suggests that chaos may be the dominant factor in regional climate variations. Thus we study the unforced variability before examining regional model results for signatures of climate forcings.

Other investigators have examined ensembles of model runs to study regional climate variability [*Barnett*, 1995; *Bengtsson et al.*, 1995; *Harzallah and Sadournny*, 1995; *Stern and Miyakoda*, 1995; *Kumar et al.*, 1996; *Brankovic and Palmer*, 1997], and informative studies of the role of unforced variability have been made with simple atmospheric models [*Lorenz*, 1984; *Pielke and Zeng*, 1994; *Kurgansky et al.*, 1996]. Our study differs from these in that we examine the effect of several global radiative forcings and the influence of several alternative ways of modeling the ocean. *Manabe and Stouffer* [1996] have previously studied the variability in long control runs with several ways of treating the ocean.

The climate parameters we illustrate are tropospheric temperature, surface temperature, and precipitation. We focus on tropospheric temperature measured by MSU channel 2 (hereinafter MSU2) because of its global coverage and high precision. We choose MSU2 over MSU2R because MSU2R, as the difference of measurements at different angles, is noisier and more subject to contamination by hydrometeor effects and surface emissivity changes [*Hansen et al.*, 1995a; *Prabhakara*, 1995].

In section 8.1 we examine the magnitude of interannual climate variability, comparing models to observations and one model with another. Because the models do a reasonable job of simulating observed interannual climate variability, we can use them to estimate the contributions to observed climate variability arising from radiative forcings and from unforced variability in different parts of the climate system.

In section 8.2 we examine potential climate predictability. We estimate an upper limit on predictability by examining the correlation among model runs with identical forcings. We then obtain a perhaps more realistic estimate of potential predictability of short-range climate by comparing observed climate change with ensemble mean model simulations.

In our nomenclature, chaos is synonymous with unforced variability. When we carry out simulations with some parts of the climate system fixed at climatological values, we identify the parts of the climate system contributing to the resultant chaotic variability. Specifically, in our simulations using climatological SSTs, the variability of climate parameters is described as the atmosphere-land contribution to the model's total variability. Soil moisture anomalies, for example, provide a means by which the influence of short-term atmospheric fluctuations is extended over longer timescales. Our aim here is to divide the variability into a small number of categories for an initial survey.

8.1. Climate Variability

We examine climate variability in four steps. First, we show examples of the standard deviation of climate parameters over the period 1979-1996 in our model runs and observations; the standard deviation is a limited measure of variability, excluding information on space-time correlations, but it provides an intuitive compact measure of regional variability. Second, we show examples of the atmosphere-land contribution to chaotic variability (based on an ensemble of simulations with climatological SST) and the SST thermal forcing contribution (based on simulations with observed time-varying SST); in these simulations the chief effect of atmospheric radiative forcings is implicitly lumped into the specified ocean temperature variations. Third, we compare the

unforced variabilities obtained with our four different ocean representations. Fourth, we use the three models with calculated SSTs to estimate the explicit contribution of atmospheric radiative forcings to climate variability in the period 1979-1996.

8.1.1. Standard deviations. The observed interannual variability of seasonal mean tropospheric temperature is shown in the top row of Plate 6. The next row is the interannual variability in the GCM when the SST has fixed climatological values, that is, when there is no climate forcing; in this case, only the atmosphere and land contribute to interannual variability. The third row is the interannual variability in the model when the SST has its observed interannual variations. The bottom row is the model variability when it is forced by both observed SSTs and the four radiative forcings incorporated in runs Ae.

Plate 6 indicates that the model realistically reproduces observed tropospheric temperature variability when forced by observed SSTs. The results also show that a large fraction of the observed variability at middle and high latitudes is inherent in unforced atmospheric variability, while at low latitudes observed SSTs account for much of the atmospheric variability. Explicit addition of radiative forcings, with SSTs specified, makes no significant change in the variability, but of course, the radiative forcings played a role in establishing the SST variations. Below we estimate the proportion of variability associated with radiative forcings by using the models with calculated SST.

8.1.2. Contributions to chaos. The atmosphere-land and SST contributions to interannual variability are illustrated in Plate 7, based on simulations with climatological SSTs and observed time-varying SSTs. Averaged over the world, for the period 1979-1996, about 70-75% of the tropospheric temperature variability is unforced atmosphere-land variability. This large chaotic variability must severely limit climate predictability at middle and high latitudes, especially in the winter. The situation is much more favorable at low latitudes, where typically 50 to 75% of the variability is associated with SST variations. Thus on the timescales and to the degree that low-latitude SSTs are predictable, there is the potential for substantial predictability of low-latitude temperatures, a conclusion reached by many others [e.g., *Charney and Shukla*, 1981; *Barnett*, 1995; *Bengtsson et al.*, 1995; *Harzallah and Sadourny*, 1995; *Stern and Miyakoda*, 1995; *Brankovic and Palmer*, 1997].

Radiative forcings have negligible impact on variability if SSTs are specified, as shown by the bottom row of Plate 6; but part of the 25-30% of global variability associated with SST variations must be due to radiative forcings which have influenced the SSTs. Also, on longer timescales, some of the variability in the atmosphere-land portion may be driven by radiative forcings, for example, by soil moisture anomalies and vegetation distributions which are modified by greenhouse gases and other radiative forcings on century and paleoclimate timescales.

The estimated partitioning of variability into atmosphere-land (70-75%) and SST (25-30%) categories applies to this particular climate parameter (tropospheric temperature) and period (1979-1996). We find a similar partitioning for surface air temperature (not illustrated), but only about 10% of the interannual variability of precipitation is forced by SST variations (Plate 7). The accuracy of these values is limited by the reliability of the present climate model, so they are only current estimates which should be compared with results from successively more realistic models.

8.1.3. Ocean representations. Plate 8 shows the standard deviation of surface air temperature in the control runs for all four oceans, each coupled with the SI95 atmospheric model, and compares these with the standard deviation of observed

(1979-1996) surface temperature [*Hansen et al.*, 1996b]. The surface air temperature variability with observed SSTs (ocean A) is a good approximation to observed variability, except that the model generates excessive variability over land areas, especially in the summer.

The Q flux model (ocean B) generates a realistic level of interannual variability in the midlatitude storm track regions, similar to that obtained by using observed SSTs, signifying that this variability is driven by the atmosphere. At low latitudes, on the other hand, the Q flux model entirely misses ENSO variability.

Both the GISS (ocean C) and the GFDL (ocean D) models generate ENSO-like SST variability in the tropical Pacific, and in both cases the most pronounced interannual variability is located in the central Pacific, while observed SSTs have greatest variability near South America. The standard deviation in our version of the GFDL model has a maximum value of only about 0.3°C in the region of ENSO-like variability; in part, this is because in the present simulations the surface heating anomalies were distributed through the upper three layers of the ocean. In a separate run of this ocean model, with surface heating anomalies inserted into the upper ocean layer, the standard deviation in this region is about twice as large, similar to values found by *Knutson and Manabe* [1994] using the GFDL model at a similar resolution. *Philander et al.* [1992] show that the amplitude of the ENSO-like variability increases further, to realistic values, and its location becomes more realistic, when higher resolution is employed in the tropical Pacific Ocean.

In the GISS ocean model the magnitude of the ENSO-like variability is surprisingly large, given the 4° by 5° ocean resolution, even somewhat larger than observed. Although this may partly result from the differencing scheme, which effectively increases the resolution, it also is probably due to the fact that surface fluxes are inserted only into the upper ocean layer, which is thin (12 m). This apparent sensitivity of the surface variability in both oceans C and D emphasizes the need to include realistic ocean mixed layer modeling based on first principles, which mixes the surface fluxes to appropriate depths on appropriate timescales.

8.1.4. Radiative contribution to variability. We want to estimate the portion of the climate variability that is driven by deterministic global radiative forcings. This requires simulations in which the ocean temperature is allowed to respond to the radiative forcings. Thus we examine results of experiments with oceans B, C, and D.

Plate 9 shows the calculated percentage of seasonal-mean tropospheric temperature variability (for the period 1979-1995) that is associated with the four modeled radiative forcings. Because this proportion of variability associated with the radiative forcings is small, it is difficult to define with five runs. Thus we also examined several other cases, for example using control runs *a* rather than *a'* and using five 17-year periods from the 100-year control run, rather than five separate runs. In all cases the global mean of the proportion of local interannual variability associated with the radiative forcings was in the range -1 to 12%, typically 5-8%.

Inferences from these model runs are constrained by the degree of realism of the model. We may underestimate the radiative impact as a result of the inability of our present model to represent certain climate change mechanisms, for example the effect of stratospheric radiative changes on stratosphere-troposphere dynamical interactions or radiative influences on the Southern Oscillation. The fact that our simulated variability of tropospheric temperature is somewhat smaller than observed variability (Plate 5) suggests that there is still room for some mechanisms of climate variability, which are not being captured by our present model, but not a great deal of room.

These results imply that only a minor portion of regional interannual climate variability in this 17-year period is accounted for by radiative forcings. Given the small magnitude of this radiatively forced variability, the number of our experiment runs is too few to determine its spatial distribution, although clearly, it is larger (on a percentage basis) in the tropics than at high latitudes. The small contribution of radiative forcings to regional variability, summarized by the global mean of the regional values on the upper right corner of each map (Plate 9), does not imply that radiative forcings do not strongly drive global mean climate parameters, as suggested by Figure 5.

We conclude that most of the interannual variability of seasonal mean regional climate parameters on the 17-year timescale is the unforced (chaotic) atmosphere-land contribution. Most of the remaining variability is associated with SST changes. The SST changes themselves may be largely chaotic on long timescales, but the ocean's inertia means that the ocean fluctuations are persistent or modelable, and thus deterministic, to a degree that probably decreases rapidly on timescales from seasons, to years, to decades. Although the regional radiatively forced variability is small on the
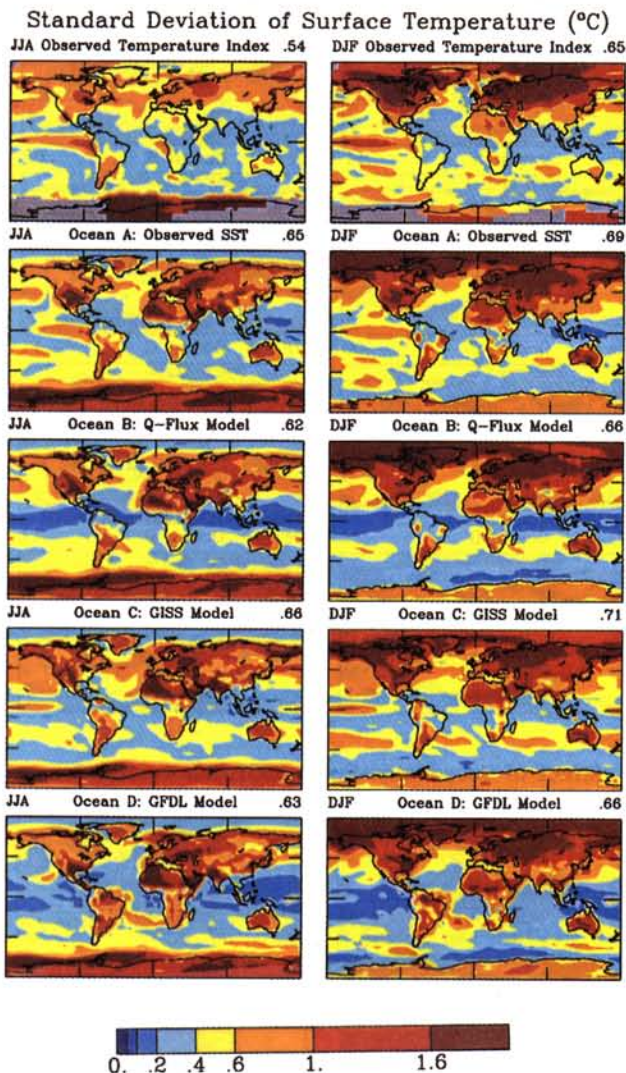
Radiative Contributions to Variability

Standard Deviation of Surface Temperature (°C)
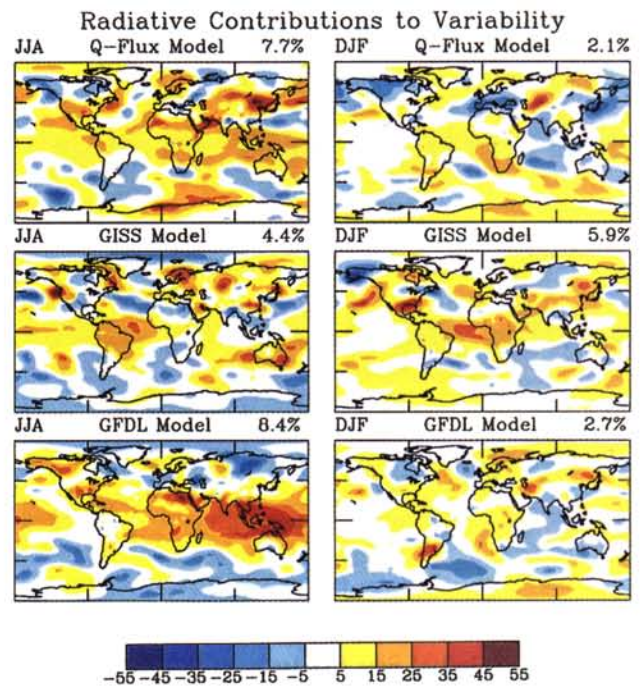
Plate 9. Contributions of radiative forcings to tropospheric (MSU2) temperature variability as estimated from three different ocean models. In each case, the quantity shown is $[\sigma(\text{run f})-\sigma(\text{run a'})]/\sigma(\text{observations})$. Model σ is calculated for each 17-year run and averaged over five runs; observations are based on a single 17-year period (1979-1996).

17-year timescale, it can be presumed to increase on longer timescales for forcings which grow with time, such as anthropogenic greenhouse gases.

8.2. Climate Predictability

Lorenz [1982] studied potential predictability of weather by examining ensembles of GCM forecasts. He estimated an upper limit to predictability based on the variation among ensemble members, and he set a lower limit based on the skill of an ensemble mean forecast using a state-of-the-art model. Here we study seasonal climate simulations with an analogous approach, although we do not attempt to optimize our model for seasonal forecasts by using observed initial atmospheric conditions. Our purpose is not to produce seasonal predictions but rather to gain some understanding of inherent limitations on determinism.

8.2.1. Potential predictability. The spread among an ensemble of runs arises from the chaos inherent in the solutions of the nonlinear equations describing the climate system [*Lorenz*, 1963]. The ensemble mean provides the best forecast. However, even if the model were a perfect representation of the real world, the mean accuracy of the ensemble mean forecast is only that represented by the correlation between the ensemble mean and the individual climate realizations, because the real world runs through the "experiment" only one time. Thus we obtain our upper limit on predictability, Plate 10, by taking the mean of the correlations of each individual ensemble member with the ensemble mean, with the ensemble mean excluding the individual member to avoid autocorrelation. Specifically, at each grid point we calculate the means of the correlations of each 17-year time series with the mean 17-year time series of all other ensemble members.

The upper limits on predictability that we obtain for tropospheric temperature, surface air temperature, and precipitation are shown in

Plate 8. Standard deviation of seasonal mean surface temperature. Observations [*Hansen et al.*, 1996b] are surface air temperature over land and SST over ocean. Model results are the mean standard deviation of surface air temperature in five 17-year runs of the SI95 atmospheric model attached to four different oceans (control runs Aa, Ba, Ca, and Da).
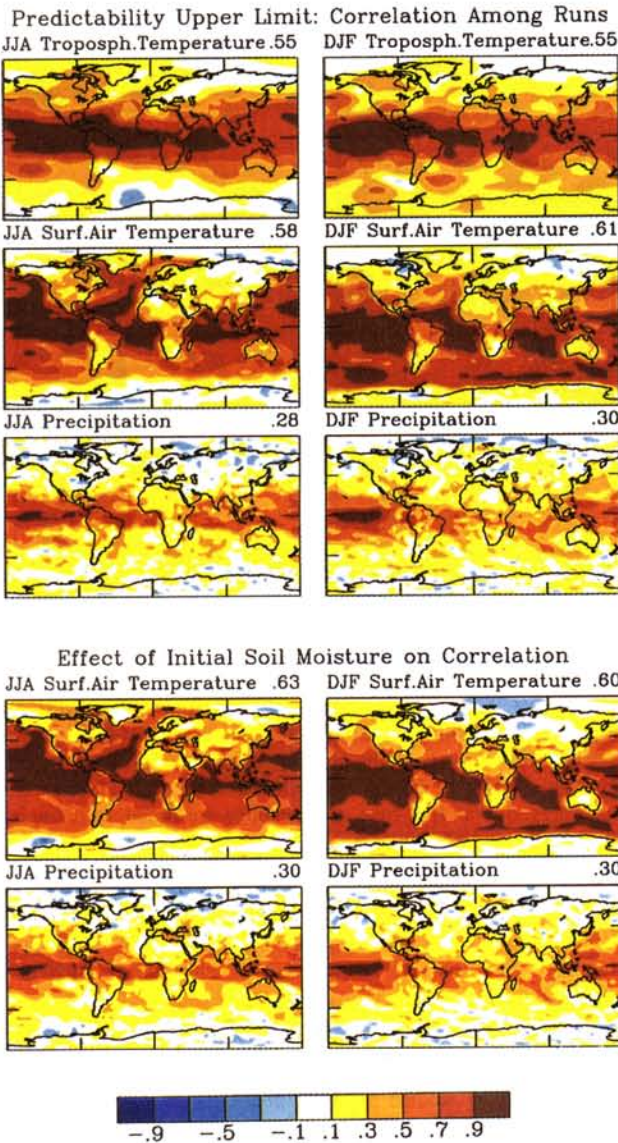
Predictability Upper Limit: Correlation Among Runs

Effect of Initial Soil Moisture on Correlation

Plate 10. Mean correlation of the 10 individual runs Ab with the mean of the other 9 runs, for 17 years (1979-1996) of seasonal-mean tropospheric temperature (MSU2), surface air temperature, and precipitation. The bottom two rows show the impact on calculated predictability caused by perfect knowledge of soil moisture conditions at the beginning of each season.

Plate 10. The results for tropospheric temperature are perhaps the most reliable, because the model does a good job of simulating variability of tropospheric temperature (Plate 6). Over ocean the surface air temperature is more closely correlated with SSTs than the tropospheric temperature, but correlations over land are generally higher for tropospheric temperature. At middle-and high-latitude land areas the predictability of temperature is limited, with correlations less than 0.5, and the predictability of precipitation is small, with correlations less than 0.3.

In principle, actual predictability can exceed that estimated from the correlation among model runs. For example, a seasonal forecast issued the day before a season begins can be based on model runs that use observed initial atmospheric conditions, which can have an influence over more than several days in atmospheric blocking situations [*Shukla*, 1981; *Miyakoda et al.*, 1983], and initial soil moisture values, which can lengthen the timescale of near-surface atmospheric fluctuations [*Delworth and Manabe*, 1993]. On the

other hand, our calculated upper limit assumes perfect knowledge of SSTs throughout the season. As the time constant for decay of SST anomalies is typically of the order of a few months, in practice the presumed or forecast SSTs will be imperfect and tend to reduce the correlation below what we have calculated. Because the factors just mentioned partially cancel, the model correlations are perhaps a reasonable practical estimate of potential predictability.

8.2.2. Models versus real world. Additional information on predictability can be obtained by correlating our model-simulated climate with observed climate of the past 17 years. Plate 11 shows the correlation between MSU2 data and tropospheric temperature produced by the SI95 model for all four ocean representations, in each case including all of the radiative forcings (runs Ae, Bf, Cf, and Df). The correlation measures the average predictability, and, in much of the world, it is primarily dependent on the ability to simulate the large anomalies associated with El Niños and La Niñas [*Barnett*, 1995; *Bengtsson et al.*, 1995; *Brankovic and Palmer*, 1997].

Correlation of Model with Observations

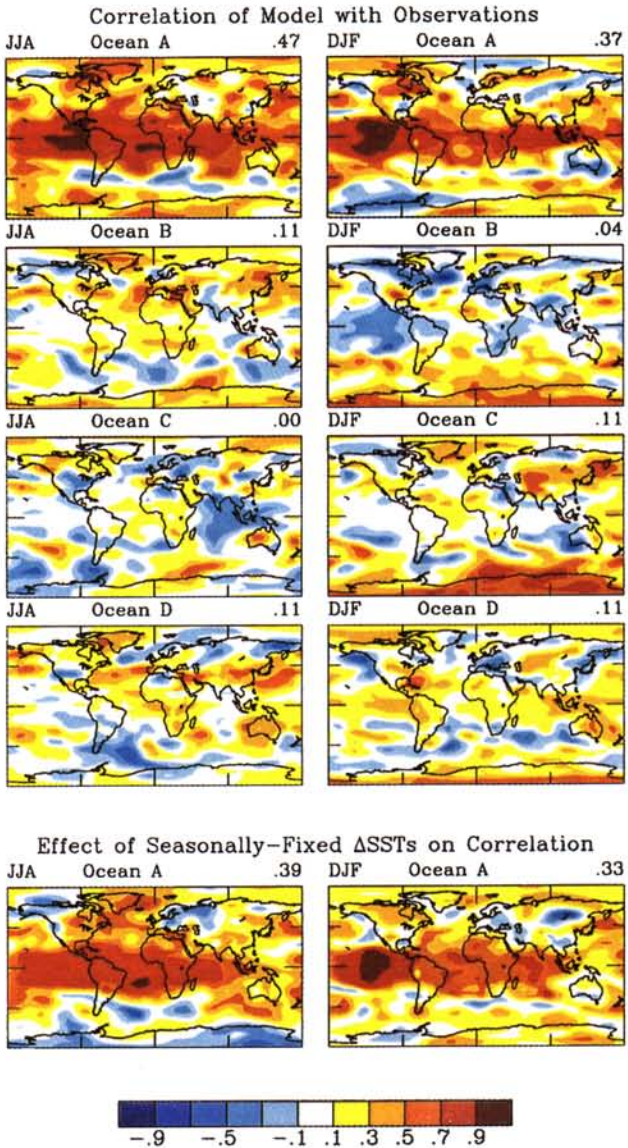## Effect of Seasonally-Fixed ΔSSTs on Correlation

Plate 11. Correlation of observed 17-year seasonal-mean tropospheric temperature variation with five-run mean model simulations, for four different ocean representations (runs Ae, Bf, Cf, and Df). The bottom row shows the impact of keeping the SST anomalies that existed at the beginning of the season unchanged for the entire season.
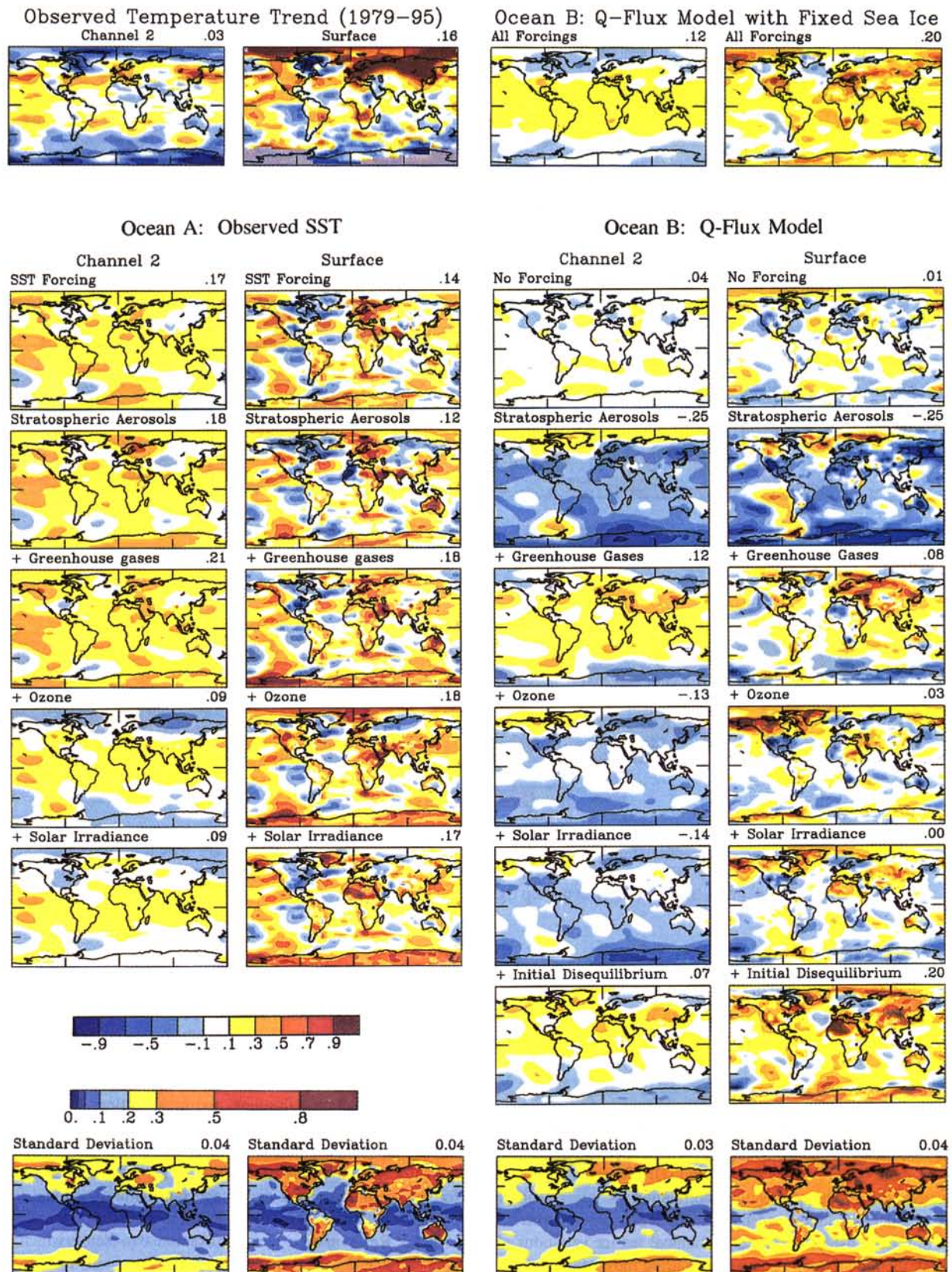
Plate 12a. (Top row) Observed tropospheric (MSU2) and surface temperature changes for 1979-1996 based on linear trends; also (right) ocean B simulations with fixed sea ice for all four radiative forcings and 0.65 W/m² initial disequilibrium forcing. (Middle rows) Five-run-mean simulations of the SI95 climate model using oceans A and B. Results are shown for five and six combinations of forcings for oceans A and B, respectively. (Bottom row) Standard deviation of local temperature trend (and of global temperature trend, given by number in top right) among ensemble members.
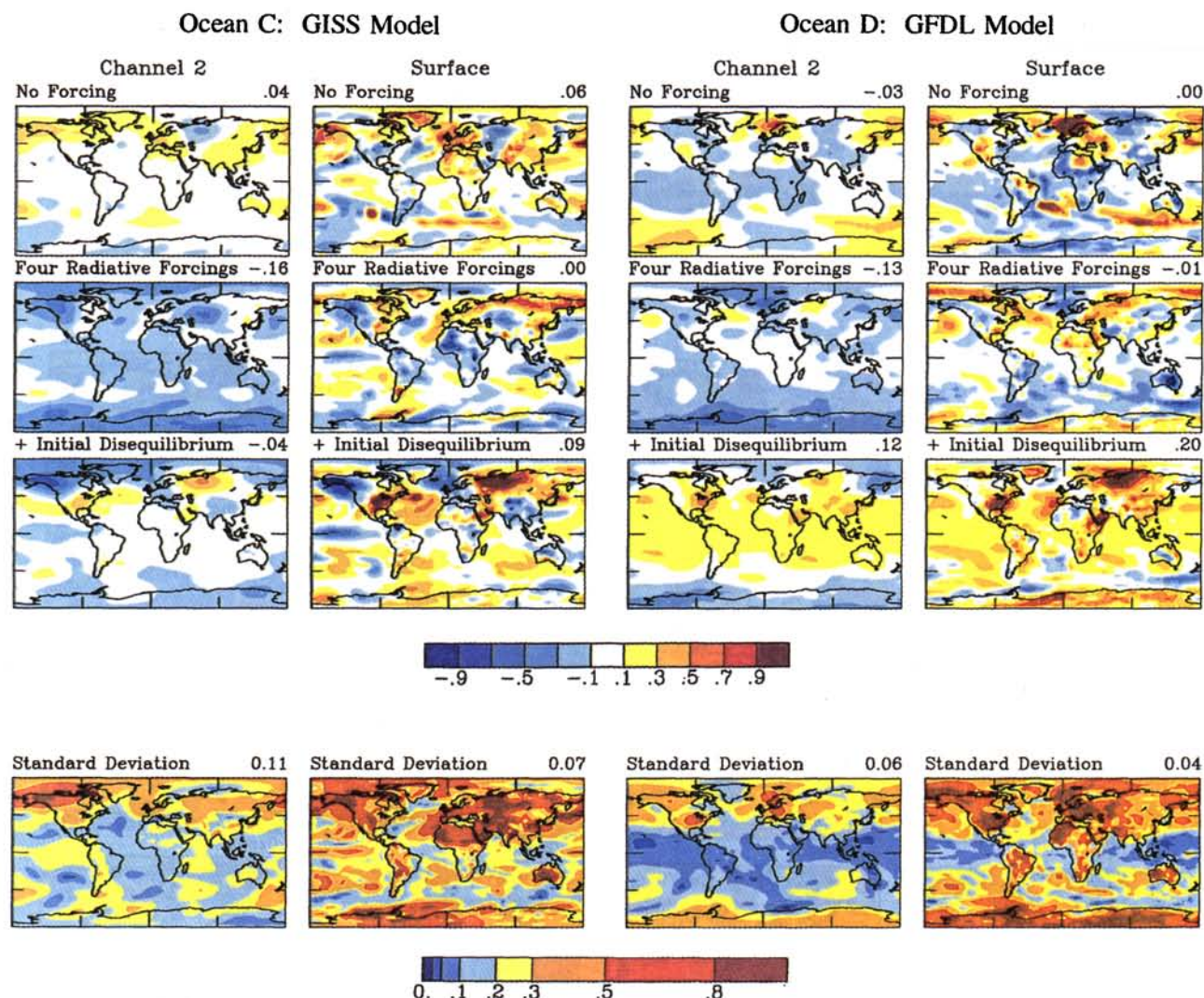
Ocean C: GISS Model

Ocean D: GFDL Model

Plate 12b. Five-run-mean simulations of the SI95 model using oceans C and D. Results are shown for three combinations of forcings. (Bottom row) Standard deviation of local temperature trend (and of the global temperature trend, given by the number in the top right) among ensemble members.

Ocean A, using observed SSTs, is expected to yield a high correlation; but the correlation should be less than the model-model correlation, because (1) the model is an imperfect simulator of atmospheric processes; (2) observations of both SST and tropospheric temperature are imperfect; (3) the model uses climatological (fixed) sea ice, while in the real world, sea ice was variable; (4) the real world radiative forcings are not all included in the model, and those included are imperfectly represented. As it turns out, the correlation for tropospheric temperature goes down only to about 0.42 (average for JJA and DJF) from 0.55. Thus, as expected, the model-observation correlation is lower than the model-model correlation, especially in the sea ice regions where we have not made use of observed interannual sea ice variations. In general, the model does very well, capturing most of the potential predictability suggested by Plate 10. Finally, it is perhaps of interest to compare the predictability achieved by the present model to that obtained by assuming persistence of climate anomalies of the previous season: the model produces a better forecast in both JJA (correlation 0.47 between model and observations, versus 0.36 from persistence) and DJF (0.37 versus 0.27).

Oceans B, C, and D in Plate 11 are forced only by the small radiative forcing for 1979-1996. Thus the degree to which the

models yield a positive correlation is a measure of the contribution of radiative forcing to climate variability on the 17-year timescale. The models suggest that the radiative forcings do provide a positive contribution, averaging about 0.08, to the model-observation correlation. This is a lower limit to the radiative contribution because of inaccuracies in the specified forcings, omission of unmeasured radiative forcings, and imperfections in the model's ability to simulate the impact of the radiative forcings. Furthermore, during this 17-year period the net radiative forcing was small, typically several tenths of 1 W/m^2. This suggests that radiative forcings could become a significant contributor to regional climate change if the forcings reach a sustained magnitude of several W/m^2.

8.2.3. Refinements. Here we examine two factors which could alter our conclusions. First, we test the effect of soil moisture initial conditions on potential predictability of seasonal-mean climate. Second, we quantify the impact of intraseasonal SST variations on calculated predictabilities.

We estimate the influence of initial soil moisture conditions on seasonal climate predictability by making nine additional runs for 1979-1996 similar to runs Ae. In all nine runs at the beginning of each season the soil moisture is reset to be identical to a specific member of the ensemble of Ae runs. Thus these 10 runs should

correlate better with each other than the original 10 Ae runs, to the extent that soil moisture conditions influence seasonal climate. Recent analyses, such as those of *Betts et al.* [1996] and other studies referenced there, indicate that soil moisture conditions have a considerable influence on regional climate for at least several days and possibly much longer.

The results shown in the bottom panels of Plate 10 confirm that the soil moisture initial conditions improve seasonal mean predictability but by a modest amount. Averaged over all land, excluding Antarctica and Greenland, the soil moisture increases the surface air temperature correlation by +0.12 (from 0.33 to 0.45) and the precipitation correlation by +0.03 (from 0.19 to 0.22) in JJA (northern hemisphere summer). As might be anticipated, the changes in DJF are slight (-0.02, from 0.32 to 0.30, for temperature and +0.02, from 0.22 to 0.24, for precipitation). The conclusion that the soil moisture impact is modest is dependent on the realism of our model, especially the ground hydrology. The formulation we employ [*Rosenzweig and Abramopoulos*, 1997] has a large soil moisture capacity, and we doubt that model improvements will alter our conclusion qualitatively.

The second issue we examine is whether the predictability implied by the high model-observation correlation with ocean A is a consequence of the fact that the observed SST that was used to drive the model included intraseasonal (monthly mean) variations. As a test, we considered the extreme case of complete ignorance of intraseasonal change of the SST anomalies, i.e., the SST anomaly at the beginning of each season was kept fixed for that season. As shown by the bottom row of Plate 11, this reduces the mean correlation with observations from 0.42 to 0.36 (the reduction occurring mainly at low latitudes), indicating that most of the seasonal predictability can be obtained without predicting changes of SST anomalies.

8.3. Summary

Most of the interannual variability of regional climate on decadal timescales appears to be chaotic, i.e., nondeterministic, except at low latitudes. This unforced variability places severe limits on regional climate predictability. Nevertheless, model simulations indicate that knowledge of SSTs provides a substantial predictability. Our results suggest that knowledge of initial soil moisture conditions can provide a noticeable improvement in (warm season) predictability.

Although radiative forcings have only a small effect on regional climate variability in this 17-year period, we do find a radiative impact; and we would expect the effect of a steadily increasing radiative forcing, such as anthropogenic greenhouse gases, to increase on longer timescales.

Our quantitative results depend on our climate model's limitations. We anticipate that model improvements, such as higher vertical resolution and better representation of sub-grid-scale processes, may increase the degree of atmospheric teleconnections and thus increase the proportion of deterministic variability, especially in continental regions. But, because of the realistic level of variability in the current model and the model's success in simulating climate change of the past 17 years, we do not expect a qualitative change of our conclusions about predictability.

9. Spatial Distribution of Temperature Change

Our objective here is to compare forced and chaotic climate variations on scales of practical importance and in the process seek signatures of climate change due to natural and anthropogenic

climate forcings. We first present global maps of the 17-year temperature change, maps being a result that is easy for people to relate to. We then examine temperature change as a function of season, latitude, and height.

9.1. Global Maps: Temperature Trends

We examine global maps of annual-mean temperature trends for 1979-1995. Trends for such a short period are not very meaningful; that is, they fluctuate as a few years of additional data are added. Nevertheless, study of the global distribution of the response to radiative forcings at least can help define what to look for on a longer timescale.

The observed temperature trends for the troposphere (MSU channel 2) and surface are shown on the left side of the top row of Plate 12. The observed surface temperature is the land-ocean index of *Hansen et al.* [1996b], based on surface air measurements over land and SSTs over the ocean. Note that some regions of strong surface warming, such as Europe and eastern Siberia, have much weaker warming at the levels sampled by MSU2. There is a tendency at high latitudes for cooling at the MSU2 level relative to the surface. On the other hand, MSU2 tends to be warming slightly relative to the surface in some low-latitude ocean regions. On the global average the surface has a warming of 0.16°C over the period 1979-1996, while MSU2 has only a slight warming of 0.03°C.

Ocean A (observed SSTs) five-run mean results are shown for no explicit radiative forcings and with addition of each successive radiative forcing. Despite the fact that specified SSTs strongly constrain the atmospheric thermal response, some of the radiative forcings have detectable effects on the global mean, which differ in magnitude at the MSU2 and surface levels.

The numerical significance of changes can be estimated from the standard deviation of the 17-year temperature trends among the ensemble members (Plate 12). For oceans A and B it is the average over all the sets of forcings. That is, for a given forcing, say stratospheric aerosols plus ozone change, the standard deviation is computed from the results of the five runs; the mean is then calculated for the five different sets of forcings. Crudely, if the calculated change in the five-run mean result is as large as this standard deviation, it is significant at about the 90% level; if it is twice as large, it is significant at the 99% level. But of course high numerical significance due to any forcing does not imply detection of its effect in the real world, which depends upon identification of climate change characteristics that are unique among candidate forcings.

For ocean A the largest radiative effects are cooling due to ozone change (largest at MSU2 level) and warming by the homogeneously mixed greenhouse gases (largest at the surface). Slight warming at the MSU2 level is caused by stratospheric aerosols due to the high-altitude tail of the MSU2 weighting function [*Hansen et al.*, 1996a, Table 1], which extends into the stratosphere where the Pinatubo aerosols cause warming. The net result of all the forcings is warming at the surface and a smaller warming at the MSU2 level, roughly consistent with the observations. We examine the altitudinal variation of the temperature change explicitly in section 9.4.

Ocean B (*Q* flux model) allows the surface and atmosphere to respond fully to the radiative forcings, thus revealing a clearer influence of each forcing. The Pinatubo aerosols by themselves cause a strong cooling trend, but this is more than offset by warming due to the well-mixed greenhouse gases. Ozone depletion causes a substantial cooling, especially at the MSU2 level, and the cyclic solar variability yields a slight further cooling. The net effect of the four measured radiative forcings is zero global mean trend at the

surface and significant cooling at the MSU2 level. Addition of the 0.65 W/m^2 initial disequilibrium forcing yields global warming trends slightly larger than observed at both the MSU2 and the surface levels.

Plate 12a, in the top right-hand corner, presents results for ocean B with fixed sea ice, driven by all the radiative forcings. There is little difference compared with the standard ocean B result, except in some sea ice regions. Apparently, the small and oscillating magnitude of the forcing (Figure 4), and the long response time of the ocean at high latitudes, limits the global impact of sea ice feedback in this 17-year period.

Plate 12b shows the 17-year temperature trends simulated using the dynamical ocean models. None of the models yields Arctic-Eurasian warming as intense as observed, although there is Asian warming with all three predicted ocean models. But we show below that the intensity of the observed high-latitude warming is in part a fluke of an extreme year at the end point of the 17 years.

9.2. Global Maps: Seasonal Anomalies

The large unforced variability of regional climate (section 8) implies that it will be difficult to detect the impact of a small forcing in any specific region. The best chance for a detectable regional response in 1979-1996 probably is provided by the Mount Pinatubo radiative forcing of -3 W/m^2 (Figure 4). Thus as an example of regional seasonal response to a radiative forcing, we choose the summer and winter seasons when Pinatubo would be expected to have its maximum effect.

The top row of Plate 13 shows observed surface air temperature anomalies for JJA, 1992 and DJF, 1991-1992. The same row shows twice the standard deviation of temperature for these seasons based on data for the period 1951-1980 (the probability of the observed anomaly at a given location exceeding 2σ by chance, with the expected sign, is about 5%). In JJA 1992, there is a 4σ observed cooling in the middle of North America and a cooling almost that large in Asia. The centers of these continents are the a priori places to look for a summer response to a large short-term radiative forcing. Thus these regions of summer cooling are good candidates for being a response to Pinatubo forcing. Winter warmings in North America and Europe are also a predicted response to volcanic aerosols [*Robock and Mao*, 1992; *Graf et al.*, 1994]. The observations of DJF 1991-1992 show warmings in those regions (top row, Plate 13), but the magnitude does not exceed the 2σ natural variability, so it is more difficult to ascribe an association with the volcano.

Plate 13 also shows simulated summer and winter temperature anomalies after Pinatubo for individual and five-run means (oceans A and B). There is a tendency for summer cooling in North America and Asia, which is apparent in the five-run means. But individual runs vary considerably, even as to the sign of the anomaly. Because the real world only ran through the experiment once, unforced variability makes it difficult to associate any specific feature with the small radiative forcing. This is especially true in the winter, when the unforced variability is much larger than in the summer. Some individual model runs yield winter warming over North America and/or Europe, but there is little tendency for that result in the mean response.

In the real world there may be a stronger winter response to stratospheric aerosol forcing than that in our model. Consistent with that possibility, we noted in section 8 that the model's variability in winter over North America and Europe is smaller than in observations. As discussed in section 3.11, we do not expect the SI95 model to do a good job of simulating phenomena dependent on dynamical interactions of the stratosphere and troposphere, such as hypothesized to occur after large volcanos [*Kodera and Yamazaki*, 1994; *Graf et al.*, 1994].

Despite this caveat, it is clear from the results in both this section and section 8 that unforced interannual variability of regional temperature represents a large fraction of observed variability. This evidence suggests that a seasonal climate anomaly in any given region cannot be categorically "blamed" on a radiative forcing of the magnitude we have considered. However, a forcing may alter the probability of the climate anomaly occurring.

9.3. Zonal Temperature Trends

Plate 14 shows observed and modeled zonal-mean surface air temperature changes for 17 years 1979-1996 (March 1979 to February 1996). Results are given for individual seasons, JJA and DJF, for no radiative forcings and all radiative forcings. The effect of the forcings is not large compared with unforced variability, which is large even in the zonal mean, especially at high latitudes.

The bottom row of Plate 14 shows vividly the difficulty of attaching significance to a 17-year change of surface temperature. Shifting the period by 1 year, thus adding the unusually cool season DJF 1978-1979, alters the global-mean change based on the 17-year trend from 0.08°C to 0.15°C, and as shown on the bottom right, it changes the results at high northern latitudes by a much larger amount.

This chaotic variability of temperature at high latitudes must be recognized when temperature records are used to assess mechanisms of climate change. For example, trends of high-latitude temperatures are sometimes taken as being discrepant with expectations of greenhouse warming [*MacCracken*, 1983; *Idso*, 1983]. Zonal variations of climate change are a valuable test of our understanding of climate feedbacks, but the large chaotic variability of temperature at high latitudes can mask on the decadal timescale zonal trends that may be present on longer timescales [*Hansen et al.*, 1983b].

For the sake of brevity we do not show the results as individual forcings are added one by one. Such results, as suggested by Plate 14, yield the conclusion that the zonal-mean surface air temperature provides little discrimination among radiative forcings for the 17-year period of our present study. A much more sensitive indicator of forcings is provided by the air temperature aloft, as shown in the next section.

9.4. Vertical Profile of Temperature Change

Figure 6 shows how the vertical profile of temperature is altered by each radiative forcing for oceans A and B. Some forcings have a large impact on the lapse rate, far exceeding unforced variability among model runs. The dominant effect on lapse rate is due to ozone change, which causes strong cooling in the 10-20 km range. The ozone cooling near the tropopause, about 1°C, dramatically alters atmospheric temperatures, reversing the expected warming effect of well-mixed greenhouse gases and steepening the lapse rate in the upper troposphere. Increasing CO_2 cools the middle and upper stratosphere, although the crude vertical resolution in our present model may not precisely describe this cooling.

We would like to compare the calculated temperature profiles with available observations which include surface, MSU, and radiosonde data. Each of these data types has limitations and uncertainties. The radiosonde data are particularly important for our present purpose, because they are the only available data with high vertical resolution. However, the radiosonde data need close scrutiny because of several sources of temporal inhomogeneity [*Gaffen*, 1994]. The radiosonde data is especially uncertain above the 100 mbar level, where it is much less complete; also, it is suspected that at upper levels, instrument changes [*Gaffen*, 1994] and/or temporal changes in balloon survivability at low temperature [*Parker and Cox*, 1995] could introduce a spurious cooling trend.
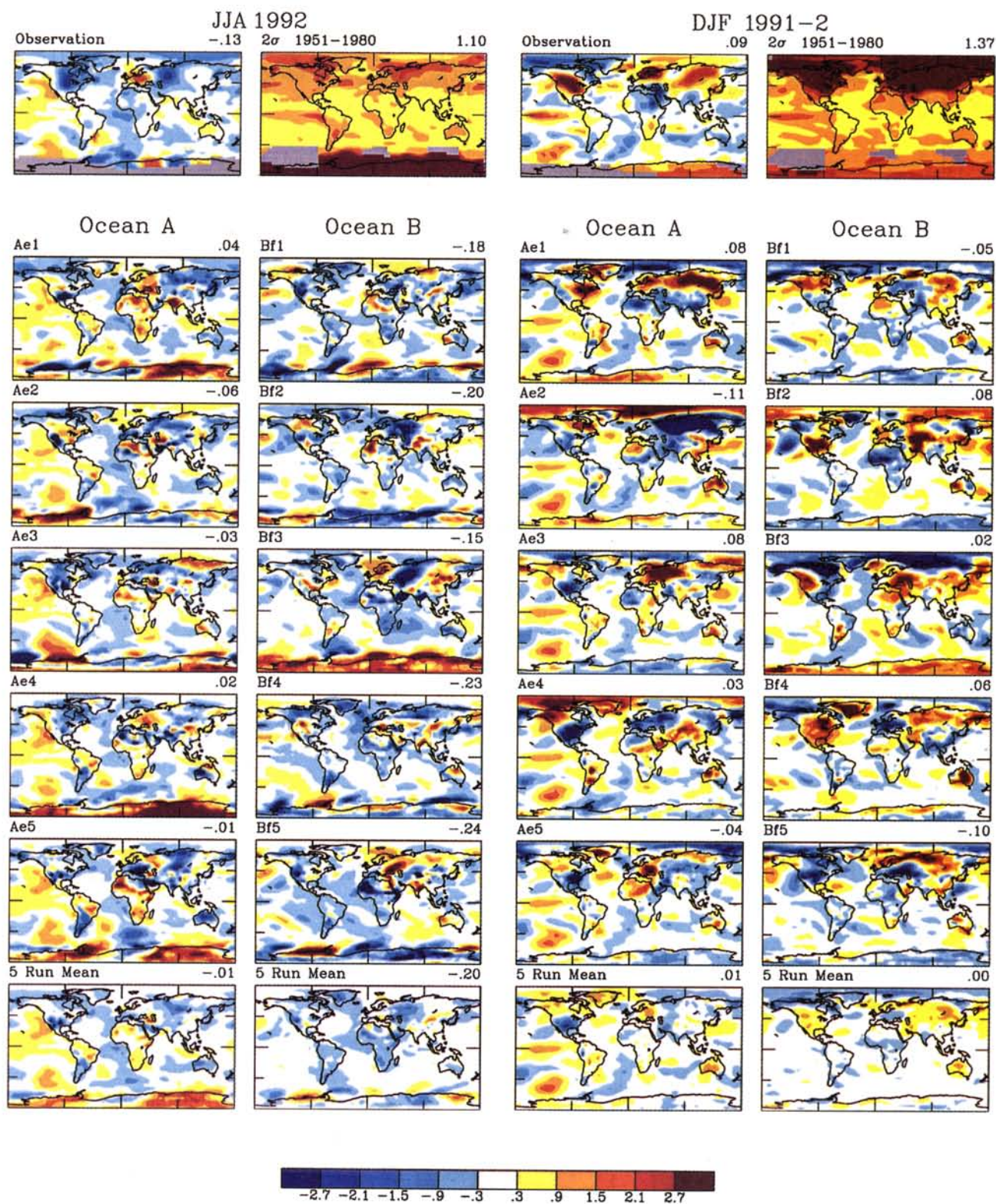
Surface Temperature Anomaly (°C)

Plate 13. Surface air temperature anomalies for JJA 1992 and DJF 1991-1992 relative to the base period 1979-1990. (Top row) Observed anomalies and standard deviations, the latter based on the period 1951-1980. (Next five rows) Results of the five individual runs for ocean A and B with all radiative forcings. (Bottom row) Five-run means.
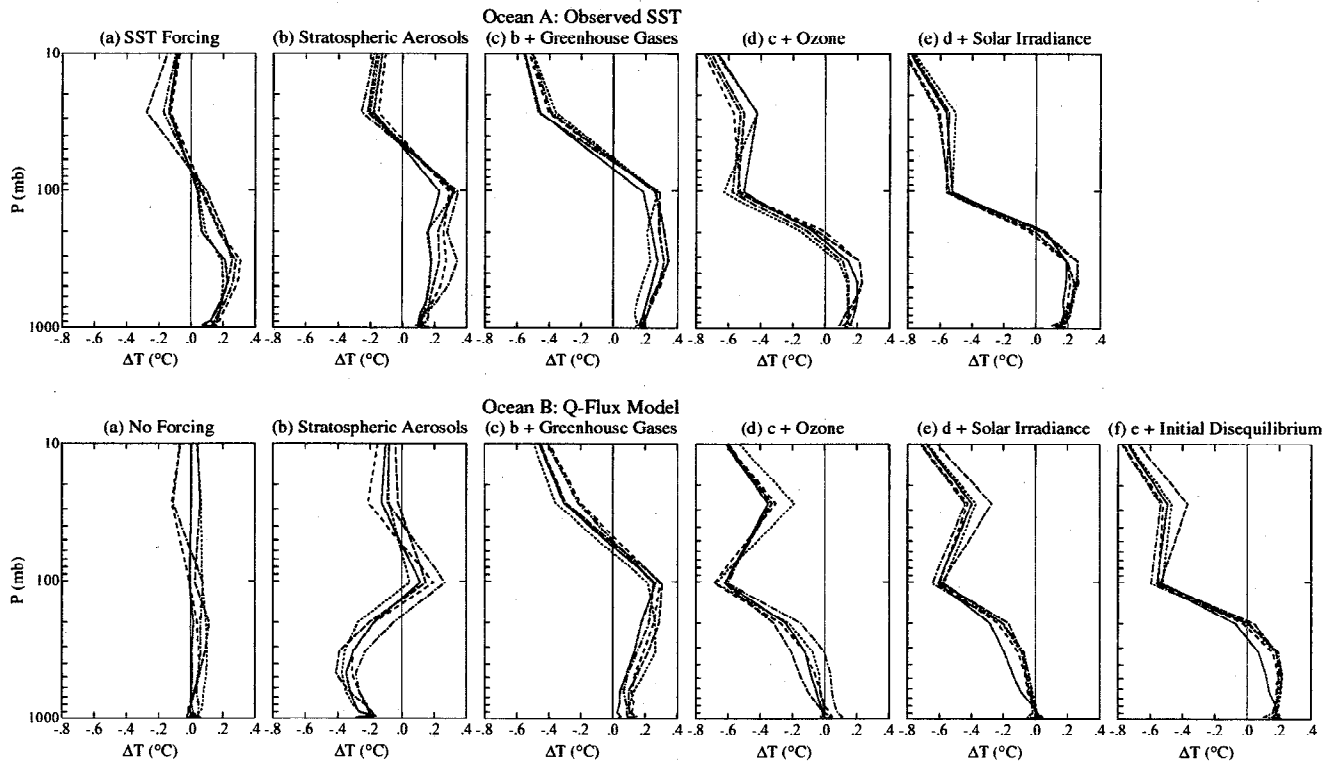
Plate 14. Change of seasonal-mean zonal-mean surface temperature for 1979-1996 based on linear trends. Observations are the land-ocean temperature index of *Hansen et al.* [1996b]. Model results are for individual runs with either no forcing or all radiative forcings included. The bottom row shows the large effect on observed temperature change caused by shifting the period by one year, thus adding the unusually cool season DJF 1978-1979.

Figure 6. Change of global-mean annual-mean temperature profile for 1979-1995 based on linear trends. Results are shown for individual model runs. Radiative forcings are added one by one for ocean A (observed SST) and ocean B (Q flux model).

We have screened the radiosonde data, in two alternative ways, to try to minimize the effect of temporal inhomogeneities, as summarized below. Details of the screening procedure will be presented elsewhere, and the analyzed radiosonde data are available from us. Because of the inchoate state of profile analyses and verifications, we limit our conclusions to a few general statements about the tropopause and lower troposphere regions.

Our first screening method checked the consistency of the 1979-1996 temperature record of each radiosonde station (weighted by the MSU vertical weighting function) against the measured MSU temporal variation at the location of the radiosonde station, culling and retaining those stations with an RMS difference less that 0.5°C for the full period of data. The radiosonde stations surviving this screening provide good coverage in the northern hemisphere and useful coverage in the southern hemisphere.

Our second screening method is to use only those radiosonde stations which one of us (DJG) found to meet rigorous standards for metadata availability as well as continuity of instruments and measurement procedures. This alternative represents an extreme; although middle- and high-latitude stations have not been examined yet, in the tropics, only three stations have been identified which meet these criteria. We show results for each of these stations, thus providing examples of local temperature profile variability.

Figure 7 compares the simulated 17-year change of temperature profile with the radiosonde, surface, and MSU observations. The simulated temperature changes are reasonably consistent with the global, hemispheric, and local observations. The discrepancy at Koror Island may be in part a matter of horizontal resolution, as the 17-year observed SST change averaged over the GCM grid box is 0.0°C while the radiosonde profile suggests surface cooling of -0.4°C at the radiosonde site.

Plate 15 shows the latitude-altitude dependence of the observed and calculated zonal-mean temperature change. Similar results were

presented by *Hansen et al.* [1993] based on calculations with a sector climate model. Our comments here refer to two levels of the atmosphere: the near-tropopause region and the lower troposphere.

9.4.1. Tropopause region. The observations indicate good agreement with the strong cooling in the tropopause region, cooling which occurs in the model as a result of ozone change. This ozone cooling is sufficient to move the level at which the profile switches from warming to cooling by about 10 km on global average, from about the 50 mbar level to the 200 mbar level. The radiosonde data seem to be consistent with this global-mean result, although there are reasons to suspect that the downward movement of the switchover level could be exaggerated in both the model and the data: the assumed ozone loss in the 15-20 km region, based on SAGE data, may be excessive [*Wang et al.* 1996], and observed cooling at these altitudes may be exaggerated by the effect of instrument changes [*Gaffen,* 1994] and balloon survivability [*Parker and Cox,* 1995]. Nevertheless, the switchover is clearly at much lower altitudes, in both model and data, than it would be in the absence of ozone loss, and it occurs at higher altitudes at low latitudes than at high latitudes.

Specifically, the temperature change profile represents evidence of ozone depletion in the tropopause region, as has been pointed out before [*Hansen et al.,* 1993; *Ramaswamy et al.,* 1996; *Tett et al.,* 1996]. No other mechanism has been demonstrated to cause a temperature change approaching that observed. In the tropics, compared to high latitudes, the modeled and observed coolings are limited to higher levels, yet the tropical cooling extends to much lower levels than it would in the absence of ozone effects. The tropical cooling provides support for the SAGE measurements of ozone depletion in the tropical tropopause region. Although Total Ozone Mapping Spectrometer (TOMS) measurements [*Stolarski et al.,* 1991] of column ozone show little change in the tropics, it is possible that ozone loss in the tropospause region is partially
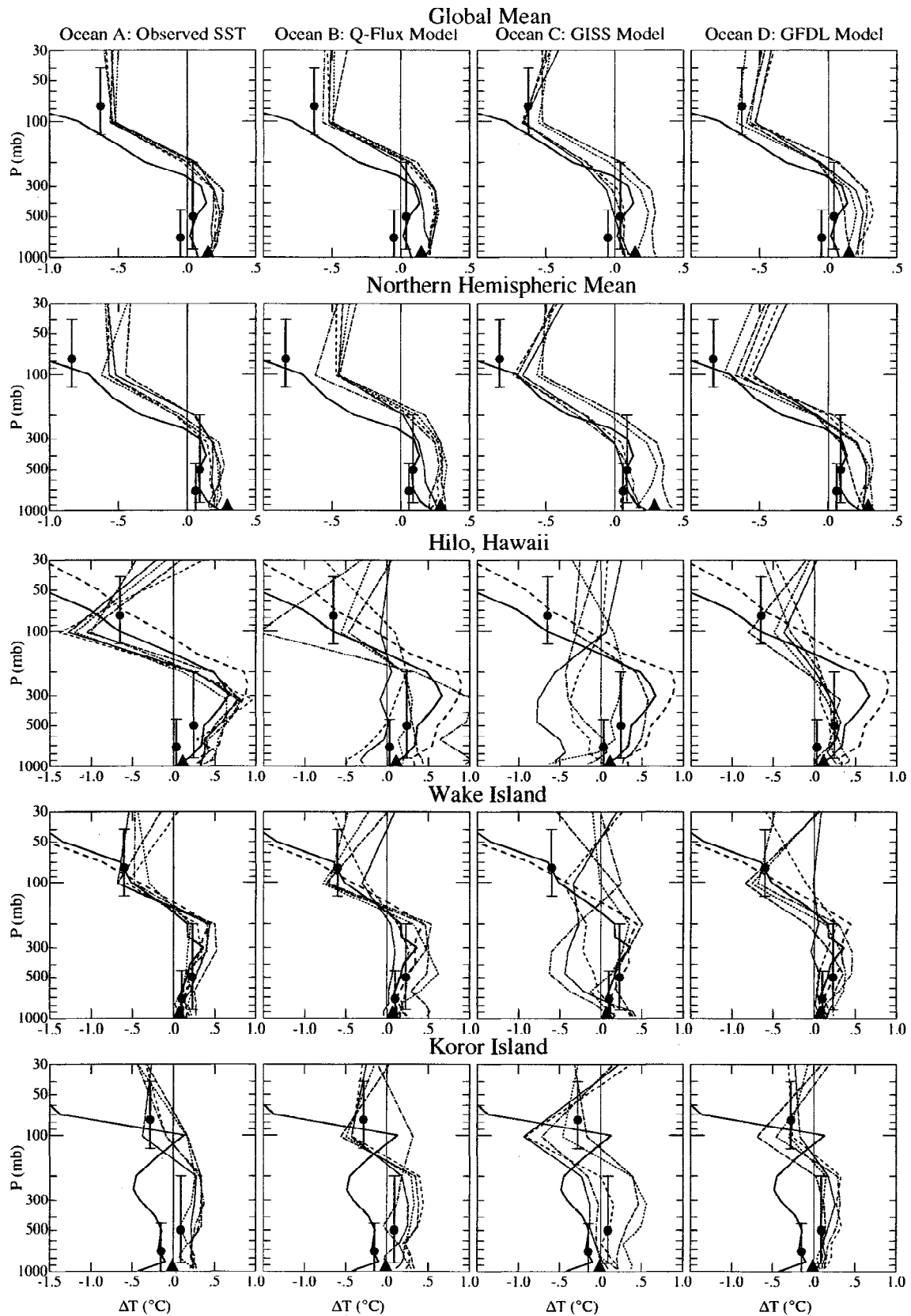
Figure 7. Change of annual-mean temperature profile for 1979-1995 based on linear trends. Model results are for all four oceans for the case with all four radiative forcings plus (for oceans B, C, and D) the 0.65 W/m^2 initial disequilibrium. Surface observations (triangles) are the land-ocean data of *Hansen et al.* [1996b]. The arrows on the MSU satellite data [*Christy et al.*, 1997] indicate the height ranges that contain 70% of the signal for MSU4 and MSU2 and 85% of the signal for MSU2R. The radiosonde profiles (solid curve 0000 UT, dashed curve 1200 UT) become unreliable above about the 100 mbar level.

balanced by tropospheric ozone increase [*Ziemke et al.*, 1996; *Portmann et al.*, 1997]. Recent refinements of SAGE data analyses [*Wang et al.*, 1996] reduce the estimated tropopause ozone loss, but they would not qualitatively alter our results.

An alternative interpretation (popular among critics of "global warming," but apparently unpublished) is that the absence of strong upper tropospheric warming is evidence that climate models are flawed, because models forced only by well-mixed greenhouse gases show strong warming in the upper troposphere [*Manabe and Wetherald*, 1980; *Hansen et al.*, 1984]. Specifically, it is argued that the cooling is an indication of a negative water vapor feedback. However, our results, obtained with a model that has a strong positive water vapor feedback and is driven by measured radiative forcings, are consistent with observed temperature change and indicate that ozone depletion has reduced the upper tropospheric warming. If our interpretation is correct, during the next 5-10 years, as ozone depletion levels out and perhaps reverses, warming of the upper troposphere by well-mixed greenhouse gases should become apparent.

9.4.2. Lower troposphere. There are differences between the modeled and observed tropospheric temperature profiles (Figure 7). But there are uncertainties in the observed temperatures, in the radiative forcing data, and in the climate models, which make it difficult to draw firm conclusions from the apparent differences. For this reason we focus here on the uncertainties and how these may be alleviated in future analyses.

First we note that although the different types of observations appear to be in rather good agreement, this may be somewhat deceptive. One problem is the poor spatial coverage of the radiosonde stations, especially in the southern hemisphere. When we sample MSU2R data at the radiosonde locations, the MSU2R temperature change is about $0.1°C$ cooler over 17 years than its true global average, thus increasing the discrepancy with the radiosonde result. Also, the process that we used to cull the radiosonde data (by eliminating stations that had large RMS differences with MSU2) caused a cooling of more than $0.1°C$ in the resultant radiosonde tropospheric temperature change over 17 years. Although this culling procedure was intended to remove radiosonde stations with temporal discontinuities, if there is any cooling bias in MSU2, the culling process may have transferred that bias partially to the radiosonde result.

Note also that MSU2, with weighting function peaking in the upper troposphere, shows global warming, while MSU2R has global cooling. The difference between MSU2 and MSU2R becomes of greater interest when it is realized that the MSU weighting function contains a large contribution from the stratosphere, which is known to have cooled rapidly in this period. If the stratospheric tail is removed, the MSU2 temperature trend moves about $+0.1°C$/decade in Figure 7. Thus if both the MSU2 and MSU2R data are correct, the lower troposphere cooled strongly relative to the upper troposphere. The radiosonde data suggest a relative change of that sense, mainly in the southern hemisphere, but not of the magnitude indicated by MSU. We note that we have already included the recent $+0.03°C$/decade revision of MSU2R (J. Christy, private communication, 1997), otherwise the difference between MSU2 and MSU2R would have been greater. *Hansen et al.* [1995a] and *Hurrell and Trenberth* [1997] have suggested that further positive revision of MSU2R may be needed, but the case has not been proven.

We conclude, regarding data, that an independent measure of the vertical profile of temperature change is needed. Satellite infrared

sounding data, which have been acquired since the late 1970s for weather forecasting purposes, provide the possibility of such data. Development of a data set from the infrared measurements, even though it may be restricted to cloud-free regions, deserves high priority.

The radiative forcings that we have employed do not seem to cause a cooling of the lower troposphere relative to the upper troposphere. But we were unable to include either the direct or the indirect (from induced cloud changes) radiative forcing due to changes of tropospheric aerosols. Such forcings are perhaps the most likely to have caused alterations of the temperature profile within the troposphere. If the spatial and temporal distributions of such forcings could be estimated, for example from a combination of satellite data, aerosol models, and in situ data, it is would be possible to search for their influence and possible signature in the four-dimensional temperature fields.

It is also possible that deficiencies in the climate model itself may make the model incapable of properly simulating changes in the vertical temperature profile. For example, the next version of our model will have higher vertical resolution. However, higher resolution per se, with our present forcings, is not likely to cause a cooling of the lower troposphere with warming of the surface and upper troposphere.

The most likely cause of such a profile is probably a forcing that causes increased low-level clouds and thus cooling of the lower troposphere. Together with overall tropospheric warming from increasing greenhouse gases, the qualitative profile suggested by Figure 7 could be produced. We have argued on the basis of observed changes in the diurnal cycle of surface air temperature [*Hansen et al.*, 1995c] and on the basis of other data [*Hansen et al.*, 1997a] that the dominant global climate forcings over the past several decades have been increases of greenhouse gases and low clouds.

9.4.3. Summary. The vertical profile of temperature change is a sensitive diagnostic of climate change mechanisms. *Vinnikov et al.* [1996] showed that the range of unforced variability of the global-mean lapse rate is small. This is also illustrated in the bottom left corner of our Figure 6. The unforced variability is much smaller than observed lapse rate changes or simulated changes for several radiative forcings.

The large effect of ozone depletion on the global temperature profile in the climate model simulations is consistent with observed temperature trends as previously noted [*Hansen et al.*, 1993; *Ramaswamy et al.*, 1996; *Tett et al.*, 1996]. In turn, this supports our calculation of a large forcing (-0.3 W/m^2) due to ozone depletion (the cooling at these levels is the mechanism by which the forcing works). But these results need to be refined with a model having higher vertical resolution, capable of accurately representing dynamical effects, and more precise determination of the ozone change is also needed.

In the lower troposphere, MSU2R data yield a slight global cooling trend, while other observations (including MSU2) and the model simulations indicate warming. Quantitative analysis of the differences is beyond the scope of this paper, but it has been noted [*Hansen et al.*, 1995a] that the MSU2R trend is sensitive to several factors, including changes of atmospheric hydrometeors [*Prabhakara et al.*, 1995], surface emissivity variations, and satellite-to-satellite calibration transfers [*Hurrell and Trenberth*, 1997]. The vertical profile of temperature change may also be affected by direct and indirect aerosol forcings, but these have not been measured.

10. Discussion and Conclusions

10.1. Inferences: Forcings Versus Chaos

10.1.1. Planetary disequilibrium. We find evidence of a current planetary radiative disequilibrium of about +0.5-0.7 W/m^2; that is, the Earth is absorbing that much more energy in solar radiation than it is emitting in thermal radiation to space. The basis for the finding is the observed surface warming over the period 1979-1996, a period with essentially null net-measured radiative forcing. The observed warming exceeds unforced variability among model runs. This analysis could be altered by substantial unmeasured forcings. But the principal suspected unmeasured forcing, related to increasing tropospheric aerosols, is believed to cause a negative forcing, which would increase the inferred radiative disequilibrium.

The estimated planetary radiation imbalance is too small to measure directly, but the excess heat must primarily be accumulating in the ocean. The implied ocean temperature change could be measured readily, but a sufficient coverage of ocean soundings is not available. The most practical measurement approach is perhaps acoustic tomography [*Munk and Forbes*, 1989]. The planetary heat gain also implies a measurable sea level rise due to thermal expansion of ocean water, about 12 mm over 1979-1996, including +8 mm during 1993-1997 and -5 mm during 1991-1992. Observed sea level change in the last four years is consistent with this, but interpretation of observations also requires measurement of ice sheet volume changes. Such measurements are possible with aircraft or satellite lidar systems, but they are not presently being carried out for Antarctica.

The planetary radiation imbalance, averaged over several years to remove short-term variability such as that due to El Niños, captures in a single number a fundamental measure of the state of the climate system. It is an integrated effect of all past climate forcings, measured and unmeasured, and climate sensitivity [*Hansen et al.*, 1984]. Our estimate of a current disequilibrium of +0.5-0.7 W/m^2 implies that further global warming of about 0.5°C is already "in the pipeline"; that is, it will occur over the next century even if CO_2 and other climate forcings are kept fixed at today's amounts. Thus quantification of the radiation imbalance has practical importance, because it is the possible existence of such "unrealized warming" that makes a global climate change policy of "wait and see" problematical and perhaps dangerous. The long lag in the realization of warming distinguishes the greenhouse effect from other environmental issues, such as ozone depletion, in which further ozone depletion stops when the depleting chemicals are stabilized.

Improved quantification of the planetary radiative imbalance, which is possible as the period of satellite data gets longer, is needed. Suppose, for example, that we have overestimated the imbalance due to error in measured surface temperature change and inherent variability in the single 17-year "run" of the real world, such that the true imbalance is only +0.25 W/m^2. Such an imbalance would imply that either the radiative forcing estimated for the past century [*IPCC*, 1995] is too large or the climate sensitivity is smaller than is generally believed. On the other hand, if the imbalance is +0.75 W/m^2, the warming of 0.6°C in the past century is only half of the eventual warming that will be caused by the existing atmospheric composition. More accurate quantification of the imbalance can be made by using the method of this paper, if the major radiative forcings are monitored, including tropospheric aerosols. An

alternative approach, or a check, would be to measure the rate of heat storage in the ocean.

The radiative imbalance that we have calculated has implications for expected global temperature change in the near term. This imbalance drives the planet toward higher temperatures, causing 14 of our 15 simulations with all forcings to yield at least one annual global-mean temperature in the period 1997-1999 higher than that in any previous year. Thus barring the unlikely event of a large volcanic eruption, we project that a new global temperature "record" is likely in the next three years.

10.1.2. Detection of climate change. We find that several radiative forcings have impacts on simulated global temperature exceeding unforced model variability, despite the brief 17-year period considered. The forcings that yield obvious effects are stratospheric aerosols, ozone, and well-mixed greenhouse gases, thus both natural and anthropogenic forcings. Of these, the volcanic aerosol and ozone forcings leave distinctive signatures in the simulated climate change, which are also apparent in observations.

One result that differs from conventional wisdom is the large climate impact of ozone change. *IPCC* [1995], for example, estimates the forcing due to ozone depletion as -0.1 W/m^2, which is negligible compared to other uncertainties. But we calculate an ozone forcing of about -0.3 W/m^2 [*Hansen et al.*, 1997b], and our Figure 6 and Plate 15 dramatically illustrate the effect of this estimated ozone change on tropospheric temperature. The principal reason for the small forcing found by *IPCC* [1995] is their assumed profile of ozone change, as shown by *Hansen et al.* [1997b]. The approximate agreement of our present simulations with observed temperature change provides support that our ozone change forcing is realistic.

The response to solar forcing is small in our simulations, less than the variability among ensemble members. But we do not conclude that solar effects are negligible in the real world, where considerable empirical evidence of solar climate effects has been found. There may be climate change mechanisms not simulated well in our present model, for example via effects of solar ultraviolet variations in the stratosphere. Furthermore, solar effects are suspected to be larger on longer timescales.

The brevity of the simulated period and the thermal inertia of the ocean hinder interpretation of surface temperature change, which is small in both model and observations. But the observed large changes of temperature in the stratosphere and tropopause regions confirm that the radiative mechanisms of climate change are at work and must be tending to influence surface climate. Indeed, observed surface temperature changes, despite their small magnitude, contain strong evidence of response to the radiative forcings.

10.1.3. Regional climate predictability. Posterior analyses of seasonal climate anomalies [*e.g.*, *Trenberth and Guillemot*, 1996] may leave the impression that the regional anomalies are largely a consequence of SST and other external forcings. If this were true, it would imply that seasonal climate anomalies are highly predictable. Such a conclusion would have welcome practical implications, and it would encourage a common tendency, among lay people and scientists, to associate causal mechanisms with climate fluctuations. But our quantitative estimates of the magnitudes of forced and chaotic climate variations on regional scales suggest caution about inferences of dominant causality and predictability.

Our global maps of the correlation among ensembles of simulations differing only because of unforced atmospheric variability, together with maps of the correlation between

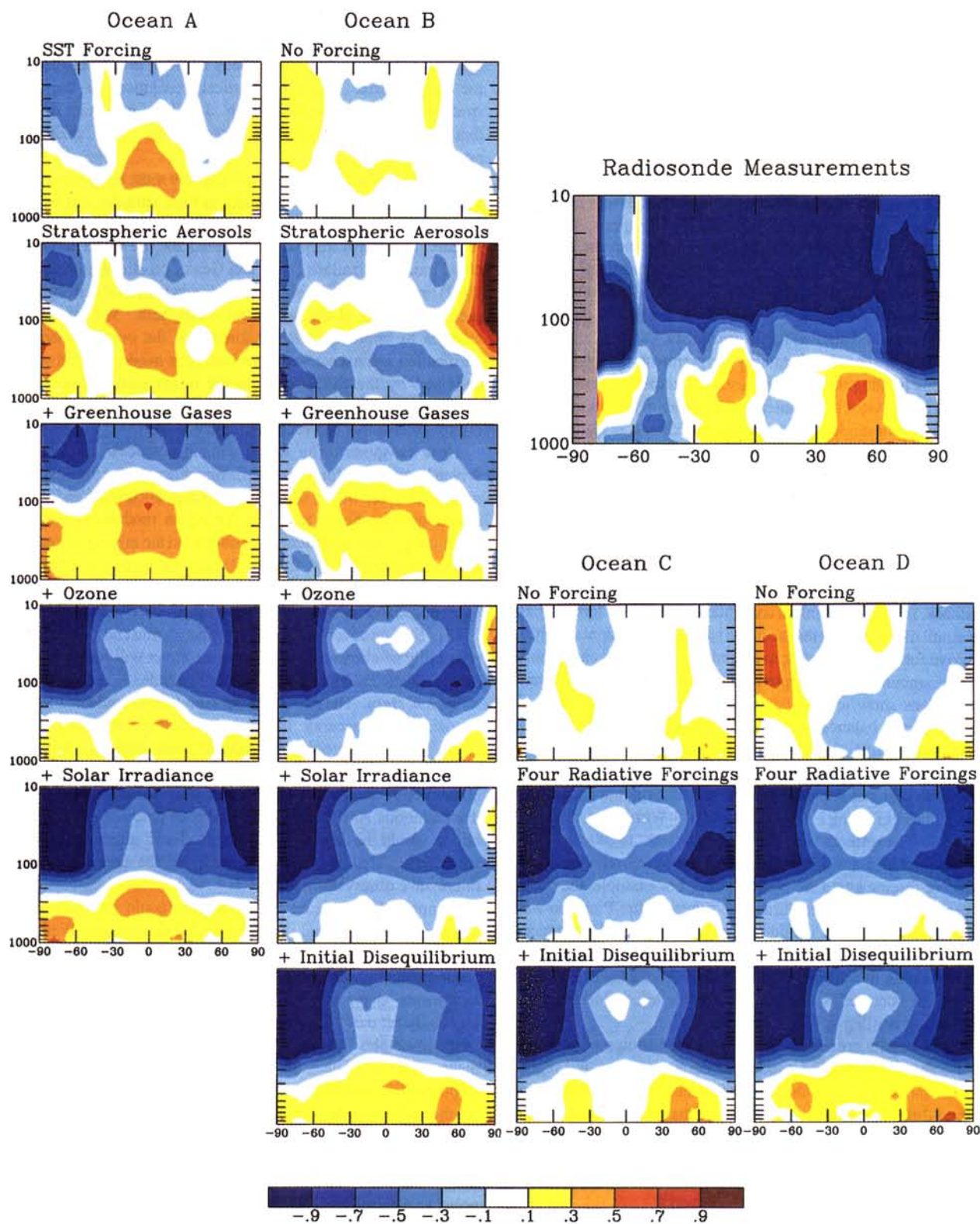# Temperature Change (1979-95)

Plate 15. Change of zonal-mean annual-mean temperature for 1979-1995 based on linear trends. Radiosonde data are shown at top right; other figures show model results for four oceans, with several combinations of forcings.

observations and simulations, provide insight about regional climate predictability. These correlations imply severe limitations on potential regional climate predictability at middle latitudes, even with perfect knowledge of antecedent climate boundary conditions. That conclusion is qualitatively consistent with previous predictability studies [*Lorenz*, 1982; *Charney and Shukla*, 1981].

We suggest the following construction of regional climate variability. Posterior climate analyses can provide a description of climate anomaly patterns, relating them to boundary conditions and feedbacks, including SSTs and soil moisture. But if the real world were to run through the same period again, the climate patterns would be different. Posterior analysis could again relate the regional climate anomalies to boundary conditions and feedbacks, but it would be describing a different anomaly pattern. Thus such analyses should be viewed as descriptions of the event, not as an indication of predictability. Convincing evidence of a causal relation with antecedent conditions requires demonstration via quantitative predictions, or at least an objective quantitative forecasting method applied to historical data.

Overall, our predictability experiments suggest severe limitations on the potential for seasonal forecasting at middle and high latitudes. Most of the interannual variability at these latitudes is chaotic in our model. We expect improvements in future models to increase the proportion of variability associated with forcings and teleconnections, especially over land areas; but already the variability produced by our model is quite realistic, so we expect our present conclusions regarding regional climate predictability to remain qualitatively unchanged.

Recent work [*e.g., Betts et al.*, 1996] has shown the importance of soil moisture in regional energy balance. As a significant climate feedback, soil moisture initial conditions can improve forecasts. But our simulations suggest that accurate soil moisture initial conditions improve forecast accuracies, averaged over a full season, by only a modest amount. Our interpretation is that even though posterior calculations show a large contribution from soil moisture to the surface energy balance, multiple runs of the model (or real world) will follow quite different paths over 3 months.

Global radiative forcings have small but statistically noticeable effects on regional seasonal climate variations in our model, even though the net forcing is only a fraction of 1 W/m^2 over most of the period. The effects are not large enough to allow climate fluctuations in a specific region to be predicted reliably, but the radiative forcing alters the probabilities. For example, the cooling in central North America during the summer after Pinatubo was a 4σ event and probably would not have occurred in the absence of Pinatubo. But the large variation of simulated temperature among our ensembles of runs implies that if another volcano of Pinatubo's magnitude occurred, we would not be able to confidently predict such strong cooling in North America.

These results are not inconsistent with findings of significant predictability at middle latitudes for certain seasons and regions. Also it should be noted that the definition of predictability varies among different studies. For example, the empirical forecasts for Canada by *Shabbar and Barnston* [1996] make use of known long-term climate trends, which helps account for their 6- and 9-month lead forecasts being as accurate as their 3-month forecasts.

10.2. Limitations and Potential Improvements

Our conclusions are limited by deficiencies in the climate models, the inaccuracy or absence of climate forcing data, and the brevity of the simulation period. The obvious strategy to obtain more substantial conclusions, longer simulations with improved

models and more accurate and complete forcing data, is meaningful only if we can identify and attack the most relevant model and data problems.

10.2.1. Model. Our objectives require realistic modeling of stratospheric influences on surface climate, because changes of ozone, stratospheric aerosols, and solar irradiance all may involve dynamical and radiative interactions between the troposphere and the stratosphere. Improved vertical resolution in the lower stratosphere is a minimal first step. It will be important to verify that stratosphere-troposphere interactions are realistically portrayed.

Forcing of the ocean by the atmosphere must be improved over the SI95 model. Radiative forcing at high latitudes can be much improved with more realistic sea ice puddling, as we have shown (Figure 1). Improvements being tested for the GISS large-scale cloud parameterizations (A.D. Del Genio, private communication, 1997) reduce the remaining discrepancy in the zonal distribution of radiative forcing at the top of the atmosphere. We expect these changes to improve radiative forcing of the ocean surface, but verification against surface observations is needed. Wind stresses delivered by the SI95 model to the ocean surface also contain substantial errors (section 3.11). We have not yet identified model improvements that correct this problem.

Heat transports differ widely among our ocean models when driven by the same forcings, confirming the need for improvements in at least some of the models. Increased horizontal and vertical resolutions are being tested in the ocean models, as well as a turbulence parameterization for sub-grid-scale mixing of heat, salt, and momentum [V. M. Canuto, Ocean turbulence: a model with shear, rotation, stratification and salinity, submitted to *Dynamics of Atmospheres and Oceans, Journal of Geophysical Research*, 1997]. Sea ice cover and related feedbacks must be calculated; the possibility of obtaining realistic sea ice cover will be improved by more realistic radiative forcing at high latitudes.

10.2.2. Data. The realism of our simulations could be increased by using more accurate boundary conditions, especially sea ice cover, and by improving the completeness and accuracy of the radiative forcings. Our present simulations employ a mean sea ice climatology; this improves results over those obtained using discontinuous AMIP sea ice distributions [*Hansen et al.*, 1996a], but it would be better to employ realistic interannual sea ice variations. That is possible at least for the period of satellite microwave observations.

Minor but significant improvements could be made in the radiative forcings already included in our simulations. We believe that the solar irradiance and well-mixed greenhouse gas forcings are accurate, but improvements are needed for the stratospheric aerosol and ozone changes. The aerosol size distribution is suspect, especially for the El Chichon period, and it could be improved from first principles using available satellite thermal infrared measurements. The main uncertainty with ozone is the upper tropospheric change. It will be difficult to reconstruct past changes of the ozone vertical profile, especially at low latitudes, but measurement of future changes is possible.

Uncertainties in interpretation of climate change will remain as long as important forcings are unmeasured. The principal case in point is tropospheric aerosols and associated changes of cloud properties, which are suspected of causing a radiative forcing comparable in magnitude to the greenhouse gas forcing [*IPCC*, 1995; *Hansen et al.*, 1997a]. The requirement is not just to measure aerosol and cloud properties but to monitor the changes of their properties to a precision of a few tenths of 1 W/m^2 [*Hansen et al.*, 1995b].
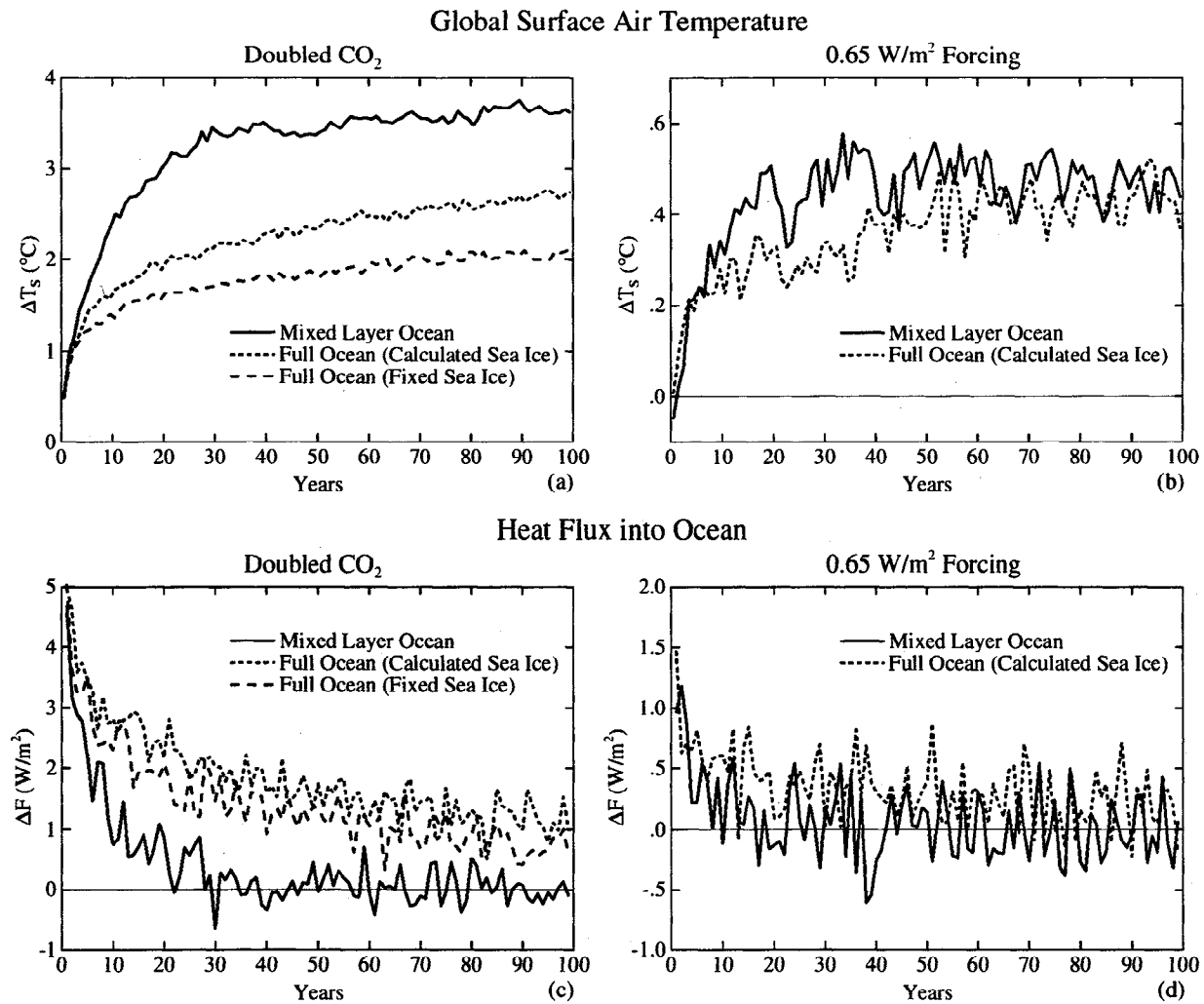
Global Surface Air Temperature

Figure 8. (a) Surface air temperature response to doubled CO_2 for the SI95 model with the Q flux ocean and (c) the corresponding heat flux into the ocean surface. Results are shown for both a mixed layer ocean and with a diffusive deep ocean attached, the latter model including cases for fixed sea ice and calculated sea ice. (b and d) Responses to the 0.65 W/m^2 planetary disequilibrium forcing, with and without a diffusive deep ocean attached to the mixed layer.

Appendix: Climate Model Sensitivity

We show here the global-mean response of the SI95 climate model for doubled CO_2 and for the 0.65 W/m^2 disequilibrium forcing, in both cases using ocean B (Q flux model). The objective is to characterize the sensitivity of the model to the canonical CO_2 forcing and to define the effectiveness of the 0.65 W/m^2 forcing. In addition, these runs illustrate the long response time of the model. Global maps of the equilibrium model response to doubled CO_2, including numerous climate diagnostics, are available via the GISS home page (http://www.giss.nasa.gov).

Doubled CO_2

The time-dependent response of surface air temperature to instantaneously doubled CO_2 is shown in Figure 8a. The case with only a mixed layer ocean (global-mean annual-maximum depth of 109 m) has sufficiently rapid response to reveal the equilibrium sensitivity (about 3.6°C) in a 100-year run. When diffusive mixing of the heat perturbations into the deep ocean is included, about 50% of the equilibrium response is obtained in the first 20 years and about

75% in the first 100 years. Similar results for a one-dimensional diffusive ocean model were found by Hansen et al. [1984, 1985].

When sea ice is held fixed the Q flux ocean yields a surface air temperature response of about 2.1°C after 100 years, compared to 2.7°C with calculated sea ice. Because of the faster response time with lower sensitivity [Hansen et al., 1985], we estimate the equilibrium response with fixed sea ice as about 2.7°-2.8°C for doubled CO_2.

The flux into the ocean surface in these model runs is shown in Figure 8c. When the full ocean is included, there is still a flux of more than 1 W/m^2 into the ocean surface after 100 years. The corresponding planetary disequilibrium (energy imbalance) is smaller by the factor 0.7, the ratio of ocean to planetary area.

Disequilibrium Forcing of 0.65 W/m^2

The initial disequilibrium was obtained by replacing a coarse infrared spectral integration, which employed absorption coefficients precalculated with fixed gas amounts, with a more accurate spectral integration. This change altered the calculated infrared opacity, increasing the greenhouse forcing at the

tropopause by about 0.65 W/m^2. *Hansen et al.* [1997b] found that all forcings are not necessarily equivalent, and thus we should determine the sensitivity of the SI95 model to this specific radiative forcing.

Figure 8b shows the response of the Q flux ocean model for the case of a mixed layer ocean and for the case with diffusive mixing of heat perturbations into the deep ocean. The equilibrium response for the mixed layer ocean indicates a sensitivity to this forcing (about 0.8°C/(W/m^2)) similar to that for the doubled CO_2 forcing (about 0.85°C/(W/m^2)). We conclude that the effectiveness of the disequilibrium forcing that we employed is reasonably representative of what might be caused by greenhouse gases added to the atmosphere prior to 1979.

References

Abramopoulos, F., A new fourth-order enstrophy and energy conserving scheme, *Mon. Weather Rev., 119*, 128-133, 1991.

Angell, J.K., and J. Korshover, Estimate of the global change in temperature, surface to 100 mbar, between 1958 and 1975, *Mon. Weather Rev., 105*, 375-385, 1977.

Ayotte, K.W., et al., An evaluation of neutral and convective planetary boundary layer parameterizations relative to large-scale eddy simulations, *Boun. Layer Meteorol., 79*, 131-175, 1996.

Barkstrom, B., E. Harrison, G. Smith, R. Green, J. Kibler, and R. Cess, Earth radiation budget experiment (ERBE) archival and April 1985 results, *Bull. Am. Meteorol. Soc., 70*, 1254-1262, 1989.

Barnett, T.P., Monte Carlo climate forecasting, *J. Clim., 8*, 1005-1022, 1995.

Barry, R.G., The parameterization of surface albedo for sea ice and its snow cover, *Prog. Phys. Geogr., 20*, 63-79, 1996.

Bengtsson, L., K. Arpe, E. Roeckner, and U. Schulzweida, Climate predictability experiments with a general circulation model, *Rep. 145*, 45 pp., Max Planck Inst. für Meteorol., Hamburg, 1995.

Betts, A.K., J.H. Hall, A.C.M. Beljaars, M.J. Miller, and P.A. Viterbo, The land-surface-atmosphere interaction, A review based on observational and global modeling perspectives, *J. Geophys. Res., 101*, 7209-7225, 1996.

Boyle, J.S., Seasonal characteristics of precipitation over the United States in AMIP simulations, *PCMDI Rep. No. 31*, 30 pp., Lawrence Livermore Lab., Livermore, Calif., 1996.

Brankovic, C. and T.N. Palmer, Atmospheric predictability and estimates of ensemble size, *Mon. Weather Rev., 125*, 859-874, 1997.

Bryan, K., A numerical method for the study of the circulation of the world ocean, *J. Comput. Phys., 4*, 347-376, 1969.

Bryan, K., and M.D. Cox, An approximate equation of state for numerical model of ocean circulation, *J. Phys. Oceanogr., 15*, 1255-1273, 1972.

Bryan, K. and L.J. Lewis, A water mass model of the world ocean, *J. Geophys. Res., 84*, 2503-2517, 1979.

Cess, R.D., et al., Uncertainties in carbon dioxide radiative forcing in atmospheric general circulation models, *Science, 262*, 1252-1255, 1993.

Cess, R.D., et al., Comparison of the seasonal change in cloud-radiative forcing from atmospheric general circulation models and satellite observations, *J. Geophys. Res., 101*, 12,791-12,794, 1996.

Charney, J.G., and J. Shukla, Predictability of monsoons, in *Monsoon Dynamics*, edited by Sir James Lighthill and R.P. Pearce, pp. 99-110, Cambridge Univ. Press, New York, 1981.

Cox, M.D., A primitive equation three-dimensional model of the ocean, *GFDL Ocean Group Tech. Rep. 1*, Geophys. Fluid Dyn. Lab., Princeton, N. J., 1984.

Del Genio, A.D., and M.S. Yao, Efficient cumulus parameterization for long-term climate studies: The GISS scheme, *Am. Meteorol. Soc. Monogr., 46*, 181-184, 1993.

Del Genio, A.D., M.S. Yao, W. Kovari, and K.K.W. Lo, A prognostic cloud water parameterization for global climate models, *J. Clim., 9*, 270-304, 1996.

Delworth, T., and S. Manabe, Climate variability and land-surface processes, *Adv. Water Resour., 16*, 3-20, 1993.

Druyan, L.M., K.P. Shah, K.W.K. Lo, J.A. Marengo, and G. Russell, Impacts of model improvements on general circulation model sensitivity to sea-surface temperature forcing, *Int. J. Climatol., 15*, 1061-1086, 1995.

Eparvier, F.G., D.W. Rusch, R.T. Clancy, and G.E. Thomas, Solar Mesosphere Explorer satellite measurements of El Chichon stratospheric aerosols, 2, Aerosol mass and size parameters, *J. Geophys. Res., 99*, 20,533-20,544, 1994.

Gaffen, D.J., Temporal inhomogeneities in radiosonde temperature records, *J. Geophys. Res., 99*, 3667-3676, 1994.

Gaffen, D.J., R.D. Rosen, D.A. Salstein, and J.S. Boyle, Evaluation of tropospheric water vapor simulations from the simulations from the Atmospheric Model Intercomparison Project, *J. Clim.*, in press, 1997.

Gates, W.L., AMIP: The Atmospheric Model Intercomparison Project, *Bull. Am. Meteorol. Soc., 73*, 1962-1970, 1992.

Garratt, J.R., Sensitivity of climate simulations to land-surface and atmospheric boundary-layer treatments — A review, *J. Clim., 6*, 419-449, 1993.

Gleckler, P.J., et al., Cloud-radiative effects on implied oceanic energy transports as simulated by atmospheric general circulation models, *Geophys. Res. Lett., 22*, 791-794, 1995.

Gloerson, P., W.J. Campbell, D.J. Cavalieri, J.C. Comiso, C.L. Parkinson, and H.J. Zwally, Arctic and Antarctic Sea Ice, 1978-1987, *NASA Spec. Publ., SP-511*, 290 pp., 1992.

Gordon, H.R., and D.K. Clark, Clear water radiances for atmospheric correction of coastal zone color scanner imagery, *Appl. Opt., 20*, 4175-4180, 1981.

Gordon, H.R., and M. Wang, Influence of oceanic whitecaps on atmospheric correction of SeaWiFS, *Appl. Opt., 33*, 7754-7763, 1994.

Gordon, H.R., O.B. Brown, R.H. Evans, J.W. Brown, R.C. Smith, K.S. Baker, and D.K. Clark, A semi-analytic radiance model of ocean color, *J. Geophys. Res., 93*, 10,909-10,924, 1988.

Graf, H.F., J. Perlwitz, and I. Kirchner, Northern hemisphere tropospheric mid-latitude circulation after violent volcanic eruptions, *Beitr. Phys. Atmosph., 67*, 3-13, 1994.

Graham, N.E., Simulation of recent global temperature trends, *Science, 267*, 666-671, 1995.

Grenfell, T.C., and D.K. Perovich, Spectral albedos of sea ice and incident solar irradiance in the southern Beufort Sea, *J. Geophys. Res., 89*, 3573-3580, 1984.

Grenfell, T.C., S.G. Warren, and P.C. Mullen, Reflection of solar radiation by the Antarctic snow surface at ultraviolet, visible, and near-infrared wavelengths, *J. Geophys. Res., 99*, 18,669-18,684, 1994.

Hahmann, A.N., D.M. Ward, and R.E.Dickinson, Land surface temperature and radiative fluxes response of the NCAR CCM2/Biosphere-Atmosphere Transfer Scheme to modifications in the optical properties of clouds, *J. Geophys. Res., 100*, 23,239-23,252, 1995.

Haigh, J.D., The impact of solar variability on climate, *Science, 272*, 981-984, 1996.

Handler, P., Possible association between the climatic effects of stratospheric aerosols and sea surface temperatures in the eastern tropical Pacific Ocean, *J. Climatol., 6*, 31-41, 1986.

Hansen, J., G. Russell, D. Rind, P. Stone, A. Lacis, S. Lebedeff, R. Ruedy, and L. Travis, Efficient three-dimensional global models for climate studies: Models I and II, *Mon. Weather Rev., 111*, 609-662, 1983a.

Hansen, J., D. Johnson, A. Lacis, S. Lebedeff, P. Lee, D. Rind, and G. Russell, Climatic effects of atmospheric carbon dioxide, *Science, 220*, 874-875, 1983b.

Hansen, J., A. Lacis, D. Rind, G. Russell, P. Stone, I. Fung, R. Ruedy, and J. Lerner, Climate sensitivity: Analysis of feedback mechanisms, in *Climate Processes and Climate Sensitivity, Geophys. Monogr.*, vol. 29, edited by J.E. Hansen and T. Takahashi, pp. 130-163, AGU, Washington, D. C., 1984.

Hansen, J., G. Russell, A. Lacis, I. Fung, D. Rind, and P. Stone, Climate response times: Dependence on climate sensitivity and ocean mixing, *Science, 229*, 857-859, 1985.

Hansen, J., I. Fung, A. Lacis, D. Rind, S. Lebedeff, R. Ruedy, G. Russell, and P. Stone, Global climate changes as forecast by the Goddard Institute for Space Studies three-dimensional model, *J. Geophys. Res., 93*, 9341-9364, 1988.

Hansen, J., A. Lacis, and M. Prather, Greenhouse effect of chloro-fluorocarbons and other trace gases, *J. Geophys. Res., 94*, 16,417-16,421, 1989.

Hansen, J., A. Lacis, R. Ruedy, M. Sato, and H. Wilson, How sensitive is the world's climate?, *Res. Explor., 9*, 142-158, 1993.

Hansen, J., H. Wilson, M. Sato, R. Ruedy, K. Shah, and E. Hansen, Satellite and surface temperature data at odds?, *Clim. Change, 30*, 103-117, 1995a.

Hansen, J., W. Rossow, B. Carlson, A. Lacis, L. Travis, A. Del Genio, I. Fung, B. Cairns, M. Mishchenko, and M. Sato, Low-cost long-term monitoring of global climate forcings and feedbacks, *Clim. Change, 31*, 247-271, 1995b.

Hansen, J., M. Sato, and R. Ruedy, Long-term changes of the diurnal temperature cycle: Implications about mechanisms of global climate change, *Atmos. Res., 37*, 175-209, 1995c.

Hansen, J., et al., A Pinatubo climate modeling investigation, in *Global Environment Change*, edited by G. Fiocco, D. Fua', and G. Visconti, *NATO ASI Ser. I*, vol. 42, 310 pp., Springer-Verlag, New York, 1996a.

Hansen, J., R. Ruedy, M. Sato, and R. Reynolds, Global surface air temperature in 1995: Return to pre-Pinatubo level, *Geophys. Res. Lett.*, 23, 1665-1668, 1996b.

Hansen, J., M. Sato, A. Lacis, and R. Ruedy, The missing climate forcing, *Philos. Trans., R. Soc. London, Ser. B*, 352, 231-240, 1997a.

Hansen, J., M. Sato, and R. Ruedy, Radiative forcing and climate response, *J. Geophys. Res.*, 102, 6831-6864, 1997b.

Hartke, G.J., and D. Rind, Improved surface and boundary layer models for the GISS general circulation model, *J. Geophys. Res.*, in press, 1997.

Harzallah, A., and R. Sadourney, Internal versus SST-forced atmospheric variability as simulated by an atmospheric general circulation model, *J. Clim.*, 8, 474-495, 1995.

Hasselmann, K., R. Sausen, E. Maier-Reimer, and R. Voss, On the cold start problem in transient simulations with coupled ocean-atmosphere models, *Clim. Dyn.*, 9, 53-61, 1993.

Hauglustaine, D.A., C. Granier, G.P. Brasseur, and G. Megie, The importance of atmospheric chemistry in the calculation of radiative forcing on the climate system, *J. Geophys. Res.*, 99, 1173-1186, 1994.

Hellerman, S., and M. Rosenstein, Normal monthly wind stress over the world ocean with error estimates, *J. Phys. Oceanogr.*, 13, 1093-1104, 1983.

Hollandsworth, S.M., R.D. McPeters, L.E. Flynn, W. Planet, A.J. Miller, and S. Chandra, Ozone trends deduced from combined Nimbus 7 SBUV and NOAA 11 SBUV/2 data, *Geophys. Res Lett.*, 22, 905-908, 1995a.

Hollandsworth, S.M., K.P. Bowman, and R. D. McPeters, Observational study of the quasi-biennial oscillation in ozone, *J. Geophys. Res.*, 100, 7347-7361, 1995b.

Hood, L.L., and D.A. Zaff, Lower stratospheric stationary waves and the longitude dependence of ozone trends in winter, *J. Geophys. Res.*, 100, 25,791-25,800, 1995.

Hurrell, J.W., and K.E. Trenberth, Spurious trends in satellite MSU temperatures from merging different satellite records, *Nature*, 386, 164-167, 1997.

Idso, S.B., Climatic effects of atmospheric carbon dioxide, *Science*, 220, 874, 1983.

Intergovernmental Panel on Climate Change (IPCC), *Climate Change 1994: Radiative Forcing of Climate Change*, edited by J.T. Houghton et al., 339 pp., Cambridge Univ. Press, New York, 1995.

Johannessen, O.M., M. Miles, and E. Bjorgo, The Arctic's shrinking sea ice, *Nature*, 376, 126-127, 1995.

Kalnay-Rivas, E., A. Bayliss, and J. Storch, The 4th order GISS model of the global atmosphere, *Contrib. Atmos. Phys.*, 50, 306-311, 1977.

Karl, T.R., R.W. Knight, G. Kukla, and G. Gavin, Evidence for the radiative effects of anthropogenic sulfate aerosols in the observed climate record, in *Aerosol Forcing of Climate*, edited by R. Charlson and J. Heintzenberg, pp. 363-382, John Wiley, New York, 1995.

Knutson, T.R., and S. Manabe, Impact of increased CO_2 on simulated ENSO-like phenomena, *Geophys. Res. Lett.*, 21, 2295-2298, 1994.

Kodera, K., and K. Yamazaki, A possible influence of recent polar stratospheric coolings on the troposphere in the northern hemisphere winter, *Geophys. Res. Lett.*, 21, 809-812, 1994.

Koepke, P., Effective reflectance of oceanic whitecaps, *Appl. Opt.*, 23, 1816-1824, 1984.

Kumar, A., A. Leetmaa, and M. Ji, Simulations of atmospheric variability induced by sea surface temperatures and implications for global warming, *Science*, 266, 632-637, 1994.

Kumar, A., M. Hoerling, M. Ji, A. Leetmaa, and P. Sardeshmukh, Assessing a GCM's suitability for making seasonal predictions, *J. Clim.*, 9, 115-129, 1996.

Kurgansky, M.V., K. Dethloff, I.A. Pisnichenko, H. Gernandt, F.M. Chmielewski, and W. Jansen, Long-term climate variability in a simple, nonlinear model, *J. Geophys. Res.*, 101, 4299-4314, 1996.

Lacis, A.A., D.J. Wuebbles, and J.A. Logan, Radiative forcing of climate by changes of the vertical distribution of ozone, *J. Geophys. Res.*, 95, 9971-9981, 1990.

Lacis, A., J. Hansen, and M. Sato, Climate forcing by stratospheric aerosols, *Geophys. Res. Lett.*, 19, 1607-1610, 1992.

Lambert, A., R.G. Grainger, J.J. Remedios, C.D. Rodgers, M. Corney, and F.W. Taylor, Measurements of the evolution of the Mt. Pinatubo aerosol cloud by ISAMS, *Geophys. Res. Lett.*, 20, 1287-1290, 1993.

Langner, J., and H. Rodhe, A global three-dimensional model of the tropospheric sulfur cycle, *J. Atmos. Chem.*, 13, 225-263, 1991.

Lau, K.M., J.H. Kim, and Y. Sud, Intercomparison of hydrologic processes in AMIP GCMs, *Bull. Am. Meteorol. Soc.*, 77, 2209-2227, 1996.

Lean, J., Variations in the Sun's radiative output, *Rev. Geophys.*, 29, 505-535, 1991.

Lean, J., G.J. Rottman, H.L. Kyle, T.N. Woods, J.R. Hickey, and L.C. Puga, Detection and parameterization of variations in solar middle- and near-ultraviolet radiation, *J. Geophys. Res.*, in press, 1997.

Lelieveld, J., P.J. Crutzen, and C. Bruhl, Climate effects of atmospheric methane, *Chemosphere*, 26, 739-768, 1993.

Levitus, S., Climatological atlas of the world ocean, *NOAA Prof. Pap. 13*, 173 pp., Environ. Res. Lab., Rockville Md., 1982.

Levitus, S., R. Burgett, and T.P. Boyer, NOAA World Ocean Atlas 1994, vol. 3 and 4, 99 and 117 pp., Natl. Oceangr. Data Cen., Washington, D. C., 1994.

Logan, J.A., Trends in the vertical distribution of ozone: An analysis of ozonesonde data, *J. Geophys. Res.*, 99, 25,553-25,585, 1994.

Lorenz, E.N., Deterministic nonperiodic flow, *J. Atmos. Sci.*, 20, 130-141, 1963.

Lorenz, E.N., Atmospheric predictability experiments with a large numerical model, *Tellus*, 34, 505-513, 1982.

Lorenz, E.N., Irregularity: A fundamental property of the atmosphere, *Tellus, Ser. A*, 36, 98-110, 1984.

MacCracken, M.C., Climatic effects of atmospheric carbon dioxide, *Science*, 220, 873-874, 1983.

Macdonald, A.M., and C. Wunsch, An estimate of global ocean circulation and heat fluxes, *Nature*, 382, 436-439, 1996.

Manabe, S., and R.J. Stouffer, Low-frequency variability of surface air temperature in a 1000-year integration of a coupled atmosphere-ocean-land surface model, *J. Clim.*, 9, 376-393, 1996.

Manabe, S., and R.T. Wetherald, On the distribution of climate change resulting from an increase in CO_2 content of the atmosphere, *J. Atmos. Sci.*, 37, 99-118, 1980.

Manabe, S., K. Bryan, and M.J. Spelman, Transient response of a global ocean-atmosphere model to a doubling of atmospheric carbon dioxide, *J. Phys. Oceanogr.*, 20, 130-141, 1990.

Maslanik, J.A., M.C. Serreze, and R.G. Barry, Recent decreases in Arctic summer ice cover and linkages to atmospheric circulation anomalies, *Geophys. Res. Lett.*, 23, 1677-1680, 1996.

Matthews, E., Global vegetation and land-use: New high resolution data bases for climate studies, *J. Clim. Appl. Meteorol.*, 22, 474-487, 1983.

Matthews, E., Prescription of land-surface boundary conditions in GISS GCM II: A simple method based on fine-resolution data bases, *NASA Tech. Memo., NASA TM 86096*, 1984.

McCormick, M.P., R.E. Viega, and W.P. Chu, Stratospheric ozone profile and total ozone trends derived from the SAGE I and SAGE II data, *Geophys. Res. Lett.*, 19, 269-272, 1992.

McPeters, R.D., Ozone profile comparisons, in *The Atmospheric Effects of Stratospheric Aircraft*, vol II, edited by M.J. Prather and E.E. Remsberg, 268 pp., *NASA Ref. Publ. 1092*, pp. D1-D37, 1993.

Miller, J.R., G.L. Russell, and G. Caliri, Continental-scale river flow in climate models, *J. Clim.*, 7, 914-928, 1994.

Miller, R.L., and X. Jiang, Surface energy fluxes and coupled variability in the tropics of a coupled general circulation model, *J. Clim.*, 9, 1599-1620, 1996.

Mitchell, J.F.B., R.A. Davis, W.J. Ingram, and C.A. Senior, On surface temperature, greenhouse gases, and aerosols: Models and observations, *J. Clim.*, 8, 2364-2386, 1995.

Miyakoda, K., T. Gordon, R. Caverly, W. Stern, J. Sirutis, and W. Bourke, Simulations of a blocking event in January 1977, *Mon. Weather Rev.*, 111, 846-869, 1983.

Munk, W., and A.M.G. Forbes, Global ocean warming: An acoustic measure?, *J. Phys. Oceanogr.*, 19, 1765-1768. 1989.

Nerem, R.S., B.J. Haines, J. Hendricks, J.F. Minster, G.T. Mitchum, and W.B. White, Improved determination of global mean sea level variations using TOPEX/POSEIDON altimeter data, *Geophys. Res. Lett.*, 24, 1331-1334, 1997.

Oberhuber, J.M., An atlas based upon the "COADS" data set: The budgets of heat, buoyancy and turbulent kinetic energy at the surface of the global ocean, *Rep. 15*, Max Planck Inst. für Meteorol., Hamburg, Germany, 1988.

Oltmans, S.J., and D.J. Hofmann, Increase in lower-stratospheric water vapor at a mid-latitude northern hemisphere site from 1981 to 1989, *Nature*, 374, 146-149, 1995.

Parker, D.E., and D.I. Cox, Towards a consistent global climatological rawinsonde data-base, *Int. J. Climatol.*, 15, 473-496, 1995.

Philander, S.G.H., R.C. Pacanowski, N.C. Lau, and M.J. Nath, Simulation of ENSO with a global atmospheric GCM coupled to a high-resolution, tropical Pacific Ocean GCM, *J. Clim.*, 5, 308-329, 1992.

Pielke, R.A., and X. Zeng, Long-term variability of climate, *J. Atmos. Sci.*, *51*, 155-159, 1994.

Portmann, R.W., S. Solomon, J. Fishman, J.R. Olson, J.T. Kiehl, and B. Briegleb, *J. Geophys. Res.*, *102*, 9409-9417, 1997.

Prabhakara, C., J.J. Nucciarone, and J.M. Yoo, Examination of "Global atmospheric temperature monitoring with satellite microwave measurements," 1, Theoretical considerations, *Clim. Change*, *30*, 349-366, 1995.

Prather, M.J., Numerical advection by conservation of second-order moments, *J. Geophys. Res.*, *91*, 6671-6680, 1986.

Ramaswamy, V., M.D. Schwarzkopf, and W.J. Randel, Fingerprint of ozone depletion in the spatial and temporal pattern of recent lower-stratospheric cooling, *Nature*, *382*, 616-618, 1996.

Reynolds, R.W., and T.M. Smith, Improved global sea surface temperature analyses, *J. Clim.*, *7*, 929-948, 1994.

Rind, D., and J. Lerner, The use of on-line tracers as a diagnostic tool in GCM model development, *J. Geophys. Res.*, *101*, 12,667-12,683, 1996.

Rind, D., R. Suozzo, N.K. Balachandran, A. Lacis, and G.L. Russell, The GISS global climate/middle atmosphere model, I, Model structure and climatology, *J. Atmos. Sci.*, *45*, 329-370, 1988.

Rind, D., R. Healy, C. Parkinson, and D. Martinson, The role of sea ice in 2×CO_2 climate model sensitivity, I, The total influence of sea ice thickness and extent, *J. Clim.*, *8*, 449-463, 1995.

Robock, A., The volcanic contribution to climate change of the past 100 years, in *Greenhouse-Gas-Induced Climatic Change: A Critical Evaluation of Simulations and Observations*, edited by M.E. Schlesinger, pp. 429-443, Elsevier, New York, 1991.

Robock, A., and J. Mao, Winter warming from large volcanic eruptions, *Geophys. Res. Lett.*, *12*, 2405-2408, 1992.

Rosenzweig, C., and F. Abramopoulos, Land surface model development for the GISS GCM, *J. Clim.*, in press, 1997.

Rossow, W.B., and Y.C. Zhang, Calculation of the top-of-the-atmosphere radiative fluxes from physical quantities derived from ISCCP data sets, II, Validation and results, *J. Geophys. Res.*, *100*, 1167-1197, 1995.

Russell, G.L., and J.A. Lerner, A new finite-differencing scheme for the tracer transport equation, *J. Appl Meteorol.*, *20*, 1483-1498, 1981.

Russell, G.L., J.R. Miller, and L.C. Tsang, Seasonal oceanic heat transports computed from an atmospheric model, *Dyn. Atmos. Oceans*, *9*, 253-271, 1985.

Russell, G.L., J.R. Miller, and D. Rind, A coupled atmosphere-ocean model for transient climate change studies, *Atmos. Oceans*, *33*, 683-730, 1995.

Russell, P.B., et al., Global to microscale evolution of the Pinatubo volcanic aerosol derived from diverse measurements and analyses, *J. Geophys. Res.*, *101*, 18,745-18,763, 1996.

Sato, M., J.E. Hansen, M.P. McCormick, and J.B. Pollack, Stratospheric aerosol optical depth, 1850-1990, *J. Geophys. Res.*, *98*, 22,987-22,994, 1993.

Shabbar, A., and A.G. Barnston, Skill of seasonal climate forecasts in Canada using canonical correlation analysis, *Mon. Weather Rev.*, *124*, 2370-2385, 1996.

Shah, K.P., and D. Rind, Use of microwave brightness temperatures with a general circulation model, *J. Geophys. Res.*, *100*, 13,841-13,874, 1995.

Shukla, J., Dynamical predictability of monthly means, *J. Atmos. Sci.*, *38*, 2547-2572, 1981.

Snetsinger, K.G., G.V. Ferry, P.B. Russell, R.F. Pueschel, V.R. Oberbeck, D.M. Hayes, and W. Fong, Effects of El Chichon on stratospheric aerosols late 1982 to early 1984, *J. Geophys. Res.*, *92*, 14,761-14,771, 1987.

Spencer, R.W., J.R. Christy, and N.C. Grody, Precision tropospheric temperature monitoring 1979-90, *Palaeogeogr. Palaeoclimatol. Palaeoecol.*, *90*, 113-120, 1991.

Stern, W., and K. Miyakoda, Feasibility of seasonal forecasts inferred from multiple GCM simulations, *J. Clim.*, *8*, 1071-1085, 1995.

Stolarski, R.S., P. Bloomfield, R.D. McPeters, and J.R. Herman, Total ozone trends deduced from Nimbus 7 TOMS data, *Geophys. Res. Lett.*, *18*, 1015-1018, 1991.

Stone, P.H., and J.S. Risbey, On the limitations of general circulation climate models, *Geophys. Res. Lett.*, *17*, 2173-2176, 1990.

Taylor, K.E., and J.E. Penner, Anthropogenic aerosols and climate change, *Nature*, *369*, 734-736, 1994.

Tegen, I., A.A. Lacis, and I. Fung, The influence of mineral aerosols from disturbed soils on climate forcing, *Nature*, *380*, 419-422, 1996.

Tett, S.F.B., J.F.B. Mitchell, D.E. Parker, and M.R. Allen, Human influence on the atmospheric vertical temperature structure: Detection and observations, *Science*, *274*, 1170-1173, 1996.

Toon, O.B., and J.B. Pollack, A global average model of atmospheric aerosols for radiative transfer calculations, *J. Appl. Meteorol.*, *15*, 225-246, 1976.

Trenberth, K.E., and C.J. Guillemot, Physical processes involved in the 1988 drought and 1993 floods in North America, *J. Clim.*, *9*, 1288-1298, 1996.

Vinnikov, K.Y., A. Robock, R.J. Stouffer, and S. Manabe, Vertical patterns of free and forced climate variations, *Geophys. Res. Lett.*, *23*, 1801-1804, 1996.

Wang, H.J., D.M. Cunnold, and X. Bao, A critical analysis of Stratospheric Aerosol and Gas Experiment ozone trends, *J. Geophys. Res.*, *101*, 12,495-12,514, 1996.

Weare, B.C., I.I. Mokhov, and Project Members, Evaluation of total cloudiness and its variability in the atmospheric model intercomparison project, *J. Clim.*, *8*, 2224-2238, 1995.

Willson, R.C., and H.S. Hudson, The sun's luminosity over a complete solar cycle, *Nature*, *351*, 42-44, 1991.

World Meteorological Organization (WMO), Scientific assessment of ozone depletion, Global Ozone Research and Monitoring Project, *WMO Rep. 37*, Geneva, 1994.

Young, R.E., H. Houben, and O.B. Toon, Radiatively forced dispersion of the Mt. Pinatubo volcanic cloud and induced temperature perturbations in the stratosphere during the first few months following the eruption, *Geophys. Res. Lett.*, *21*, 369-372, 1994.

Yulaeva, E., and J.M. Wallace, The signature of ENSO in global temperature and precipitation fields derived from the Microwave Sounding Unit, *J. Clim.*, *7*, 1719-1736, 1994.

Ziemke, J.R., S. Chandra, A.M. Thompson, and D.P. McNamara, Zonal asymmetries in southern hemisphere column ozone: Implications of biomass burning, *J. Geophys. Res.*, *101*, 14,421-14,427, 1996.

B. Cairns, B. Carlson, L. Druyan, J. Glascoe, J. Hansen, X. Jiang, A. Lacis, J. Lerner, K. Lo, R. Miller, R. Ruedy, G. Russell, M. Sato, and I. Tegen, NASA Goddard Institute for Space Studies, 2880 Broadway, New York, NY 10025 (e-mail: jhansen@giss.nasa.gov).

K. Asamoah, I. Ramberran, MAST High School, Cambria Heights, Queens, NY 11411.

K. Beckford, S. Borenstein, and S. de Castro, Department of Natural Science, York College, Jamaica, Queens, NY 11451.

E. Brown, Marine Sciences, University of Miami, Coral Gables, FL 33124.

B. Curran, T. Ferede, M. Fox, and A. Luckett, Bronx High School of Science, Bronx, NY 10468.

R. Willson, 2845 Windfall Avenue, Altadena, CA 91001.

P. Etwarrow, C. Johnson, N. Lawrence, and S. Thomas, Far Rockaway High School, Brooklyn, NY 11691.

D. Gaffen, NOAA Air Resources Laboratory, Silver Spring, MD 20910.

H. Gordon, Department of Physics, University of Miami, Coral Gables, FL 33124.

S. Hollandsworth, R. McPeters, and A. Thompson, NASA Goddard Space Flight Center, Greenbelt, MD 20771.

J. Lean, E.O. Hulbert Center for Space Research, Naval Research Laboratory, Washington, DC 20375.

J. Logan, Department of Earth and Planetary Sciences, Harvard University, Cambridge, MA 02137.

M.P. McCormick, Department of Physics, Hampton University, Hampton, VA 23668.

P. Minnis, L. Thomason, and J. Zawodny NASA Langley Research Center, Hampton, VA 23665.

P. Russell, NASA Ames Research Center, Moffett Field, CA 94035.

P. Stone, Center for Meteorology, Massachusetts Institute of Technology, Cambridge, MA 02139.

J. Wilder, Electrical Engineering Division, Polytechnic University, Brooklyn, NY 11201.